The Pennsylvania State University

The Graduate School

Department of Materials Science and Engineering

EFFECTS OF EXPOSURE HISTORY ON THE SURFACE MECHANICAL PROPERTIES OF FLOAT GLASS

A Thesis in

Materials Science and Engineering

by

Pavan V.N. Kolluru

© 2008 Pavan V.N. Kolluru

Submitted in Partial Fulfillment

of the Requirements

for the Degree of

Master of Science

December 2008

The thesis of Pavan V.N. Kolluru was reviewed and approved* by the following:

Christopher L. Muhlstein
Associate Professor of Materials Science and Engineering
Thesis Advisor

David J. Green
Professor of Ceramic Science and Engineering

Carlo G. Pantano
Distinguished Professor of Materials Science and Engineering

Joan M. Redwing
Professor of Materials Science and Engineering
Chair of the Intercollege Materials Science and Engineering Graduate Degree Program

*Signatures are on file in the Graduate School.

ABSTRACT

Commercial float glasses are technologically important materials that are commonly used in architectural, automotive and structural applications. The surface layers of these glasses are usually affected by their exposure to corrosive environments leading to structural modifications at the atomic scale. Such variations in surface mechanical properties of these glasses are expected to control a wide range of glass characteristics such as the flaw generation and propagation, glass strength and adhesion of coatings. The current study evaluated the mechanical property variations in commercial float glasses on a length scale equal to the thickness of the corrosion modified surface layer using nanoindentation. This provided an insight into the influence of surface cleaning treatments and corrosion on elastic and plastic response of the float glass surfaces. Variations in the reduced elastic modulus and hardness were evaluated for fresh soda-lime-silica float glass surfaces that were subjected to controlled surface cleaning treatments in pH 0.9 hydrochloric acid, pH 7.1 reverse osmosis water and pH 9.5 Alconox® solutions. Further, controlled experiments were performed to evaluate the effects of short-term corrosive exposure conditions such as weathering and leaching in de-ionized water on the surface mechanical properties of fresh float glass. Reduced elastic modulus variations in the range of 0.5 – 9% and hardness variations from 2 – 35% were observed due to these controlled exposure conditions. Effects of corrosion on the surface mechanical properties of the tin-enriched side of fresh float glass were found to be very different from the effects on the air side. The relative hardness of the tin side compared to the air side of the float glass was dependent on the exposure history of the glass, which may be the dominant factor that controls float glass surface mechanical properties. Nanoindentation experiments were also performed on 2, 6 and 8 mm thick aged commercial soda-lime-silica float glasses with known tin concentration profiles that had been exposed to laboratory air over a long period of 16 years. The indentation penetration depths lay between 50 and 225 nm, the region with the largest concentration and the steepest gradient of diffused tin. Attempts to correlate the trends in reduced elastic modulus and hardness of these surfaces with their tin concentration profiles

indicated that the tin diffusion into float glass was not the most dominant parameter affecting their mechanical properties. Upon comparing the reduced elastic modulus and hardness results of the aged 2 mm thick float glass with those from the 2 mm thick fresh float glass that was subjected to different controlled exposure conditions, it appeared that the aged float glasses were also being affected by their exposure history. The reduced elastic modulus and hardness of the tin side of the fresh float glass were found to nearly invariant after exposing to corrosive environments, indicating that the tin side was more resistant to corrosion. Further, the less resistant air side underwent reduction in hardness and reduced modulus after corrosion due to which the corresponding tin sides were harder and had a higher modulus. While an earlier study had indicated that the tin side may be harder than the tin side, a few others had reported that the possibilities of tin side possessing the same or lower hardness and elastic modulus as compared to the air side. Based on the results from both fresh and aged float glasses, these contradictory observations in the published literature are attributed to the exposure history dependence of float glass. The fact that even the short duration surface cleaning treatments significantly affected the reduced elastic modulus of these float glass surfaces raises serious questions about the use of silicate glasses to calibrate nanoindentation systems.

TABLE OF CONTENTS

LIST OF FIGURES vii

LIST OF TABLES xii

ACKNOWLEDGEMENTS xiii

Chapter 1 Introduction 1

1.1 Float Glass 1
1.1.1 Float Glass Processing 2
1.1.2 Compositional and Structural Variations in Float Glass 3
1.1.3 Effect of Tin Diffusion on Physical Properties 5
1.2 Float Glass Corrosion 8
1.3 Nanoindentation 10
1.3.1 Analysis of Nanoindentation Force-Displacement Data 11
1.3.2 Errors Associated with Nanoindentation Testing and Data Analysis 17
1.4 Thesis Structure 18

Chapter 2 Nanoindentation Methodology and Data Analysis 20

2.1 Nanoindentation Test Setup 20
2.1.1 The Nanoindenter 20
2.1.2 Nanoindentation Testing Parameters 22
2.1.2.1 Feedback Control 23
2.1.2.2 In-situ Imaging 24
2.1.3 Sample Preparation 26
2.2 Instrument Calibrations 27
2.2.1 Calibration Material 28
2.2.2 Transducer Calibration 29
2.2.3 Thermal Drift 30
2.2.4 Machine Compliance Calibration 31
2.2.5 Area Function Calibration 37
2.3 Nanoindentation Data Analysis 39
2.3.1 Inelastic Effects 41
2.3.2 Experimental Pile-up Correction 42
2.3.2.1 Pile-up Corrections for Area Calibration Data 51
2.3.2.2 Pile-up Correction for Test Data 53
2.3.3 Surface Roughness 55
2.4 Representation of Results and Error Analysis 57
2.5 General Methodology of Performing a Nanoindentation Test 57

Chapter 3 Exposure History Dependence of Float Glass Mechanical Properties 59

3.1 Motivation....59
3.2 Controlled Exposure Conditions....63
3.2.1 Surface Cleaning Treatments....64
3.2.2 Short-term Corrosion....65
3.3 Effects of Exposure Conditions on Nanoindentation Results....66
3.3.1 Influence of Surface Cleaning Treatments....70
3.3.2 Influence of Short-term Corrosion....77
3.4 Summary....83

Chapter 4 Effects of Exposure History and Tin Diffusion on the Nanomechanical Properties of Aged Commercial Float Glass....85

4.1 Sample Specifications....86
4.2 Role of Tin Diffusion on Float Glass Surface Nanomechanical Behavior....89
4.3 Role of Exposure History on Float Glass Surface Nanomechanical Behavior....95
4.4 Summary....99

Chapter 5 Conclusions and Future Work....101

5.1 Conclusions....101
5.2 Recommended Future Work....105

Bibliography....106

LIST OF FIGURES

Figure **1.1**: Schematic illustration of the float process of manufacturing flat glass [1]. The molten glass in the furnace flows over molten tin in the float bath and solidifies along the length of the bath. It is then picked up by metallic rollers and passed in the annealing lehr. 3

Figure **1.2**: Illustration of the two stages/mechanisms of corrosion of alkali silicate glasses [28]. 8

Figure **1.3**: Schematic illustration of a typical nanoindentation load (P) – displacement (h) curve depicting some important data analysis parameters. 12

Figure **2.1**: A schematic illustration of a local coordinate system marked on the sample using knoop indents. The global coordinate system of the nanoindenter's stage is also shown in the figure. 27

Figure **2.2**: Machine compliance correction performed using an iterative approach for displacement controlled indents on C1737f glass, with peak penetration displacement in the range of 140 – 300 nm. The figure shows the final iteration and machine compliance was determined to be 2.11 nm/mN. 35

Figure **2.3**: Machine compliance as a function of the data set range, depicting the fact that machine compliance is a variable in the first hundred nanometers. 36

Figure **2.4**: Experimentally evaluated, pile-up corrected indenter tip area calibration function. The calibration standard used was Corning 1737f glass with an elastic modulus (E) = 70.9 GPa and Poisson's ratio (ν) = 0.22 [60]. Data in red circles depicts the experimentally evaluated area function while the solid black line represents the curve fit to this experimental data. It is this curve fit that is used as the indenter tip area function. The importance of this calibration is also projected by comparing the experimental results with an ideal tip are function that assumes ideal spherical shape for the indenter tip. 39

Figure **2.5**: Schematic depiction of the role of pile-up in increasing the projected contact area during indentation 43

Figure **2.6**: A 3-dimensional post indent in-situ AFM image on float glass showing the pile-up around an indent along with the pile-up evaluation scheme that was employed in this study. The white circle denoted by A represents the deepest point in the residual indent impression. Four equiangular line scans (numbered 1-4) radiating from this point were used to capture the pile-up around the indent at 8 different locations as shown. The total length of each line scan was half the length of the dimensions of the image 46

Figure **2.7**: Quantitative topographical data (height (*h*) above or below the mean surface plane) from the four line scans shown in Figure **2.6** plotted as a function of the lateral scan distance. The two peak points on either side of the deepest point (A) on the each line scan are marked in circles in this figure and they depict the values of pile-up captured by the MATLAB algorithm. The mean of these 8 values was denoted as the pile-up around the indent. 46

Figure **2.8**: Experimentally evaluated mean values of pile-up (expressed as percentage of the maximum penetration depth) are plotted as a function of average maximum penetration depth for the displacement controlled indents performed on the Corning 1737f calibration glass. It is evident there exists a measurable amount of pile-up in the reference glass that shows a slight increase as a function of the maximum indentation depth. This pile-up was taken into consideration during the evaluation of the tip area function shown in Figure **2.4**. The error bars are one standard deviation in length on either side of the mean value. 49

Figure **2.9**: Pile-up that was observed on the air side of a 2 mm thick Guardian float glass for the three different force control indentations where the peak indentation forces were 750, 2000 and 4000 μN. Pile-up was observed to increase with increasing peak force conditions. 50

Figure **2.10**: Schematic depiction of pile-up correction procedure employed for indenter tip area function calibration data. The figure shows how the unloading segment of the force-displacement curve used for the area function calibration was modified based on the estimated pile-up. 52

Figure **2.11**: The effect of pile-up correction on the calibrated indenter tip area function. The figure compares the area function curve that was calibrated without considering pile-up around the indents against the area function curve that was calibrated after correcting for the pile-up shown in Figure **2.8**. ...53

Figure **2.12**: Effect of pile-up correction on the measured reduced elastic modulus of the air side of 2 mm thick Guardian float glass whose pile-up response was depicted in Figure **2.9**. It can be observed that the reduced modulus decreased after pile-up correction. 55

Figure **3.1**: Representative pre-indent in-situ AFM line scans from 4×4 μm^2 regions on a 6 mm thick aged float glass. Clearly, there is a variation in the surface roughness of the two regions and accordingly these regions are labeled as 'smooth' and 'rough' regions. The nominal peak-to-valley roughness for the smooth region is 2 nm while it is around 6 nm for the rough region. 60

Figure **3.2**: A 3 – dimensional post-indent in-situ AFM image of a force controlled indent (peak force of 6500 μN) within the smooth region of the 6

mm thick aged float glass shown in Figure **3.1**. The peak penetration depth for this indent was ~300 nm. Pile-up was observed to be ~25 nm. 61

Figure **3.3**: A 3–dimensional post-indent in-situ AFM image of a force controlled indent (peak force of 6500 μN) within the rough region of the 6 mm thick aged float glass that was shown in Figure **3.1**. The peak penetration depth for this indent was ~300 nm. Pile-up was observed to be ~60 nm. 62

Figure **3.4**: Representative line scans obtained from pre-indent in-situ AFM images of float glass surfaces subjected to acidic (pH 0.9), neutral (pH 7.1) and alkaline (pH 9.5) surface cleaning treatments. Inset shows a magnified view from a reduced length scale. It is observed that all the surfaces have the same nominal surface roughness and therefore the observed mechanical property variations across these surfaces are due to the cleaning treatments, not variations in surface roughness. 69

Figure **3.5**: Representative line scans obtained from pre-indent in-situ AFM images of fresh, weathered and leached float glass surfaces. Inset shows a magnified view from a reduced length scale. It is observed that all the surfaces have the same nominal surface roughness. Therefore, the observed mechanical property differences are due to the short-term corrosive exposure conditions and related structural changes, not due to surface roughness variations. 69

Figure **3.6**: Experimentally evaluated average percentage pile-up as a function of the average maximum penetration depth for the surfaces subjected to acidic (pH 0.9), neutral (ph 7.1) and alkaline (pH 9.5) cleaning treatments. Data plotted are the averages of 10 force controlled indents per condition, for four peak force conditions of 750, 900, 2000 and 4000 μN. Pile-up was observed to increase with penetration depth and it varied for the different surfaces. At very shallow penetration depths, pile-up was assumed to be zero because it was indistinguishable from the specimen surface roughness. 70

Figure **3.7**: Average reduced elastic modulus (E_r) as a function of the average maximum penetration depth for the surfaces subjected to acidic (pH 0.9), neutral (pH 7.1) and alkaline (pH 9.5) surface cleaning treatments. Data plotted represent the mean of 10 force controlled indents per condition, for four peak force conditions of 750, 900, 2000 and 4000 μN. Reduced elastic modulus was observed to decrease with penetration depth up to ~100 nm and then reach a near constant value. Also, the reduced elastic modulus was dependent on the nature of the surface cleaning treatments that the surfaces were subjected to. 72

Figure **3.8**: Average hardness (H) as a function of the average maximum penetration depth for the surfaces subjected to acidic (pH 0.9), neutral (pH 7.1) and alkaline (pH 9.5) surface cleaning treatments. Data plotted represent

the mean of 10 force controlled indents per condition, for four peak force conditions of 750, 900, 2000 and 4000 μN. Hardness was found to increase with increasing penetration depth. Acidic and alkaline cleaning treatments lead to the decrease in the hardness for the air side of the float glass while it they lead to an increase in the hardness on the tin side of the float glass. 73

Figure **3.9**: Experimentally evaluated average percentage pile-up as a function of the average maximum penetration depth for the fresh, weathered and leached float glass surfaces. Data plotted are the averages of 10 force controlled indents per condition, for four peak force conditions of 750, 900, 2000 and 4000 μN. Pile-up was observed to increase with penetration depth and it varied for the different surfaces. 78

Figure **3.10**: Average reduced elastic modulus (E_r) as a function of the average maximum penetration depth for the fresh, weathered and leached float glass surfaces. Data plotted represent the mean of 10 force controlled indents per condition, for four peak force conditions of 750, 900, 2000 and 4000 μN. Reduced elastic modulus of the air side was found to vary with penetration depth and the different short-term corrosive exposure conditions. 80

Figure **3.11**: Average hardness (H) as a function of the average maximum penetration depth for the fresh, weathered and leached float glass surfaces. Data plotted represent the mean of 10 force controlled indents per condition, for four peak force conditions of 750, 900, 2000 and 4000 μN. It is observed that the hardness is increases with increasing penetration depth. Hardness of the air side was found to decrease due to short-term corrosive exposure while there was a slight increase due to corrosion on the tin side. 81

Figure **4.1**: Tin concentration depth profiles for the air and tin sides of the 2, 6 and 8 mm thick aged SIV float glasses obtained by Secondary Ion Mass Spectroscopy (SIMS) [3]. It is observed that the tin sides contain as much as 10% (weight %) SnO_2 near the surface and this concentration decays rapidly to about 2% (weight %) at a depth of ~200 nm. Very low tin concentration (< 1%) is observed even on the air side of float glass. 87

Figure **4.2**: Experimentally evaluated average percentage pile-up as a function of the average maximum penetration depth for aged 2, 6 and 8 mm thick aged float glasses. Data plotted are the averages of 10 force controlled indents per condition, for four peak force conditions of 750, 900, 2000 and 4000 μN. Depth dependent pile-up variations are observed with the mean values of percentage pile-up lying between ~1 – 6%. At the very shallow depths pile-up was assumed to be inexistent since it was indistinguishable from the surface roughness of the samples. The length of the error bar on either side of a mean value is equal to the standard error of the mean. 90

Figure **4.3**: Reduced elastic modulus (E_r) is plotted as a function of the maximum penetration depth (h_{max}) for the air and tin sides of the 2, 6 and 8 mm thick, aged float glasses. Data plotted are the averages of 10 force controlled indents per condition, for four peak force conditions of 750, 900, 2000 and 4000 μN. It was observed that the tin side of any float glass had a greater E_r compared to its air side. Beyond 100 nm E_r was observed to be independent of penetration depth. 91

Figure **4.4**: Hardness (H) is plotted as a function of the maximum penetration depth (h_{max}) for the air and tin sides of the 2, 6 and 8 mm thick, aged float glasses. Data plotted are the averages of 10 force controlled indents per condition, for four peak force conditions of 750, 900, 2000 and 4000 μN. It was observed that the tin side of any float glass had a greater H compared to its air side. 92

LIST OF TABLES

Table **1.1**: The values of geometric correction factors suggested by King [48] 15

Table **2.1**: Force and Displacement specifications of the Triboindenter® three-plate capacitive transducer 22

Table **2.2**: Optimized gain settings used for displacement and force controlled indents 24

Table **2.3**: Optimized in-situ imaging gain settings 26

ACKNOWLEDGEMENTS

First and foremost, I would like to express my deepest gratitude and heartfelt thanks to Dr. Christopher Muhlstein, whose constant guidance and patience proved invaluable for the successful completion of this project. I would also like to thank my co-advisors, Drs. Carlo Pantano and David Green, for their advice and motivation throughout course of this project. I thank the National Science Foundation's Industry-University Center for Glass Research which provided the requisite financial support to carry out this project. Special thanks are due to Amber Romasco from the Muhlstein research group for her patient discussions and suggestions towards improving the data analysis algorithms used in this study. Special thanks are also due to Nicholas J. Smith from the Pantano research group for providing some of the float glass samples that were tested as a part of this project apart from his help with sample characterization using infrared and X-ray photoelectron spectroscopy. I further thank all the other members of the Muhlstein, Pantano and Green research groups for their suggestions and support during the course of my stay at Penn State. I extend thanks to the staff of the Pennsylvania State University's Material Characterization Laboratory, for training and support with instrumentation. Finally, I thank my family and friends who have perennially supported me.

Chapter 1
Introduction

This introductory chapter of the thesis is intended to cover the background information required for the reader to understand the nature, scope and implications of the current project. Initially, a summary of the technological relevance and the manufacturing process of float glass are provided in order to explain the origin of the compositional and related structural differences between the two surfaces of float glass (section **1.1**). Effects of the differences between the two surfaces of commercial float glass on its physical properties are then discussed in the light of the existing literature. This is followed by an overview of silicate glass corrosion in general and more specifically a discussion of the effects of corrosion on commercial float glass (section **1.2**). The necessity to evaluate and understand the mechanical behavior of the surface layers of the two float glass surfaces is then discussed. Further in this chapter (section **1.3**) the important features of the instrumented indentation technique are reviewed since this technique was used to evaluate the surface mechanical properties of float glass. The chapter ends with a brief outline of the structure for the rest of the manuscript.

1.1 Float Glass

Flat glass that is commonly used in a wide range of architectural, automotive and structural applications is commercially processed by the float process developed by

Pilkington Ltd. [1]. This process involves floating the molten glass melt on a bath of molten tin in what is called a float line. As a result of this high temperature interaction between molten glass and molten tin, there is tin diffusion into the surface layers of float glass. This compositional change induces a structural change within the local glass network. Each of these three aspects – processing, related compositional and structural changes along with their effects on the physical properties of the glass will be now discussed.

1.1.1 Float Glass Processing

A schematic illustration of the float process is shown in Figure **1.1**. The glass melt is allowed to enter the float line and spread on the molten tin bath in the form of a sheet (often referred to as a ribbon). The surface of the tin bath remains very flat thereby leading to a flat bottom face of the glass. Due to the forces of gravity and surface tension the top surface ends up being parallel to the bottom surface and extremely smooth, eliminating the need for any secondary processing treatments such as polishing. The temperature at the start of the float line is about 1100°C. The thickness of the ribbon is adjusted to the desired value by shaping and sizing the ribbon at the hot end of the float bath. The temperature within the float chamber gradually decreases with distance along the float line until it reaches about 600°C. At this point the glass sheet is viscous enough to be lifted off the float line using metallic rollers. The glass ribbon then passes through an annealing lehr to relieve any accumulated residual stresses. As the ribbon comes out of

the annealing lehr and the temperature drops to about 200°C it is removed off the processing line and allowed to cool to room temperature on the metallic rollers.

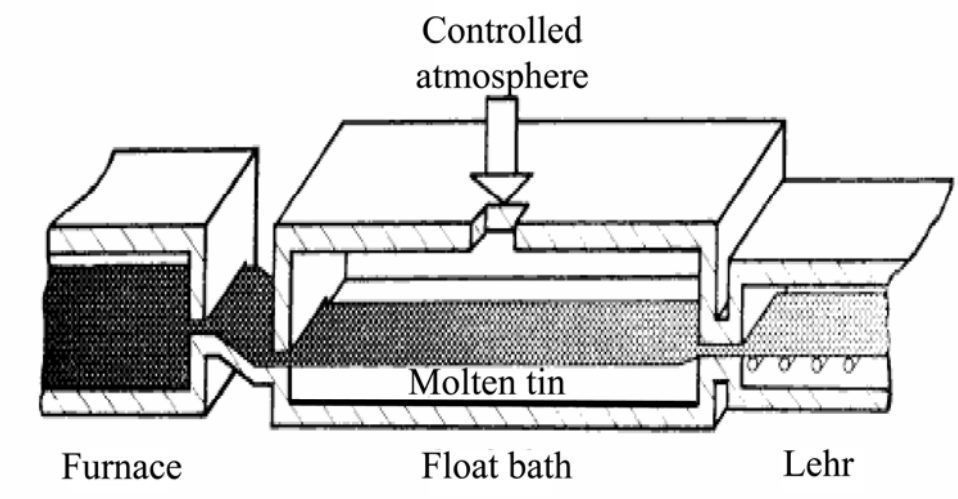

Figure **1.1**: Schematic illustration of the float process of manufacturing flat glass [1]. The molten glass in the furnace flows over molten tin in the float bath and solidifies along the length of the bath. It is then picked up by rollers and passed in the annealing lehr.

1.1.2 Compositional and Structural Variations in Float Glass

The float process leads to tin diffusion into the side that is in contact with the molten tin at a high temperature (henceforth referred to as the *tin side*) [1, 2]. The side opposite to the tin side is called the air side. Trace amount of tin had been observed on this surface [3] as a consequence of vaporization of molten tin within the float chamber. However, its exposure to a reducing environment (a mixture of hydrogen and nitrogen gasses) that is used to prevent the oxidation of molten tin within the float chamber leads

to surface de-alkalization of the air side [2]. Thus the two surfaces of a float glass have compositional differences and related structural differences. The objective of this project was to understand the effect of these structural differences on the mechanical behavior of the two surfaces.

Previous studies [2-9] had monitored the extent of tin diffusion on the tin side of float glass and diffused tin was observed up to a depth of ~40 microns. The maximum concentration of tin and the steepest gradient in the concentration of diffused tin were, however, limited to the first couple of hundred nanometers [3] beyond which the tin concentration decayed with increasing depth from the surface into the bulk of the glass. The effects of tin diffusion into silicate glasses on structure of the local glass network had been widely researched in the past with the material systems used being both float glasses [5, 6] and binary [10-14] or ternary [14-18] tin doped silicate glasses. The studies on both binary and ternary tin doped silicate glasses had indicated that tin diffusion into alkali silicate glasses modified the local glass structure. The diffused tin in these glasses had been shown to be present in the + 2 or +4 valence state. Using experimental techniques such as Mossbauer spectroscopy, nuclear magnetic resonance (NMR) or pulsed neutron diffraction these studies suggested that the Sn^{+2} was coordinated to three oxygen atoms in a pseudo tetragonal arrangement and had a lone pair of electrons. The Sn^{+4} in these stanno-silicate glasses was found to be smaller than Sn^{+2} content, but it was observed that Sn^{+4} was likely to posses a distorted octahedral configuration [18] and also was more rigidly bound to the glass structure than Sn^{+2} [19]. Based on the variations in physical properties of the tin doped glasses such as glass transition, density, thermal expansion and refractive indices with varying tin concentrations, a few earlier studies [11, 15, 16,

20] concluded that tin diffusion into float glass led to an increase in the connectivity of the local glass network. This increase in the connectivity of the local glass structure on the tin side was expected to increase its hardness and the elastic modulus compared to the surface without tin, as shown in the case of model tin doped silicate glasses [15, 20]. In addition to the compositional and related structural variations of the two sides of the float glass, another important difference between the air and tin sides was the relative increase in size and distribution of surface flaws on the tin side [21-23]. This relative increase in surface flaw size and distribution on the tin side is attributed to its contact with the rollers during the processing stage. Lower fracture strength observed on the tin side as compared to the air side was attributed this flaw size distribution [23].

1.1.3 Effect of Tin Diffusion on Physical Properties

The effect of tin diffusion into silicate glasses on a wide range of physical properties such as its optical, mechanical and thermal properties had been researched [11, 15, 20] in the past. Holland and Karim [11] during their work with binary SnO–SiO_2 glasses observed that doping silica with up to 30 mol% of SnO increased the density of the glass and the thermal expansion while decreasing the glass transition temperature, indicating that tin was breaking up the structure of the glass and acting as a network modifier. However, they also observed that tin did not de-polymerize the silica network as much as Na and Pb. Further, they observed that as the SnO concentration increased beyond 30 mol% there was an inflection in the thermal expansion trends, suggesting that tin was no longer breaking up the silica network and that its structural role had changed.

Le Bourhis [15] in his work on soda-lime-silica glasses doped with 5 – 10 mol% SnO_2 observed that tin infusion increased the hardness, viscosity and refractive index of the glass while decreasing the thermal expansion, thereby suggesting that SnO_2 diffusion led to an increase in the connectivity of the local glass structure. The tin concentration in these studies was however, higher than those usually observed in commercial float glasses. Krohn *et al.* [20] studied tin doped soda-lime-silica glasses with tin concentrations (both SnO and SnO_2) in the range of 0 – 3 mol% to mimic the tin concentrations observed in commercial float glasses. They observed an increase in viscosity and a decrease in thermal expansion with increasing concentrations of either SnO or SnO_2. Elastic modulus measured by sonic resonance was also reported to increase with increasing SnO or SnO_2 concentrations thereby suggesting that these low concentrations of tin diffusion were indeed increasing the connectivity of the local glass network. They further realized that the ratio of SnO_2 to SnO influenced the extent of this increase in connectivity. Based on these doped glass studies it was expected to observe an increase in the surface elastic modulus and hardness of commercial float glasses which were known to contain both Sn^{+2} and Sn^{+4}.

Some studies on the strength of the two different surfaces of float glass have reported that they exhibit differences in their strength, with the air side being stronger than the tin side [21, 24]. Tummala and Foster [21] attributed the higher strength of the air side to the generation of compressive residual stresses due to surface de-alkalization during the float process. They further reported that the tin side was more resistant to stress corrosion compared to the air side. Akcakaya *et al.* [24] and Krohn *et al.* [23], from their studies on float glasses attributed the lower strength of the tin side to greater

severity of flaws introduced on this surface due to contact with rollers during processing rather than compressive stresses on the air side. Akcakaya et al. [24], contrary to the observations of Tummala and Foster [21], reported that the air side was more resistant to stress corrosion compared to the tin side. Such contradictory reports had created ambiguity regarding the exact role of diffused tin on the strength of commercial float glasses. Similar ambiguity exists in published literature regarding the hardness of commercial float glass surfaces measured using nanoindentation [22, 25-27]. Ramsey and Whitehead [25], from their nanoindentation tests on commercial float glass surfaces observed that there was no difference in the load-displacement curves obtained on either the air side or the tin side and therefore concluded that there was no difference between the hardness and elastic modulus of the two sides. Later Goodman and Derby [26] reported that contrary to expectations, the elastic modulus and hardness of the air side were greater than those of the tin side. More recently, Howell *et al*. [27] had reported that there was a near 10% elevation in hardness (measured via nanoindentation) of the tin side at shallow penetration depths (i.e., within the first 100 nm from the free surface) while at greater penetration depths there was not much difference. These contradictory results from published literature suggest that the role of tin diffusion on the mechanical properties of materials is not clearly understood. One of the objectives of this project was to understand the cause of these contradictory conclusions in previously published results and this will be discussed in Chapter 4.

1.2 Float Glass Corrosion

Alkali silicate glasses have been known to corrode under seemingly innocuous environments such as atmospheric humidity and liquid water. Glass corrosion in aqueous solutions is considered to occur in two stages [28]. The 1st or primary stage involves an exchange of the alkali constituents from the glass for the hydrogen ions (H^+) or hydronium (H_3O^+) in the corrosive medium as shown in Figure **1.2**. The secondary stage involves the dissolution of the leached layer due to a breakdown of the silica network according to the second reaction in Figure **1.2**.

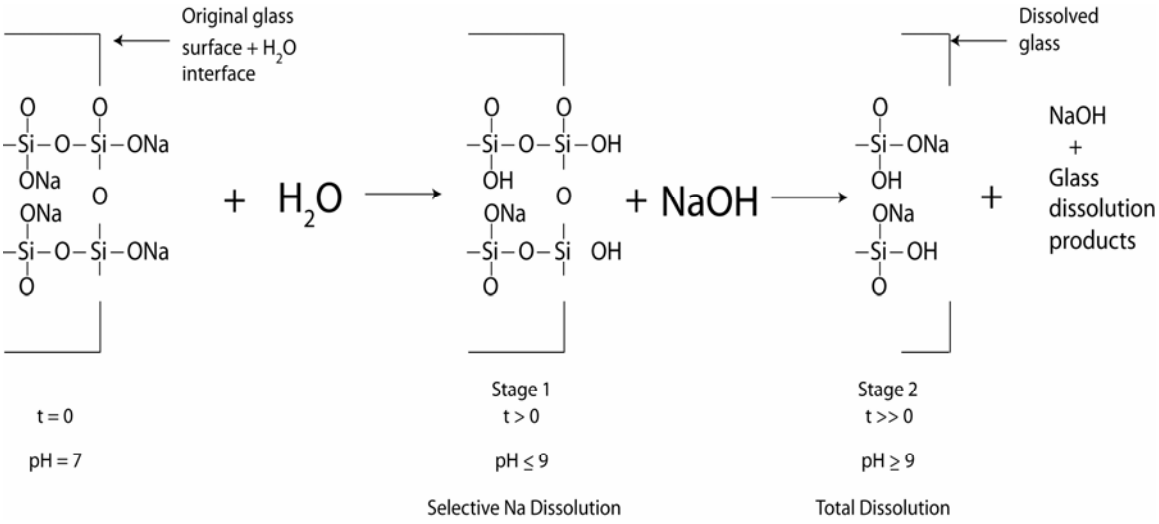

Figure **1.2**: Illustration of the two stages/mechanisms of corrosion of alkali silicate glasses [28].

Weathering of alkali silicate glasses refers to the process of leaching and dissolution of glass network when exposed to atmospheric humidity. Weathering may also be categorized into two different types: Type 1 weathering when the moisture in the environment condenses onto the surface in the form of visible drops which later 'run off' the surface and Type 2 weathering where the thin surface layer of condensate evaporates

before the formation of visible drops and run off [28]. The pH of the corrosive solution has also been shown to affect the kinetics and mechanism of both forms of corrosion (leaching and weathering). It had been reported that the ion exchange mechanism mentioned initially in Figure **1.2** is prevalent for solution pH values under 9. The corrosion mechanism involving the breakdown of the silica network is prevalent at pH values greater than 9. Bunker [29] also reported that the kinetics of hydration, network hydrolysis and ion exchange reactions were dependent on the local glass structure and, the presence of the specific reaction sites and functional groups within the glass structure. Probably for this same reason it had been observed that the corrosion resistance of the two sides of a float glass was different, with the tin side being more resistant to corrosion than the air side [30-34] . Pantano [31] reported that the Na release rate was greater on the air side due to leaching in deionized water as compared to the tin side. Shelby and Vitko [30] reported visual observations of surface degradation on the two sides of float glass due to weathering. They had observed no significant corrosion on the tin side of float glass after 4 weeks of exposure to 98 – 100% relative humidity while they observed spalling on the air side. On the basis of dye penetration tests it was established that the air side was more porous than the tin side after corrosion. Resonant nuclear reaction profiling was applied to both the surfaces of weathered float glass and it was observed that the proton penetration depth was significantly greater on the air side than the tin side. It was thus suggested that the resistance to proton penetration was the cause for the improved corrosion resistance of the tin side of float glass. Mingquin *et al.* [32] evaluated the resistance of tin doped soda-lime-silica glasses against water based corrosion. They reported that the tin doped glasses were more resistant to glass corrosion compared to the

glass that was not doped. However, these latter studies [30, 32] suggested that the higher CaO content observed on the corroded tin side relative to the corroded air side might also be the cause of the improved corrosion resistance of the tin side. It had been consistently reported that the corrosion modified surface layers of float glass were a few tens or, at times, a couple of hundred nanometers in thickness [34-38]. Such thin corrosion modified surface layers were capable of altering not only the adhesion characteristics and scratch resistance of glasses but had often been reported to affect glass fracture strength by modifying the resistance to crack propagation [39]. Therefore, for the obvious reasons, it is useful to understand the mechanical behavior of these modified surface layers. The technique of nanoindentation, due to its capability to evaluate small volumes of material, was chosen to evaluate mechanical properties such as the elastic modulus and hardness of the nanoscale corrosion modified surface layers in commercial float glasses and these results will be discussed in Chapter 3. In the ensuing section we shall provide a brief background of the technique of nanoindentation and the related data analysis methodology.

1.3 Nanoindentation

Indentation testing techniques involve the deformation of a material whose mechanical properties have to be evaluated by penetrating it with a relatively harder indenter tip of known geometry. Projected contact area between the indenter tip and the sample is an important metric used to evaluate the hardness and elastic modulus of the sample material. However, at the nanoscale it is cumbersome and at times even

impossible to image the residual indent and determine the contact area thereof. To overcome this difficulty, the applied force (P) and corresponding displacement (h) of the indenter tip are recorded continuously during a nanoindentation test and the resulting P-h data are analyzed to evaluate the projected contact area and a wide range of mechanical properties of the materials. Such indentation techniques that rely on P-h data and not on the residual indentation impression are called instrumented or depth-sensing indentation techniques. The most commonly evaluated mechanical properties via instrumented indentation are the elastic modulus and hardness of the material. Over the years the process of evaluating elastic modulus and hardness from the P-h data has undergone considerable change and currently the model proposed by Oliver and Pharr [40] is widely used. Initially, the development of Oliver-Pharr method of instrumented indentation data analysis and the basic relations involved therein are presented (section **1.3.1**) after which attention is drawn to the possible sources of errors in nanoindentation testing and data analysis methods (section **1.3.2**). The specific details regarding the testing and data analysis methodology employed during this study to reduce or eliminate these errors will be presented in Chapter 2.

1.3.1 Analysis of Nanoindentation Force-Displacement Data

The force (P) – displacement (h) curves obtained during instrumented indentation typically contain at least two segments – the *loading segment* during which the indenter is driven into the material as a result of the applied force and the *unloading segment* during the indenter is pulled away from the material by releasing the applied force. A schematic

illustration of a typical *P-h* curve with labeled loading and the unloading segments is presented as Figure **1.3**. At times a third segment referred to as the *hold period* is interjected between the loading and unloading segments where the material is subjected to a constant peak force for a specified amount of time before proceeding to the unloading segment.

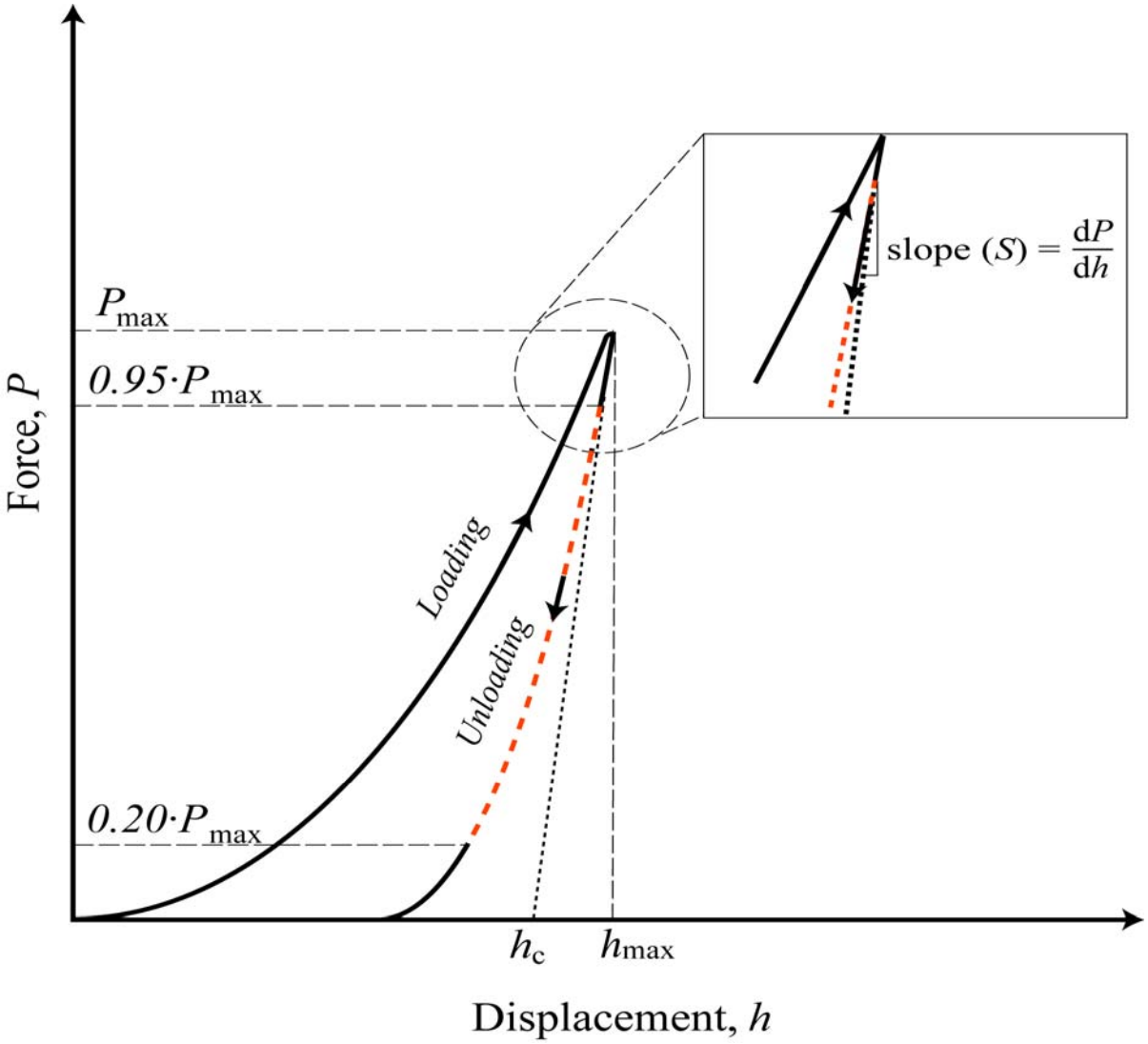

Figure **1.3**: Schematic illustration of a typical nanoindentation load (*P*) – displacement (*h*) curve depicting some important data analysis parameters.

Both the loading [41-44] and unloading [40, 45] segments of instrumented indentation data had been analyzed to evaluate the mechanical properties of the materials tested. Sharp indenter tip geometries had been commonly used during nanoindentation tests and elastic-plastic materials tend to undergo near instantaneous plastic deformation when loaded under these tips. The loading curve analyses therefore reported the estimation of lumped parameters such as (E/H). The unloading curve analyses, however, assumed that the elastic component of the deformation suffered by a material during the loading segment was recovered during the unloading segment, and therefore provided the elastic modulus (E). In the current study, the most commonly used unloading curve analysis – the Oliver-Pharr (O-P) model [40] – was employed to evaluate the elastic modulus and hardness of the float glass surfaces. A brief overview of the development of O-P analysis from Sneddon's analysis for indentation with a cylindrical flat punch will [46] will be presented below.

Sneddon [46] derived general relationships between indentation load, displacement and contact area as given by Equation **1-1** for the process of indenting an elastic half space with a rigid flat cylindrical punch.

$$S = \frac{dP}{dh} = \frac{2}{\sqrt{\pi}} \cdot \sqrt{A_c} \cdot \frac{E}{\left(1 - \nu^2\right)} \qquad \text{(Eq. } \mathbf{1\text{-}1}\text{)}$$

The differential on the left side of this equation represents the slope of the initial portion of the unloading segment, A_c is the projected contact area at this point while E and ν are the elastic modulus and Poisson's ratio of the material respectively. The slope of the initial portion of the P-h curve is an experimental measure of the stiffness (S) of the

material. Doerner and Nix [45] observed that for most metals, the unloading curve was linear over a large range. Linearity of the unloading curve suggested that the contact area was constant during the unloading segment. Thus, based on the assumption that at least the initial portion of the unloading curve was linear, Doerner and Nix suggested that Sneddon's relationship, which was originally developed for the flat punch geometry, could be applied to other indenter geometries without any modification. Later Oliver and Pharr [40] noted that the unloading curves for a variety of materials such as ceramics and glasses were non-linear and best described by a power law fit thereby rendering the Sneddon's relation to be inapplicable to any indenter geometry other than the flat punch. Pharr *et al.* [47], however, discovered that Sneddon's solutions for flat punch geometry were actually applicable to the indentation of an elastic half space with any axi-symmetric indenter geometry that was a smooth (i.e., infinitely differentiable) body of revolution, independent of the shape of the unloading curve. Though the commonly used sharp indenter geometries such as the Berkovich indenter could not be classified as smooth bodies of revolution, finite element analysis studies by King [48] showed that the general Sneddon's relation was still applicable for such indenters with triangular and square cross sections if a correction factor β was used to account for a deviation from the flat punch geometry as given by Equation **1-2**.

$$S = \frac{dP}{dh} = \frac{2}{\sqrt{\pi}} \cdot \sqrt{A_c} \cdot \beta \cdot \frac{E}{\left(1-\nu^2\right)} \qquad \text{(Eq. 1-2)}$$

Suggested values for β are mentioned in Table **1.1**

Table **1.1**: The values of geometric correction factors suggested by King [48]

Indenter Geometry	**β**
Circular cross sections	1.000
Triangular cross sections	1.034
Square cross sections	1.012

Based on their observation of non-linearity of the unloading curve, Oliver and Pharr [40] suggested a power law curve fit of the form given in Equation **1-3** instead of a linear curve fit wherein A, h_f and m were the curve fit parameters. The parameter h_f represents the depth of the residual indent.

$$P = A \cdot \left(h - h_f\right)^m \qquad \text{(Eq. 1-3)}$$

The stiffness of the material can be experimentally determined as given by Equation **1-4** based on the curve fit in Equation **1-3**.

$$\left(\frac{dP}{dh}\right)_{P_{\max}} = A \cdot m \cdot \left(h - h_f\right)^{m-1} \qquad \text{(Eq. 1-4)}$$

As mentioned previously, Equation **1-2** was developed for the case of a perfectly rigid indenter. However, the commonly used diamond indenters are not perfectly rigid. Therefore Equation **1-2** was modified to Equation **1-5** in order to account for the elasticity of the indenter into Sneddon's original formulation. E^* in Equation **1-5** is called the contact reduced elastic modulus and is based on the Hertz theory of contact between two elastic bodies. It is defined as given by Equation **1-6.**

$$S = \left(\frac{dP}{dh}\right)_{P_{\max}} = \frac{2}{\sqrt{\pi}} \cdot \sqrt{A_c} \cdot E^* \cdot \beta \qquad \text{(Eq. 1-5)}$$

$$\frac{1}{E^*} = \frac{\left(1-\nu_s^2\right)}{E_s} + \frac{\left(1-\nu_i^2\right)}{E_i} \qquad \text{(Eq. 1-6)}$$

Therefore using E_i = 1141 GPa and ν_i = 0.07 [49] for the diamond indenter tip used during this study we can calculate the reduced elastic modulus of the sample (E_r) given by Equation **1-7**.

$$\left(\frac{1}{E_r}\right) = \left[\frac{1}{E^*} - \frac{\left(1-\nu_i^2\right)}{E_i}\right] = \frac{\left(1-\nu_s^2\right)}{E_s} \qquad \text{(Eq. 1-7)}$$

If the Poisson's ratio of the material is known, the elastic modulus of the sample (E_s) could be evaluated. In order to determine the reduced elastic modulus using Equation **1-5** we need an independent measure of the projected contact area (A_c).Therefore, prior to performing the indentation tests on the desired samples A_c is commonly calibrated as a function of the contact depth (h_c) by performing indentation tests on a reference glass of known E_s and ν_s. The procedure for evaluation of indenter tip area function will be discussed later in section **2.2.5**. Contact depth (h_c) is calculated using Equation **1-8** and Equation **1-9** where ε is a geometric correction factor that helps in the accurate evaluation of the contact depth for indenter geometries other than a flat punch. For a spherical indenter (used in the current study), ε was taken to be 0.75 [40].

$$h_c = h_{\max} - h_a \qquad \text{(Eq. 1-8)}$$

$$h_a = \varepsilon \cdot \frac{P_{\max}}{S} \qquad \text{(Eq. 1-9)}$$

Oliver and Pharr [40] defined the hardness (H) of the material as the mean pressure it can support under load. Based on this definition hardness was computed according to Equation **1-10** where P_{max} was the maximum applied force and A_c was the projected contact area.

$$H = \frac{P_{max}}{A_c} \qquad \text{(Eq. 1-10)}$$

1.3.2 Errors Associated with Nanoindentation Testing and Data Analysis

Mechanical properties of materials as measured by nanoindentation could be inaccurate owing to errors introduced at various stages of nanoindentation testing and data analysis. Therefore, in order to successfully use nanoindentation testing it was necessary to understand the origin of such errors and their effect on the final results. A few earlier studies had discussed the various types of errors occurring during nanoindentation and their effects on the final results [50, 51]. Menčík and Swain [50] presented a comprehensive list of errors and their effects on the measured mechanical properties. These errors included, inaccurate load-cell calibration that affects the accuracy of recorded *P-h* data, inaccurate machine compliance calibration, thermal drift in the instrument, non-ideality of the indenter tip geometry, erroneous determination of initial point of contact, pile-up around the indenter tip, sample surface roughness, inelastic effects during unloading, viscoelastic recovery of material during unloading, and inhomogeneity or spatial variations in measured mechanical properties. A few other errors included the accuracy of the correction factors ε and β used during OP analysis

and, the effect of the residual stresses in the material on the measured mechanical properties and trends. For some of the errors listed above, the magnitude of the error could be assessed and accurate corrections could be performed on the final nanoindentation results while in the case of a few other errors such as inelastic effects during unloading, it is difficult to accurately evaluate and account for them in the final analysis. In these cases, however, certain measures had to be taken, to reduce the adverse effects of such errors on the final nanoindentation results. In the current study, efforts were taken to eliminate or limit the adverse effects of many of these errors and these details are presented in Chapter 2.

1.4 Thesis Structure

The ensuing chapter will present the details of the nanoindentation testing and data analysis methodologies that were employed in the current study to evaluate the reduced elastic modulus and hardness of the float glass surfaces as accurately as possible. The methodology and testing parameters presented in this chapter were used throughout this study on all the surfaces that were tested. Chapter 2 will also discuss the efforts taken to reduce the errors involved in nanoindentation data analyses along with the details of the custom developed MATLAB® algorithms that were used to analyze the nanoindentation data. Chapters 3 and 4 of this thesis will discuss the results from the studies on commercial float glass surfaces. In Chapter 3 the results from the nanoindentation testing of a 2 mm thick fresh float glass subjected to controlled exposure conditions will be presented. The effects of controlled surface cleaning treatments and

short-term corrosive exposure conditions on the nanomechanical properties of the two different float glass surfaces will be discussed. The implications of these results on the usage of silicate glasses as nanoindentation calibration standards will also be discussed. Chapter 4 evaluates the role of tin diffusion and long-term exposure history in controlling the surface mechanical response of the 2, 6 and 8 mm thick, aged commercial float glass surfaces whose tin diffusion profiles had been characterized in the past. These results of nanoindentation testing of the aged float glasses are discussed in conjunction with the results from the nanoindentation testing of the fresh float glass presented in Chapter 3 and it will be shown that exposure history has a dominant influence on the mechanical behavior of float glass surfaces. It will be further shown that tin diffusion into the float glasses, affects the mechanical behavior of float glass surfaces under the dominating influence of exposure history.

Chapter 2
Nanoindentation Methodology and Data Analysis

2.1 Nanoindentation Test Setup

In order to successfully perform a nanoindentation test it was imperative to understand the important features of the nanoindenter and evolve an efficient test protocol. These preliminary aspects will be given consideration in the current section. Initially the specifications of the nanoindenter will be presented (section **2.1.1**). Important features of the nanoindenter such as feedback control during indentation and the ability to perform AFM imaging with the in indenter tip (in-situ AFM) are then detailed (section **2.1.2**). Further, the various instrument gain settings and imaging parameters that were commonly employed for all indentation tests in this study will be listed. The general sequence of events associated with getting the nanoindenter and the test specimen ready for a nanoindentation test are then presented (section **2.1.3**).

2.1.1 The Nanoindenter

The nanoindenter used in this study was the Hysitron TriboIndenter® (Minneapolis, MN) – a commercial nanoindentation system that was capable of automated indentation testing, scratch/wear testing and in-situ Atomic Force Microscopy (AFM), (i.e., the same tip used for nanoindentation could also be used as an AFM probe). It was accompanied by TriboScan™ – a data analysis software that not only controlled the nanoindenter but was also capable of measuring the instrument drift and correcting for it,

performing Oliver-Pharr analysis on indentation data and inverse Oliver-Pharr analysis to evaluate the tip area function apart from a few other features. While most of the data analyses were performed using custom MATLAB® algorithms, drift measurement and corrections were applied using Triboscan™. The instrument was capable of very fine positioning control in three (X, Y and Z) axes. The sample stage was attached to the X-Y stage of the instrument that had a positioning resolution of 500 nm. The indenter tip was mounted on the fine scale positioning system that was in turn mounted on the Z-stage. The fine scale positioning of the indenter tip was achieved by a three-axis piezo scanner because it had a superior resolution compared to the XYZ stages. The piezo scanner was designed to achieve a resolution of 20 nm in the XYZ directions. Its range was, however, limited to 60 μm in the XY directions and 3 μm in the Z direction. The TriboIndenter® came with optics (also mounted on the Z-stage) to aid in preliminary magnified view of the samples. The magnification capability of the optics was 500 – 3500×. TriboIndenter® was also provided with vibration isolation features. For all vibrations less than 200 Hz the instrument could actively damp vibrations by using a system of peizo-electric accelerometers and piezo-dynamic transducers. Larger frequencies were passively damped out by placing the instrument on a granite base. The indenter also had an acoustic encapsulation to reduce noise levels due sound around the indenter and avoid air currents around the indenter tip. The relative humidity in the laboratory was 40 ± 5% and the temperature was 20 ± 2°C. The TriboIndenter® used a three-plate capacitive force transducer that could be operated with or without feedback control, to apply the desired force on the indenter tip and measure the corresponding displacement. Application of the specified force was achieved by applying an appropriate voltage bias to the transducer's

bottom plate. The transducer's load and displacement specifications in the X and Z directions are noted in Table **2.1**. The Z direction parameters are relevant for indentation tests.

Table 2.1: **Force and Displacement specifications of the Triboindenter® three-plate capacitive transducer**

	X – Axis	Z – Axis
Load Resolution	2 μN	1 nN
Load Noise Floor	10 μN	ff
Maximum Force	2 mN	10 mN
Displacement Resolution	4 nm	0.04 nm
Displacement Noise Floor	10 nm	0.2 nm
Maximum Displacement	15 mm	20 mm
Thermal Drift	< 0.05 nm/s	< 0.05 nm/s

2.1.2 Nanoindentation Testing Parameters

To perform an indentation test with the nanoindenter either under displacement control or force control, it was necessary to input a few feedback parameters. Similarly, a few feedback parameters and dimensional specifications had to be specified by the user in order to capture in-situ AFM images of the indented regions. In this section of the thesis, the details of these indentation and imaging feedback control parameters will be presented. Both displacement and force controlled indentation tests were performed during this study and therefore the specifications of the waveforms used for either of these modes will be presented. The different parameters mentioned here were employed for all the indentation tests performed during this study.

2.1.2.1 Feedback Control

In an instrumented indentation test the user specifies either a maximum penetration depth or a maximum indentation force to be applied on the material in a given time. Usually, based on the calibration of the electrostatic force constant of the transducer that preceded an indentation test, the bias voltage required to be applied to the bottom plate of the transducer plate was calculated. However, the application of this bias voltage usually would not yield the maximum force or displacement desired. This was because of a spring constant (k) associated with the center plate. From Equation **2-1** it is evident that the final actual force applied is usually lesser by an amount kx.

$$F_{actual} = F_{applied} - kx \qquad \textbf{(Eq. 2-1)}$$

This problem was overcome by employing a feedback loop that continuously monitored the error (kx) between the actual force and the desired force. This error signal (kx) was used to calculate the correction that had to be made to the applied force in order to achieve the desired force output. Two types of feedback control modes were available on the TriboIndenter® – displacement control and force control. Displacement control mode was employed to perform indents on the reference glasses. Indentations were performed to peak displacements ranging from 10 nm to 500 nm in increments of 10 nm. At each peak displacement condition 10 indents were performed. Loading and unloading rates of 10 nm/s were used with a hold time of 30 seconds at the peak displacement, between the loading and unloading segments. The optimized gain settings for such displacement control indents are listed in **Table 2.2** [52]. During the nanoindentation tests on float glass surfaces whose results are discussed in the subsequent chapters, we employed the

force control mode of indentation. Loading and unloading rates of 175 μN/s were used with the loading and unloading segments being separated with a 30 second hold time. 4 peak load conditions of 750, 900, 2000 and 4000 μN were employed. The loading and unloading rates were determined such that they were very close to a rate of 10 nm/s used during displacement controlled indentation. The gain settings required to achieve the good force control on these float glass surfaces are listed in **Table 2.2.**

Table 2.2: Optimized gain settings used for displacement and force controlled indents

	Displacement Control	Force Control
Integral Gain	0.045	1.000
Pre-load Integral Gain	0.200	0.250
Lift - Integral Gain	0.010	0.010
Proportional Gain	0.100	-
Adaptive Gain	0.700	-
Derivative Gain	0.100	-

2.1.2.2 In-situ Imaging

The in-situ imaging mode of the TriboIndenter® allowed the use of the same tip that was used to perform an indentation test as an Atomic Force Microscopy (AFM) probe. This feature of the indenter was used to image the region of indentation before and after the indentation. The pre-indent images (images taken prior to indentation) helped in the assessment of the quality of the indents (i.e., regions with debris, that were indented were not considered for further data analysis). The post-indent images of the residual indent impression (obtained after indentation) were used to quantify the flow of material above the surface and around the indenter tip – called pile-up. Pile-up that was so

quantified experimentally was used to perform an important correction to the reduced elastic modulus and hardness results obtained by the Oliver-Pharr model. Pre-indent images were also used to estimate the upper bound value of pile-up for the very shallow indents on float glass (the maximum penetration depth conditions below 100 nm that will be discussed later) since the amount of pile-up for these indents was indistinguishable from the surface roughness. This will be discussed later in section **2.3.2**.

A very small contact force of 1 μN was used to obtain the pre- and post-indent images in order to avoid mechanical damage of the region being indented. The choice of the image scan size for each indent was based on the estimated lateral dimension of the indent. The estimated value of maximum penetration depth at a peak load (nominal value of pile-up based on a trial indent was included in this estimate) was used to determine the lateral indent diameter using Equation **2-2**.

$$d_{indent} = 2 \cdot \sqrt{\left((2 \cdot R \cdot h_{\max}) - \left(h_{\max}{}^{2}\right)\right)} \qquad \text{(Eq. 2-2)}$$

The image scan size was set to be twice the indent diameter (rounded to the next largest 0.5 μm for convenience). The distance between two consecutive indents was determined based on the indent diameter of the largest indent performed. The distance between two consecutive indents in any row and two adjacent indent rows was calculated to be 10 times the largest indent diameter (in all the rows) rounded up to the nearest 0.5 μm, to avoid the effect of interacting indentation stress fields. Since the maximum peak load condition was fixed for all the float glass samples evaluated in this study the distance between two consecutive indents and between two adjacent indent rows turned out to be 14 μm. The gain settings in the in-situ AFM imaging mode were also optimized based on

the glasses being tested. These are listed in **Table 2.3**. The same parameters were used for both pre and post indent imaging.

Table 2.3: Optimized in-situ imaging gain settings

Integral Gain	900
Digital Feedback Gain	900
Proportional Gain	0
Set Point	1 μN
Scan Rate	1 Hz

2.1.3 Sample Preparation

To collect reliable results from nanoindentation testing, it was imperative that the surfaces being indented were clean and free from debris. This required the surfaces to be cleaned prior to indentation. A study of the effects of short-term cleaning treatments on the mechanical behavior of float glasses was conducted and therefore they will be discussed later. Prior to cleaning the sample surface, a local coordinate system was marked on each specimen using Knoop indents as shown in Figure **2.1**. The orientation of the local coordinate system relative to the global coordinate system (the coordinate system of the indenter stage) was noted every time the sample was placed into the indenter and therefore the positions of the previous nanoindents could be tracked. All the samples had to be mounted onto to magnetic stainless steel substrates to facilitate their placement within the indenter. This was achieved by affixing the sample on to a stainless steel substrate using a cyanoacrylate adhesive, thereby completing the sample preparation.

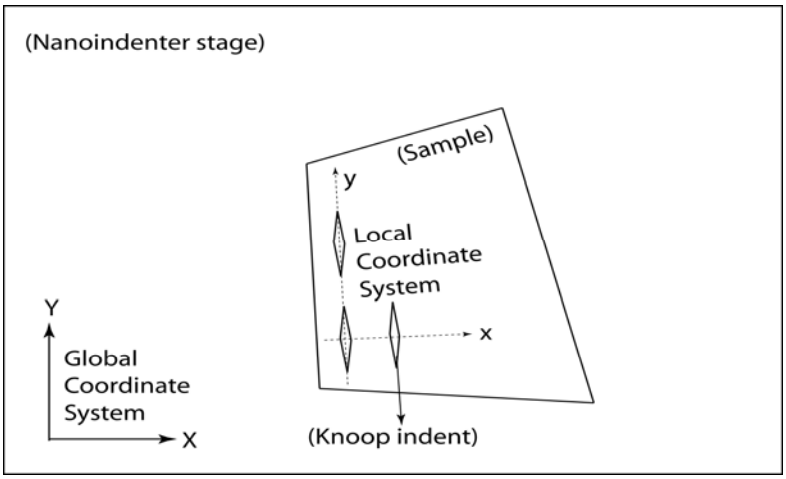

Figure **2.1**: A schematic illustration of a local coordinate system marked on the sample using knoop indents. The global coordinate system of the nanoindenter's stage is also shown in the figure.

2.2 Instrument Calibrations

In the current section attention will be focused on understanding the important calibrations that had to be performed on the nanoindenter before it could be used to test the samples of interest. These included the calibration of the transducer, evaluation of thermal drift in the instrument, the compliance of the instrument and the area function of the indenter tip that was used. Transducer calibration and evaluation of thermal drift were performed with the aid of TriboScan™. The calibration procedures for evaluating the machine compliance and the tip area function involved the indentation of a reference material and the analysis of the resulting data from a large number of calibration indents. As previously mentioned, custom MATLAB® algorithms were used to perform these analyses and their working will be discussed within the relevant subsections. Prior to that,

the details of the reference calibration material used in this study will be presented in section **2.2.1**.

2.2.1 Calibration Material

Corning 1747f glass (henceforth referred to as C1737f glass for convenience), a thin, flat, alkaline aluminosilicate glass manufactured by the fusion drawing process was used as the calibration standard throughout this study. The primary reason for choosing C1737f as a calibration standard was the fact that it was not an 'anomalous' glass, unlike the commonly used reference glass, fused silica, which had shown densification under high pressures (like those experienced below an indenter tip) and during polishing treatments that were used to get a relatively smooth surface required for nanoindentation testing [53-58]. C1737f glass was also very thin and thus devoid of property gradients along the thickness, which was a basic requirement for a reference standard. Moreover, the fusion drawing manufacturing process ensured that these surfaces were very smooth (typically measured peak-to-valley surface roughness was within ± 1 nm) and hence secondary polishing treatments were not required. Polishing treatments have been known to adversely affect the surfaces of silicate glasses inducing permanent densification of the surface layers as thick as 70 nm [59]. However, it was observed that addition of modifiers to silica glass tend to reduced the densification [53, 54, 58]. Previous work on nanoindentation of silicate glasses [52] had also found that the use of C1737f glass in determining the area function was more accurate than a few other commonly considered glasses. This glass was primarily composed of SiO_2 (67.5 – 69%). It also had Al_2O_3 (9 –

11.5%), B_2O_3 (7 – 12%), CaO (5.0%), BaO (4.5%), MgO and SrO (1 – 1.5% each), and As_2O_3 (about 0.2%) [60].

The surface of the glass had to be cleaned in order to remove debris and other impurities that may have accumulated on it. The cleaning procedure, however, should not affect the chemistry and structure of the glass. Thus, a cleaning method where the sample was rinsed for 2 minutes in pH 4 Hydrochloric (HCl) acid followed by an isopropyl and acetone rinse (3 minute each) [61] was used. A cotton swab was used to gently dry the surface immediately after removal from the acetone solution. The sample was then left in lab air to dry for 2 minutes prior to mounting it on the stainless steel substrate to perform indentation testing.

2.2.2 Transducer Calibration

The accuracy of nanoindentation testing relied primarily on the accuracy of the measurements of the applied force (P) and corresponding penetration depth (h) of the indenter. As mentioned in section **2.1.1** the P-h measurements of the indenter were carried out a using a three plate capacitive transducer. Due to the application of a certain voltage across the nanoindenter's capacitive transducer, the transducer plates moved by an amount equal to the desired displacement (under displacement control mode) or moved by a distance sufficient to apply the desired force (under force control mode). The conversion factor that was used to calculate the voltage to be applied based on the user-defined force or displacement was called the electrostatic force constant (ESF) of the transducer. The transducer's ESF was calibrated before starting any indentation

experiment. An air indentation procedure was used to calibrate the transducer during which a 600 μN peak force, 2 segment air indent was performed in 20 seconds. The ESF was calculated by TriboScan™ software. This calibration was performed prior to each experimental run and the calculated ESF value was used by the instrument to calculate the applied force during a test.

2.2.3 Thermal Drift

The displacement measurements of the nanoindenter are affected by thermal fluctuations and noise around the indenter. The nanoindenter setup used in this study did have some features to damp out noise within a certain frequency range as described earlier (section **2.1.1**) but there was no temperature control in the nanoindentation setup, thus making it necessary to account for the thermal drift in the instrument. Drift measurements were performed by monitoring instrument drift for 60 seconds before each indent was performed. During these 60 seconds the indenter tip engaged the surface in the force control mode at a contact force of 1 μN and the corresponding changes in displacement were tracked. Data from the last 30 seconds of this 60 second drift monitoring period were automatically fit to a straight line equation on the TriboScan® software. The slope of this straight line was then defined as the instrument drift rate ($\dot{D}$) and the output data from the indenter were corrected for this drift rate according to Equation **2-3** where t was the time (in seconds) at the instant when the displacement was recorded. To ensure high quality indentation tests, the MATLAB® based data analysis algorithm was designed to check the absolute value of measured drift rate that was saved

in the .lfb (force controlled tests) or .dfb (displacement controlled tests) files obtained from the nanoindenter for each indentation test and only indents with a measured drift rate within ± 0.1 nm/s were considered for further data analysis.

$$h_{drift-corrected} = h_{drift-uncorrected} + (\dot{D} \cdot t) \quad \text{(Eq. 2-3)}$$

2.2.4 Machine Compliance Calibration

The nanoindenter was ready to perform indentation testing after the transducer calibration was performed and the thermal drift evaluation methodology was decided. Later during the analysis of nanoindentation data, the stiffness (*S*) of the specimen being tested turned out to be an important mechanical parameter that was used in calculating its reduced elastic modulus (Equation **1-7**). Stiffness was the inverse of compliance (*C*) as given in Equation **2-4**. However, the compliance measured during the nanoindentation tests was the sum of both sample compliance and machine compliance as noted in Equation **2-5**.

$$S = \frac{1}{C} \quad \text{(Eq. 2-4)}$$

$$C_{total} = C_{sample} + C_{machine} \quad \text{(Eq. 2-5)}$$

Thus an accurate evaluation of the machine compliance was crucial to the determination of the actual compliance of the sample. Machine compliance was determined by performing a series of indents on the reference glass sample of known mechanical

properties. The method described by Hay and Pharr [62] was then used to iteratively compute the machine compliance as will be explained below.

Total compliance of the sample was obtained from the force-displacement curve (shown in Figure **1.3**) of an indent if the *P-h* data was not corrected for any value of machine compliance. When corrected for a value of machine compliance, the slope of the unloading segment of the *P-h* curve provided the sample compliance. Also the sample compliance was related to the projected contact area (A_c) as given by Equation **2-6** where E_r was the reduced modulus of the sample (in the case of the reference glass this was a constant) and β was a constant for a given geometry of the indenter.

$$C_{\text{sample}} = \frac{\sqrt{\pi}}{2.\beta.E_r} \cdot \frac{1}{\sqrt{A_c}} \qquad \textbf{(Eq. 2-6)}$$

Substituting Equation **2-6** into Equation **2-5** we end up with the proportionality given in Equation **2-7**.

$$C_{total} \propto \frac{1}{\sqrt{A_c}} \qquad \textbf{(Eq. 2-7)}$$

Contact area itself is a function of the contact depth, h_c of the indenter. Contact depth is calculated according to Equation **1-8**. For a spherical indenter, the ideal contact area, A_c for a contact depth h_c is given by Equation **2-8** .

$$A_c = (-\pi \cdot h_c^{\,2}) + (2 \cdot \pi \cdot R \cdot h_c) \qquad \text{(Eq. 2-8)}$$

When $h_c < 2R$, Equation **2-8** can be simplified to Equation **2-9**.

$$A_c = (2 \cdot \pi \cdot R \cdot h_c) \qquad \text{(Eq. 2-9)}$$

Therefore, based on Equation **2-6** through Equation **2-9** we obtain a relation of the form presented in Equation **2-10** where K is a constant.

$$C_{total} \propto \frac{K}{\sqrt{h_c}} + C_{machine} \qquad \text{(Eq. 2-10)}$$

From Equation **2-10** it is evident that machine compliance would be the y-intercept on a plot of total compliance as a function of $\frac{1}{\sqrt{h_c}}$. Therefore C_{total} was plotted as function of the inverse square root of contact depth, $\frac{1}{\sqrt{h_c}}$, and a straight line was fit by the method of least squares. The y-intercept of this straight line was the newly calculated value of machine compliance, $C_{\text{m\#1}}$ (the subscript #1 denoted the machine compliance value after first iteration). The entire calibration data set (i.e., the load-displacement curves of all the calibration indents) was then corrected for this $C_{\text{m\#1}}$. Contact depth (h_{c}) was then calculated as mentioned earlier for the entire data set. The linear relationship between C_{total} and the compliance corrected h_{c} was evaluated again. The new y-intercept was called $C_{\text{m\#2}}$. If $C_{\text{m\#2}} = C_{\text{m\#1}}$, then this was considered the final calibrated value of machine compliance and $C_{\text{m\#1}}$ was used to correct all the *P-h* data. However, if $C_{\text{m\#2}} \neq C_{\text{m\#1}}$, then the entire calibration data set (i.e., the load-displacement curves of all the calibration indents) was uncorrected for the earlier applied machine compliance ($C_{\text{m\#1}}$) and corrected for the new machine compliance value ($C_{\text{m\#2}}$) using Equation **2-11.**

$$h_{corrected} = h_{uncorrected} + \left(\left(C_{m\#1} - C_{m\#2} \right) \cdot P \right) \qquad \text{(Eq. 2-11)}$$

The entire process stated above was repeated for the corrected data set which provided a new machine compliance value of $C_{m\#3}$. This iterative process ended when the applied value of machine compliance $C_{m\#(n)}$ was the same as the calculated value of machine compliance $C_{m\#(n+1)}$. Figure **2.2** depicts the final iteration for the machine compliance correction using displacement control indents on C1737f glass with maximum penetration depths in the range of 140 nm to 300 nm. The peak penetration depth was incremented by 10 nm and at each condition 10 indents were performed. The final value of C_m shown in Figure **2.2** was 2.11 nm/mN. Machine compliance was evaluated before each set of indentation experiments and was usually found to vary between 2 – 2.5 nm/mN. It had been reported [63] that machine compliance was not constant for the first few hundred nanometers of indentation. This was observed even in the current study. Machine compliance was evaluated using the procedure explained above for displacement controlled indents in the peak penetration depth range of 50 – 300 nm.

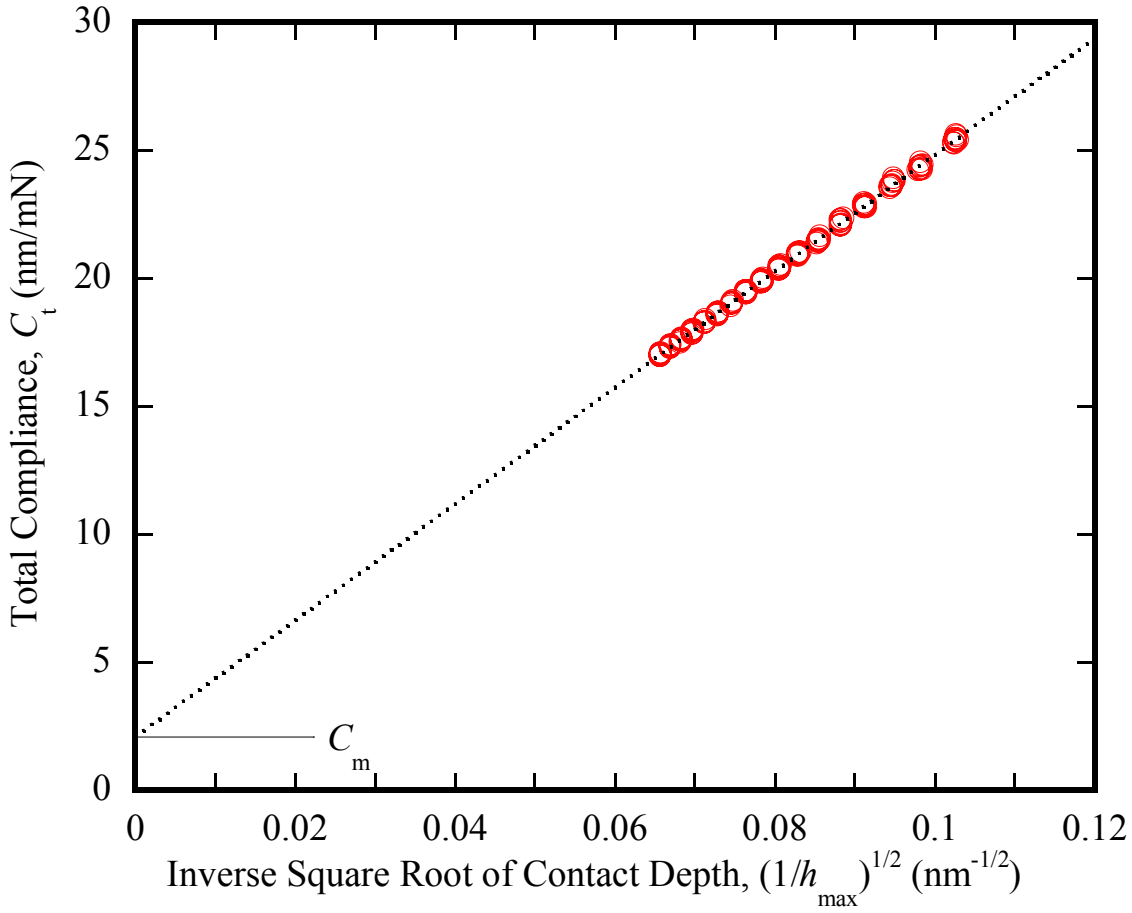

Figure **2.2**: Machine compliance correction performed using an iterative approach for displacement controlled indents on C1737f glass, with peak penetration displacement in the range of 140 – 300 nm. The figure shows the final iteration and machine compliance was determined to be 2.11 nm/mN.

It was observed that the final value of machine compliance increased rapidly when indents with a peak penetration depth of 130 nm or less were included in the analysis. The results are shown in Figure **2.3**. All through this study, a constant machine compliance value, calculated using 140 nm or deeper displacement controlled indents was used to correct the test data.

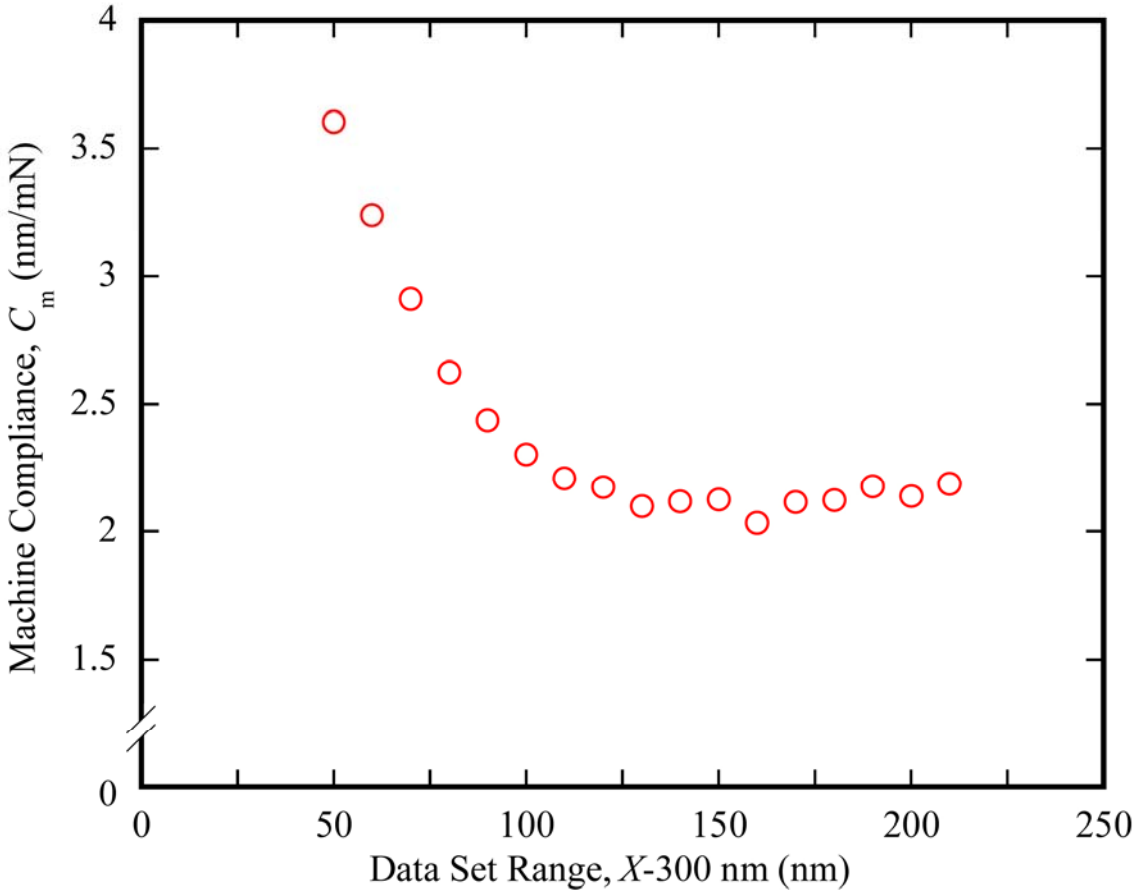

Figure **2.3**: Machine compliance as a function of the data set range, depicting the fact that machine compliance is a variable in the first hundred nanometers.

With the exception of a few technicalities, all the steps outlined above were implemented in the custom MATLAB® algorithm. The output data from the nanoindenter was always corrected for a machine compliance value of 2.47 nm/mN. Therefore, all data were initially stripped off this correction and the raw uncorrected data was then used as the input to the algorithm. Also, the iterative process ended when the calculated machine compliance was within 10^{-6} nm/mN the applied machine compliance. When the analysis

was terminated, the applied machine compliance was chosen as the final value of machine compliance.

2.2.5 Area Function Calibration

It was emphasized earlier that the technique of instrumented indentation, unlike most conventional indentation techniques, was dependent on the determination of the projected contact area (A_c) based on the force-displacement data. Ideally, the contact depth could be computed from the load-displacement data (Equation **1-8**) and the corresponding area function could be calculated if the indenter geometry was known (e.g, the ideal contact area for a spherical indenter is given by Equation **2-8**). However, the impossibility of manufacturing an indenter tip of ideal geometry at the nanometer length scale implied that an accurate experimentally verified indenter tip area function was required. The tip area function refers to a function that related a known contact depth (from a nanoindentation test) to the corresponding actual contact area.

A sphero-conical diamond indenter tip supplied by Hysitron Inc. with a nominal tip radius of 500 nm was used to perform all the indents in this study. The area function of this tip was determined by performing a series of displacement controlled indents on the C1737f reference glass. The displacement control conditions included peak displacement in the range of 10 to 500 nm in increments of 10 nm. 10 indents were performed at each condition. Inverse Oliver-Pharr analysis was performed on this set of load-displacement data following their correction for pile-up and machine compliance. Inverse Oliver-Pharr analysis referred to the use of Equation **1-7** for the calculation of

contact area from indents performed on a reference material of known depth-independent elastic modulus and Poisson's ratio. The elastic modulus and Poisson's ratio for C1737f were taken to be 70.9 GPa and 0.22 respectively [60] in the area function calculations. Contact depth (h_c) for these indents was also independently computed from the load-displacement data using Equation **1-8**. The area function was obtained by fitting a curve to A_c as a function of h_c. Figure **2.4** shows the experimental area function data and the fit area function for the sphero-conical diamond indenter tip used in this study. It demonstrates the importance of area function calibration by pointing out the difference between the actual and ideal area function curves. The actual area function shown in Figure **2.4** was also corrected for pile-up around the calibration indents. The correction of the area function data for pile-up will be described later in this chapter. The ideal area function was calculated on the basis of Equation **2-8** assuming a tip radius of 500 nm as per the manufacturer's quote.

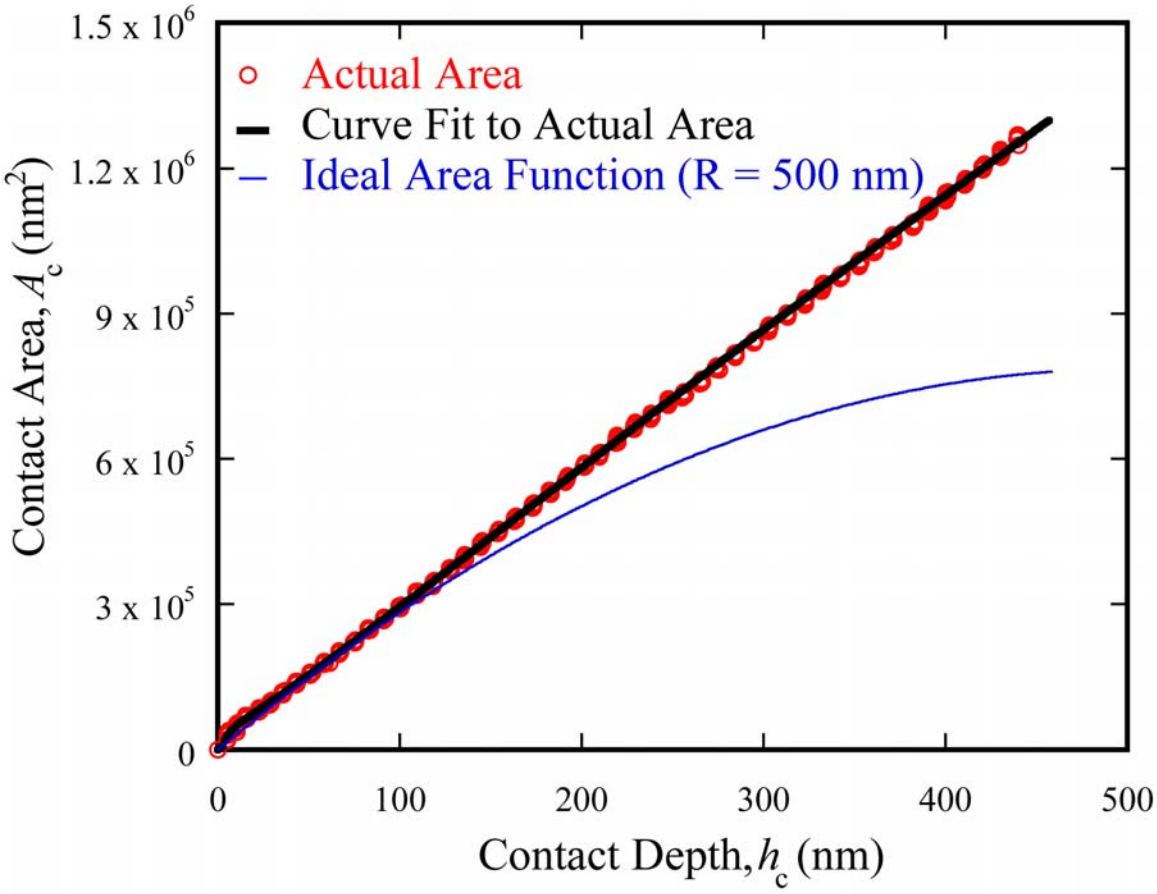

Figure **2.4**: Experimentally evaluated, pile-up corrected indenter tip area calibration function. The calibration standard used was Corning 1737f glass with an elastic modulus (E) = 70.9 GPa and Poisson's ratio (ν) = 0.22 [60]. Data in red circles depicts the experimentally evaluated area function while the solid black line represents the curve fit to this experimental data. It is this curve fit that is used as the indenter tip area function. The importance of this calibration is also projected by comparing the experimental results with an ideal tip are function that assumes ideal spherical shape for the indenter tip.

2.3 Nanoindentation Data Analysis

The Oliver-Pharr data analysis model of instrumented data analysis [40] was used in the current study to evaluate the reduced elastic modulus (E_r) and hardness (H) of the float glasses. While the fundamentals of this model and its development were mentioned

in Chapter 1, a few important modifications and corrections that were applied to it as a part of this study and will be highlighted in the current section. Custom MATLAB® algorithms were developed to incorporate such changes into the data analysis procedure. The objective of this section is to provide an insight into the nanoindentation data analysis methodology that was employed apart from elucidating on the important modifications or corrections to the Oliver-Pharr model. Wherever applicable, the details of the relevant features of the MATLAB® based data analysis algorithm will be embedded into the discussions.

As mentioned at the end of Chapter 1, there exist quite a few sources of inaccuracy in the process of instrumented indentation. The methodology adopted to tackle a few of these errors such as transducer calibration, thermal drift in the instrument, machine compliance and non-ideality of indenter tip geometry have already been discussed as a part of instrument calibrations earlier (section **2.2**). One error that was not corrected during the data analysis procedure was the error involved in evaluating the point of initial contact of the indenter tip with the specimen surface. The accuracy in evaluating the point of initial contact between the indenter tip and the sample had been noted to affect the accuracy of the measured elastic modulus and hardness [50, 51]. In the context of the current study, this error was eliminated at the data acquisition stage of nanoindentation when the TriboScan™ software recorded zero displacement (i.e., the initial point of contact) when the transducer sensed a contact force of 1 μN. A few other important errors that have not been addressed until now are the effects of inelastic and dissipative processes on the unloading behavior of the material, effects of pile-up around

the indents and surface roughness on the accuracy of the final results. Efforts taken to minimize or eliminate these errors will be discussed in this section.

2.3.1 Inelastic Effects

The Oliver-Pharr model for evaluating the elastic modulus of the material from the unloading curve was based on the assumption that the unloading segment of the indentation *P-h* response completely comprised of elastic recovery. In reality, however, the initial phase of the nanoindentation unloading response could be affected by creep, viscoelasticity and other relaxation processes. Also dissipative processes such friction and stick-slip effects could be prevalent during the final stages of the unloading. While these errors could not be accurately evaluated and eliminated, efforts were taken to reduce their adverse effects on the final nanoindentation results. These steps are discussed below.

In order to reduce the effects of time dependent material relaxation in the initial stages of the unloading curve, a 30 second hold period was employed between the loading and the unloading segments of each test. *P-h* data from the last 5 seconds of this 30 second hold period were fit to a straight line whose slope represented the creep in the material. It was observed that creep measured in this manner was always within the allowed drift rate range of ± 0.1 nm/s, suggesting that within the limits of the instrument drift rate there were no effects of creep on the unloading curve. It had been suggested by Mencik and Swain [50] that one of the ways to reduce the effects of creep in the initial stages of the unloading curve was by using a truncated segment instead of the entire

curve. Therefore, in the current study the initial 5% (relative to the peak force at the start of the unloading segment, i.e., $P_{\text{max-unload}}$) of the unloading curve was *not* considered during the Oliver-Pharr analysis (specifically in Equation **1-3**). In order to reduce the adverse impact of friction and slip-stick effects during the final stages of the unloading, the bottom 20% (again relative to $P_{\text{max-unload}}$) of the unloading curve was not considered during the Oliver-Pharr analysis. These changes were schematically depicted in Figure **1.3** where the truncated portion of the unloading curve considered for Oliver-Pharr analysis was shown in a dashed red line. The stiffness (S) from the unloading curve (Equation **1-7**) was evaluated at the peak force in this truncated section of the unloading curve, i.e., $0.95 \cdot P_{\text{max}}$.

2.3.2 Experimental Pile-up Correction

Plastic flow behavior around the indenter tip is divided into two categories: pile-up and sink-in. As the names suggest, pile-up refers to the accumulation of the material above the surface of the indented material around the indenter tip. Sink-in refers to the flow of material inwards around an indenter tip. The equations of nanoindentation were developed for elastic contact during which there is sink-in of material [46]. Pile-up of material around the indenter tip, however, affected the accuracy of the estimated contact depth and consequently the contact area. As illustrated schematically in Figure **2.5** the effect of pile-up was to increase the actual contact depth (and thus contact area), i.e., if pile-up was not considered, the contact depth as estimated by Oliver-Pharr analysis would be lower than the actual contact depth (and therefore the contact area). This

underestimation of contact area leads to an overestimation of elastic modulus (Equation **1-7**) and hardness (Equation **1-10**). Bolshakov *et al.* [64] observed that pile-up related error in modulus can be as high as 16% while the error in hardness can be as high as 60%. Based on previous studies on float glasses and tin doped glasses [15, 20] we expected the variations in the elastic modulus and hardness of the float glass surfaces in the current project to be less than the errors induced by pile-up. Thus, it was imperative that pile-up had to be accurately estimated and the final results had to be accordingly corrected in order to identify the correct trends in mechanical properties.

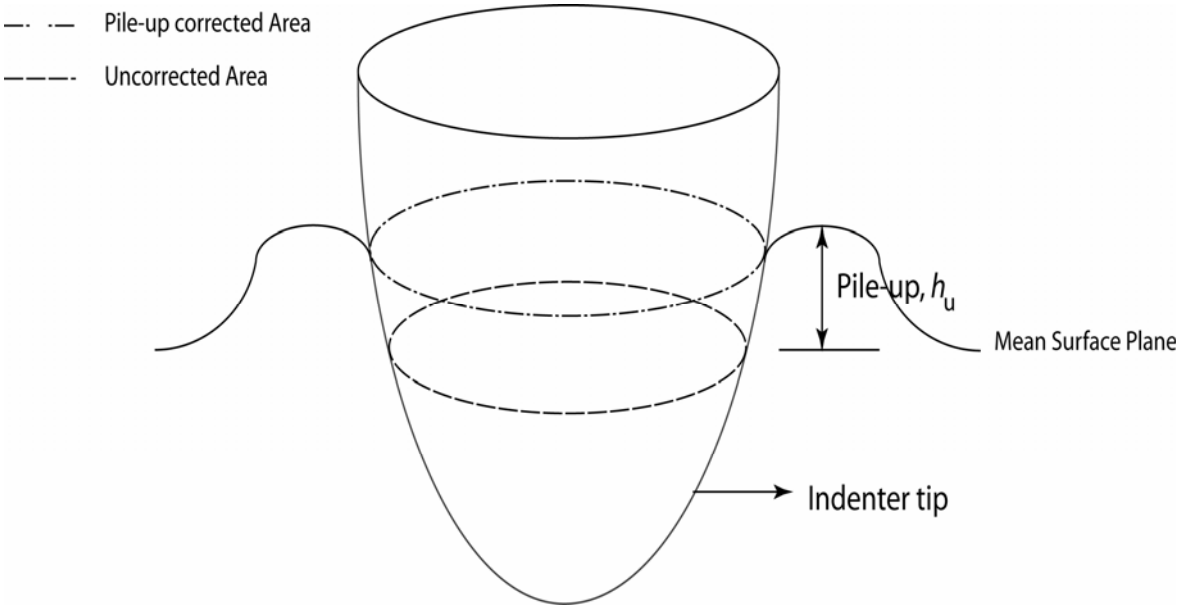

Figure **2.5**: Schematic depiction of the role of pile-up in increasing the projected contact area during indentation

Though a few models existed for estimating pile-up behavior in materials these had seen little or no experimental validation. More importantly these models were not developed for materials having a depth-dependent gradient in properties. Experimental pile-up estimations were thus necessary given the limitations of the existing pile-up

evaluation models. The in-situ AFM imaging capability of the nanoindenter presented an efficient way to image the indents and the pile-up around the indents. The post-indent in-situ AFM images obtained from every indentation test were processed using Scanning Probe Image Processing (SPIP™) software wherein the mean plane of the image was evaluated. The in-situ image data file was then converted to an ASCII file that was compatible with the MATLAB® algorithm used to quantify pile-up. The pile-up evaluation procedure is schematically illustrated in Figures **2.6** and **2.7** wherein the first step consisted of finding out the deepest point (A) in the residual indentation impression. Four line scans, each radiating from this deepest point and at 45° from each other were then used to evaluate the pile-up at 8 locations on the pile-up ring as shown in Figure **2.6**. Figure **2.7** shows the quantitative topographical information for each of these line scans. The peak heights on either side of the deepest point (A) along each line scan (shown using circles in the figure) were considered to be pile-up. The mean of these 8 values constituted the pile-up height for that particular indent. Further, at each force/displacement control condition 10 indents were performed and the average of the pile-up from these 10 indents was designated as the final average pile-up (h_u). Therefore, the reduced elastic modulus and hardness of all the 10 indents at a given condition were corrected for this final average value of pile-up.

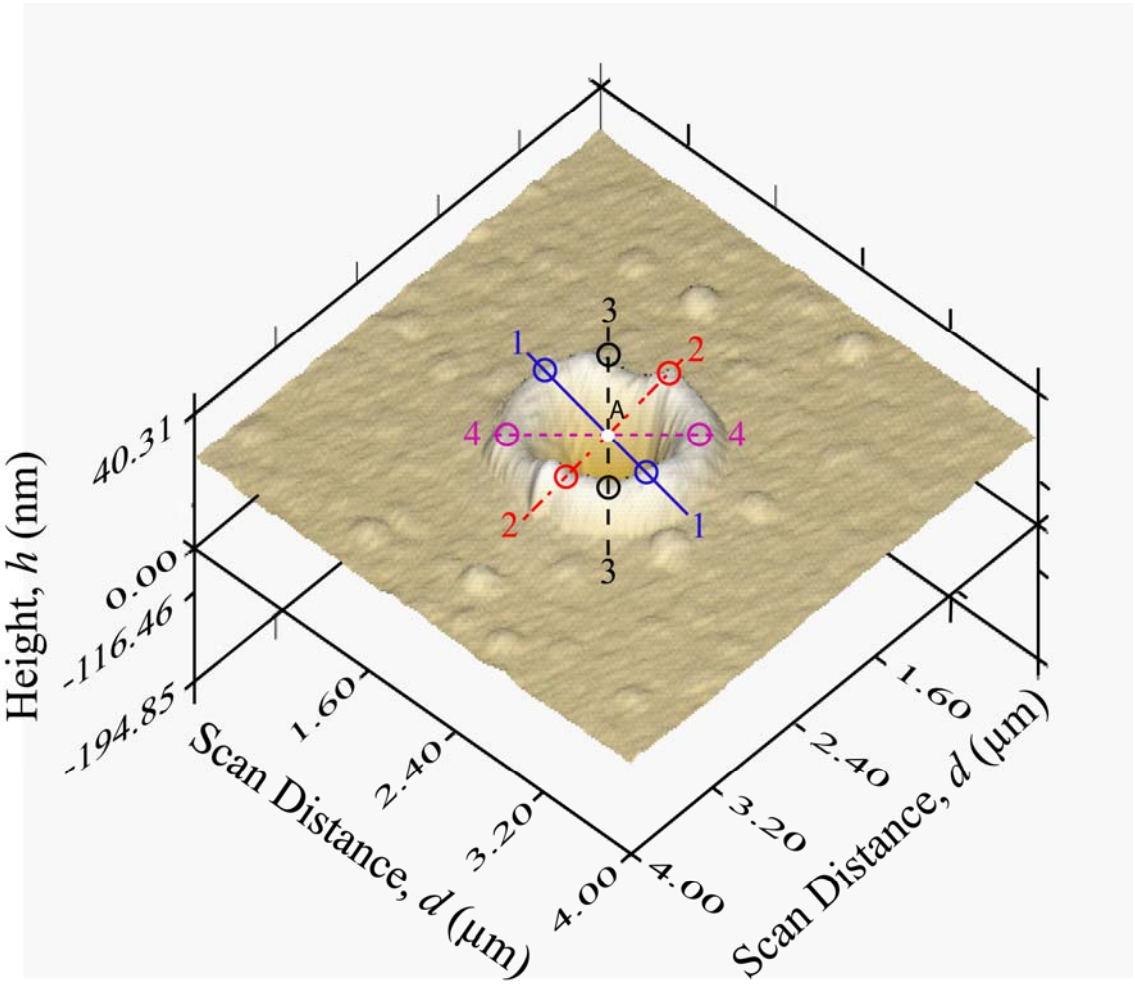

Figure **2.6**: A 3-dimensional post indent in-situ AFM image on float glass showing the pile-up around an indent along with the pile-up evaluation scheme that was employed in this study. The white circle denoted by A represents the deepest point in the residual indent impression. Four equiangular line scans (numbered 1-4) radiating from this point were used to capture the pile-up around the indent at 8 different locations as shown. The total length of each line scan was half the length of the dimensions of the image.

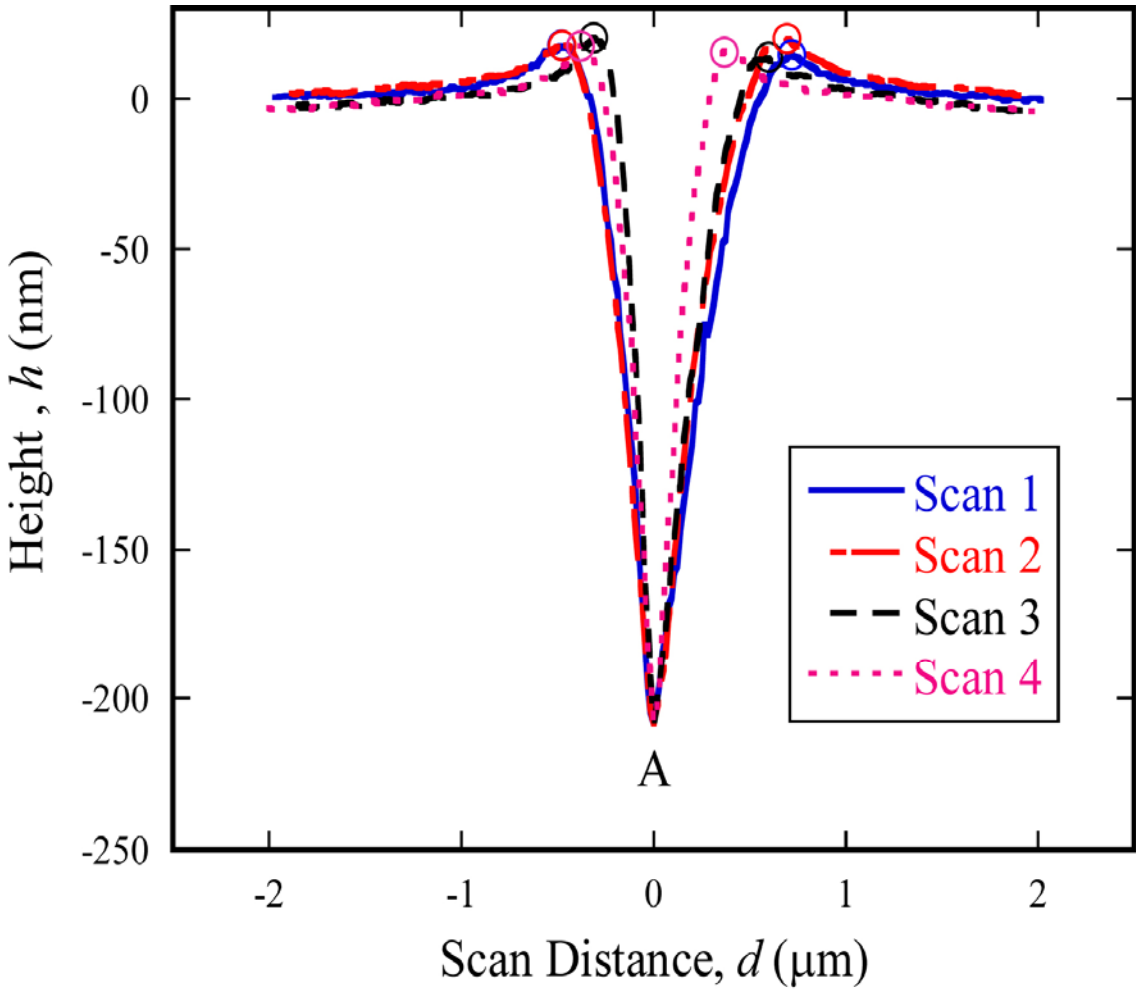

Figure **2.7**: Quantitative topographical data (height, *h*, above or below the mean surface plane) from the four line scans shown in Figure **2.6** plotted as a function of the lateral scan distance. The two peak points on either side of the deepest point (A) on the each line scan are marked in circles in this figure and they depict the values of pile-up captured by the MATLAB algorithm. The mean of these 8 values was denoted as the pile-up around the indent.

In the current study pile-up around indents was observed in both the reference (C1737f) glass and the float glass systems. Figure **2.8** depicts the experimentally determined pile-up (as a percentage of the maximum penetration depth) for the reference glass data used to calibrate the indenter tip area function. It can be observed that pile-up increased slightly with increasing penetration depth and lay between 3 – 6% of the peak indentation depth (h_{max}). Figure **2.9** presents an example of the pile-up that was observed on the air side of a 2 mm thick Guardian float glass. It was also observed in Figures **2.8** and **2.9** that initially the percentage pile-up was zero. This was because the experimental pile-up analysis procedure had a limitation on the minimum pile-up that could be evaluated owing to the roughness of the surface. Any pile-up below this threshold value could not be distinguished from the surface roughness. It was empirically determined that in order to distinguish pile-up from surface roughness the requirement mentioned in Equation **2-12** had to be met. R_{rms} in this equation indicated the root mean square surface roughness and was calculated according to Equation **2-13** where N was the number of data points from the image (was always 256× 256) and h_i was the deviation in height from the mean height $\bar{h}$. R_{rms} was calculated from the pre-indent in-situ AFM image data.

$$\frac{h_h}{R_{rms}} \geq 5 \qquad \text{(Eq. } \mathbf{2\text{-}12}\text{)}$$

$$R_{rms} = \sqrt{\frac{1}{N} \cdot \left(\sum_{i=1}^{N} \left(h_i - \bar{h} \right)^2 \right)} \qquad \text{(Eq. } \mathbf{2\text{-}13}\text{)}$$

During the evaluation of float glass surfaces presented later in Chapters 3 and 4, it was observed that for the 750 and 900 μN force controlled indents where the maximum penetration depths were usually less than 70 nm, the criterion in Equation **2-12** was not met. In such cases, the corresponding pre-indent images were evaluated to estimate the upper bound of possible pile-up around the indents. The heights of the asperities above the mean surface plane in the flattened pre-indent images were averaged and this average value was considered to be the upper bound of the pile-up around the indents under consideration. The reduced elastic modulus and hardness results at these shallow indents were then corrected for the estimated upper bound values of pile-up as described in later in section **2.3.2.2**.

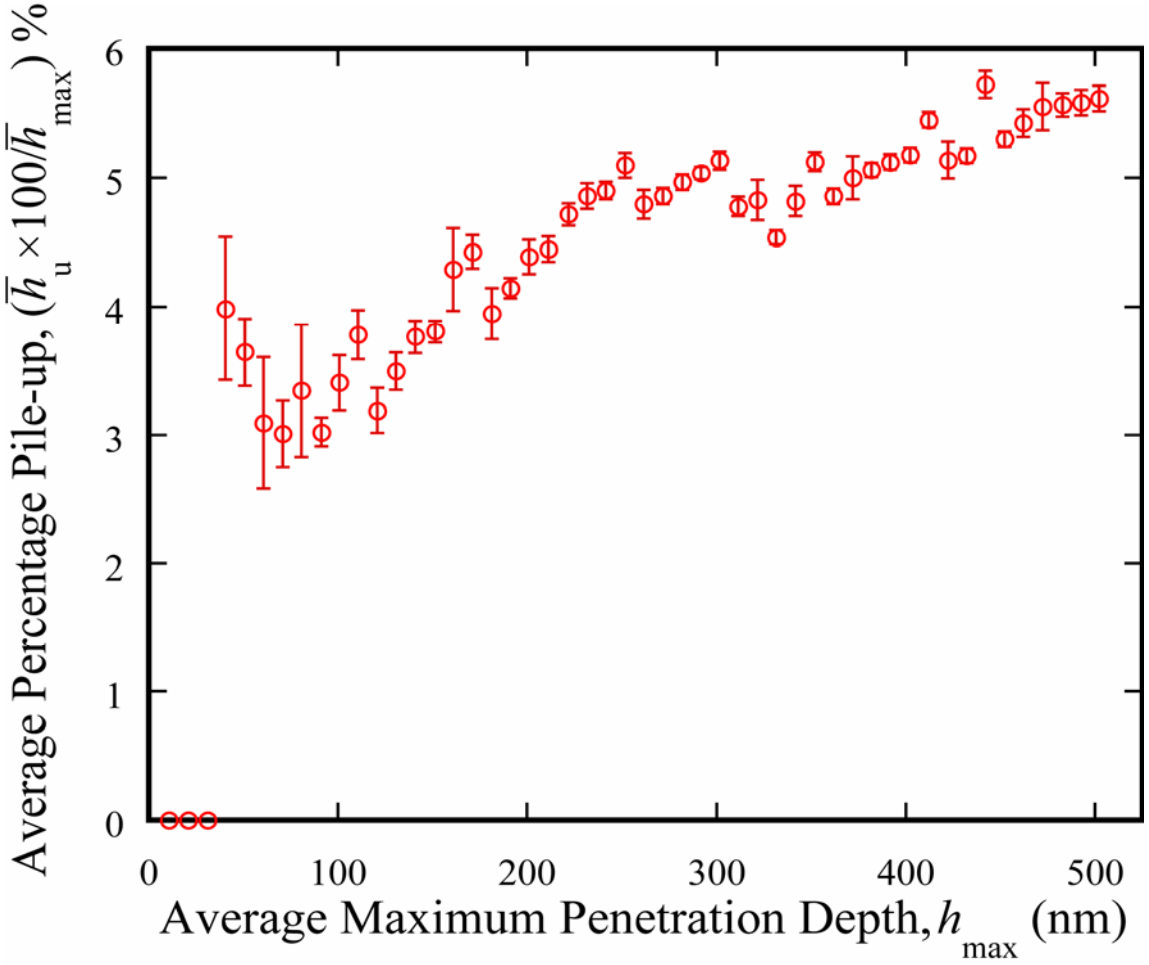

Figure **2.8**: Experimentally evaluated mean values of pile-up (expressed as percentage of the maximum penetration depth) are plotted as a function of average maximum penetration depth for the displacement controlled indents performed on the Corning 1737f calibration glass. It is evident there exists a measurable amount of pile-up in the reference glass that shows a slight increase as a function of the maximum indentation depth. This pile-up was taken into consideration during the evaluation of the tip area function shown in Figure **2.4**. Initial pile-up was indistinguishable from the surface roughness and hence considered to be inexistent. The error bars are one standard deviation in length on either side of the mean value.

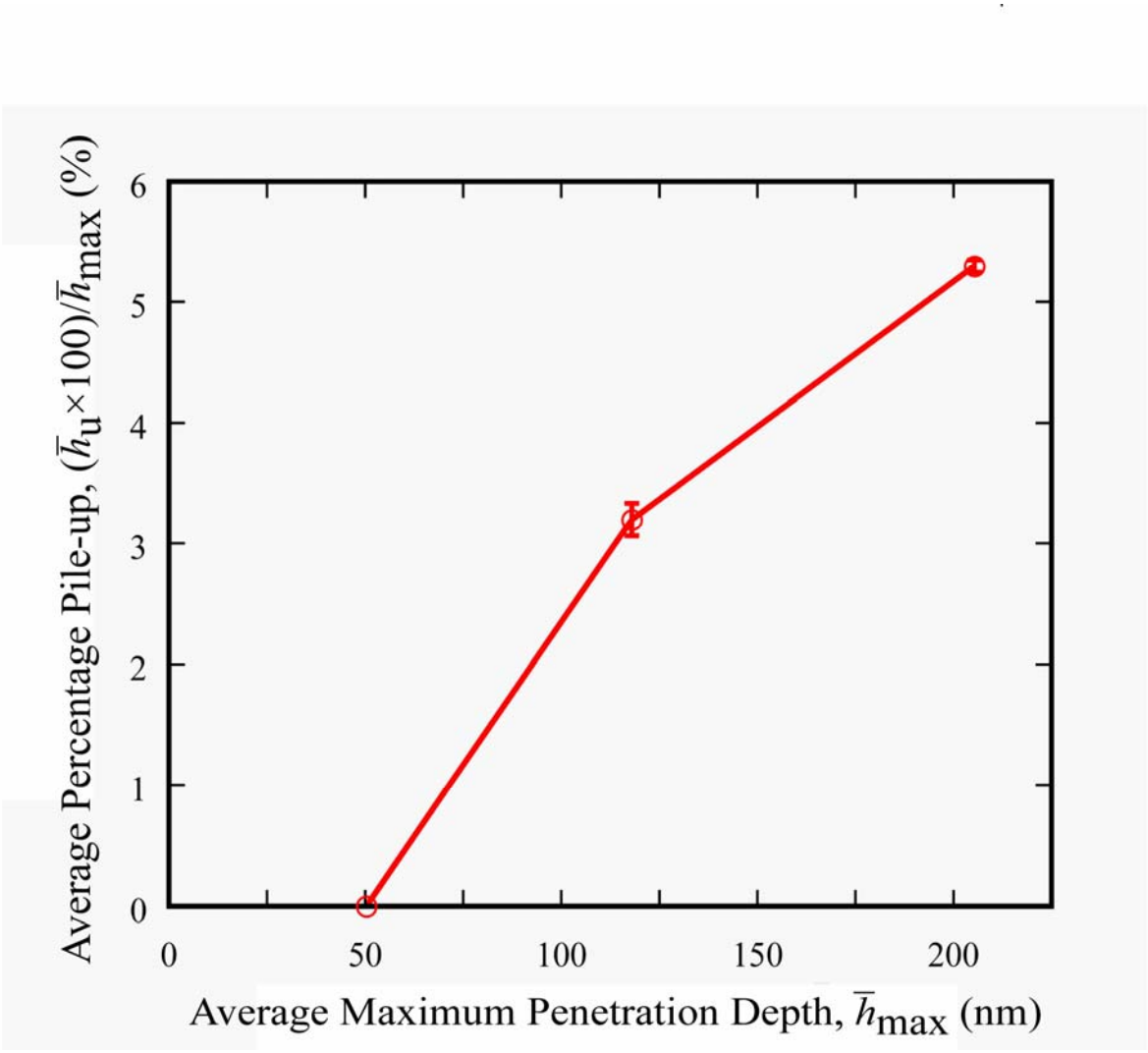

Figure **2.9**: Pile-up that was observed on the air side of a 2 mm thick Guardian float glass for the three different force control indentations where the peak indentation forces were 750, 2000 and 4000 μN. Pile-up was observed to increase with increasing peak force conditions.

While pile-up in the reference glass and the test samples was quantified using the same methodology specified earlier, there was a difference in the manner in which theses pile-up corrections were applied to the calibration indents and other test data and these differences will be discussed separately.

2.3.2.1 Pile-up Corrections for Area Calibration Data

According to Figure **2.5** the effect of pile-up is to increase the contact depth and projected contact area. The calibration indents on the reference glass were used to establish the contact area as a function of the contact depth. Therefore the contact area (A_c) and contact depth (h_c) were calculated independently as outlined in section **2.2.5**. A_c is dependent on the stiffness of force (P) – displacement (h) curves and the assumed material properties. The stiffness of the material was determined from the slope of the unloading P-h curve and the slope was unaffected by pile-up because pile-up, by definition, was plastic flow of material around the indenter tip and thus evolved continuously during the loading segment of an indentation test but not during unloading. Therefore the uniform pile-up correction (h_u) obtained via the analysis of the post-indent AFM impression could be applied to all the displacement values on the unloading segment. This would then shift the unloading curve by an amount equal to h_u along the x-axis as depicted in Figure **2.10**. Since contact depth was also independently evaluated and this calculation involved an exponential curve fit (refer section **1.3.1**) to a segment of the unloading curve, h_u was added to this entire unloading curve segment as shown in Figure **2.10** prior to the evaluation of contact depth from the unloading curve. Oliver-Pharr analysis of this corrected unloading curve provided the pile-up corrected contact depth. The effect of pile-up correction on the final calibrated tip area function is depicted in Figure **2.11**.

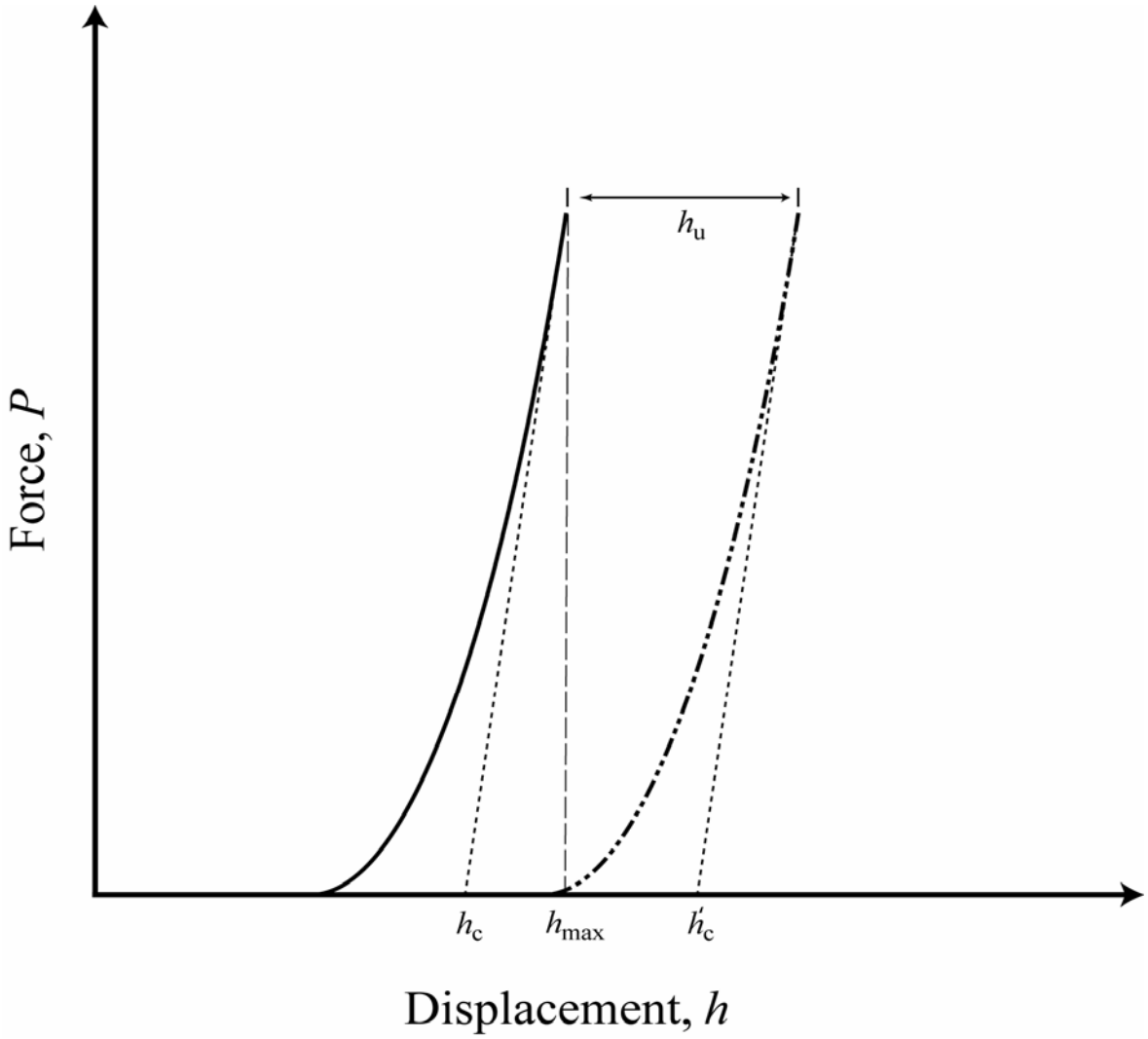

Figure **2.10**: Schematic depiction of pile-up correction procedure employed for indenter tip area function calibration data. The figure shows how the unloading segment of the force-displacement curve used for the area function calibration was modified based on the estimated pile-up.

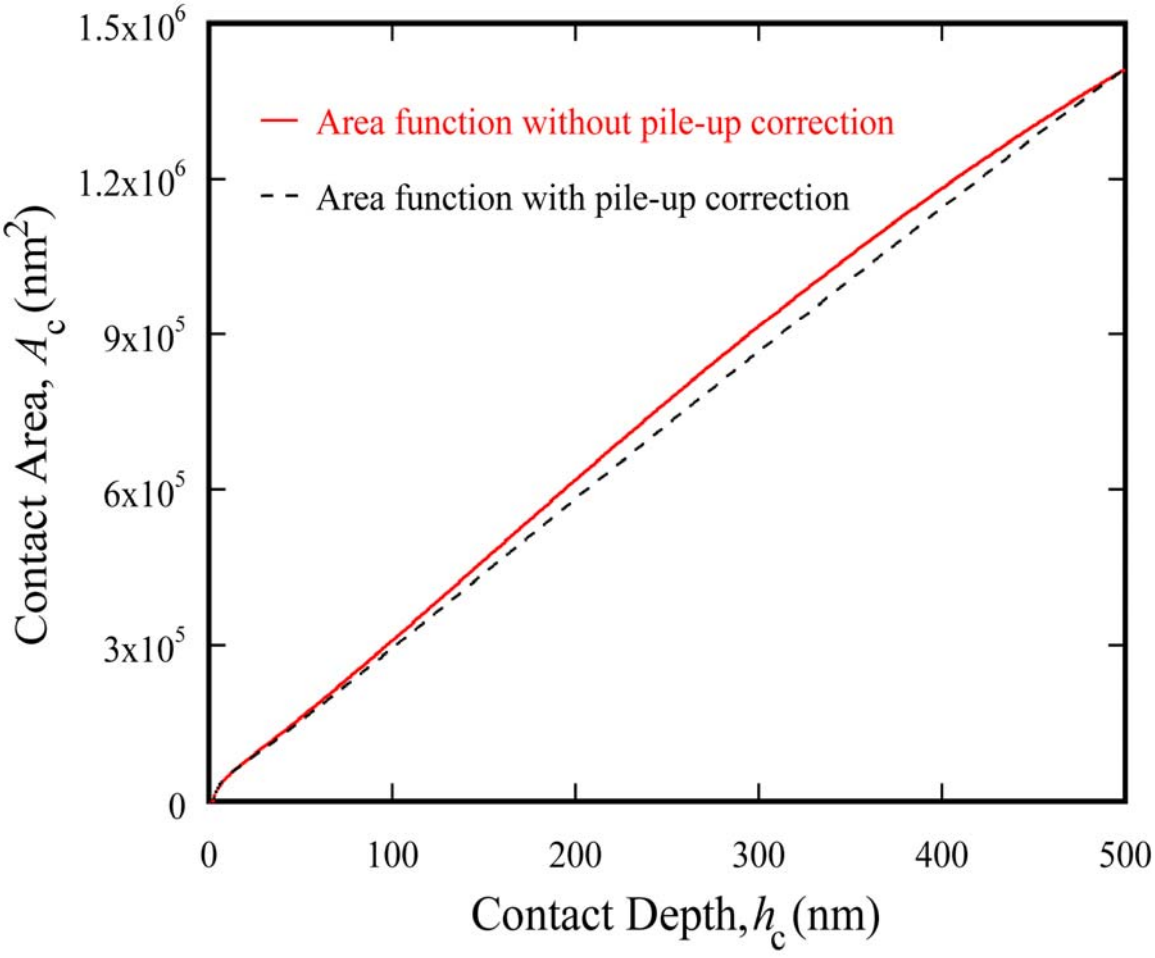

Figure **2.11**: The effect of pile-up correction on the calibrated indenter tip area function. The figure compares the area function curve that was calibrated without considering pile-up around the indents against the area function curve that was calibrated after correcting for the pile-up shown in Figure **2.8**.

2.3.2.2 Pile-up Correction for Test Data

As discussed earlier, the effect of pile-up was to increase the actual contact depth and thereby the actual contact area. While evaluating the reduced elastic modulus (Equation **1-7**) and hardness (Equation **1-10**) of the test specimens, the accurate projected

contact area (A_c) had to be known. Prior to the indentation testing of float glasses, the tip area calibration procedure had been performed and functional dependence of A_c on h_c was established. Once the contact depth was determined from the test data, the corresponding contact area was obtained based on the tip area function. Therefore, pile-up correction for test data was performed according to Equation **2-14** where $(h_c)_{\text{pile-up-uncorrected}}$ stood for the contact depth evaluated by the standard Oliver-Pharr analysis which did not account for pile-up. Figure **2.12** depicts the effect of pile-up correction on the reduced elastic modulus measurement for the air side of the 2 mm thick Guardian float glass whose pile-up behavior was shown in Figure **2.9**. A near 5% change in pile-up was observed to cause ~4% change in reduced modulus.

$$\left(h_c\right)_{pile-up\,corrected} = \left(h_c\right)_{pile-up\,uncorrected} + h_u \qquad \text{(Eq. 2-14)}$$

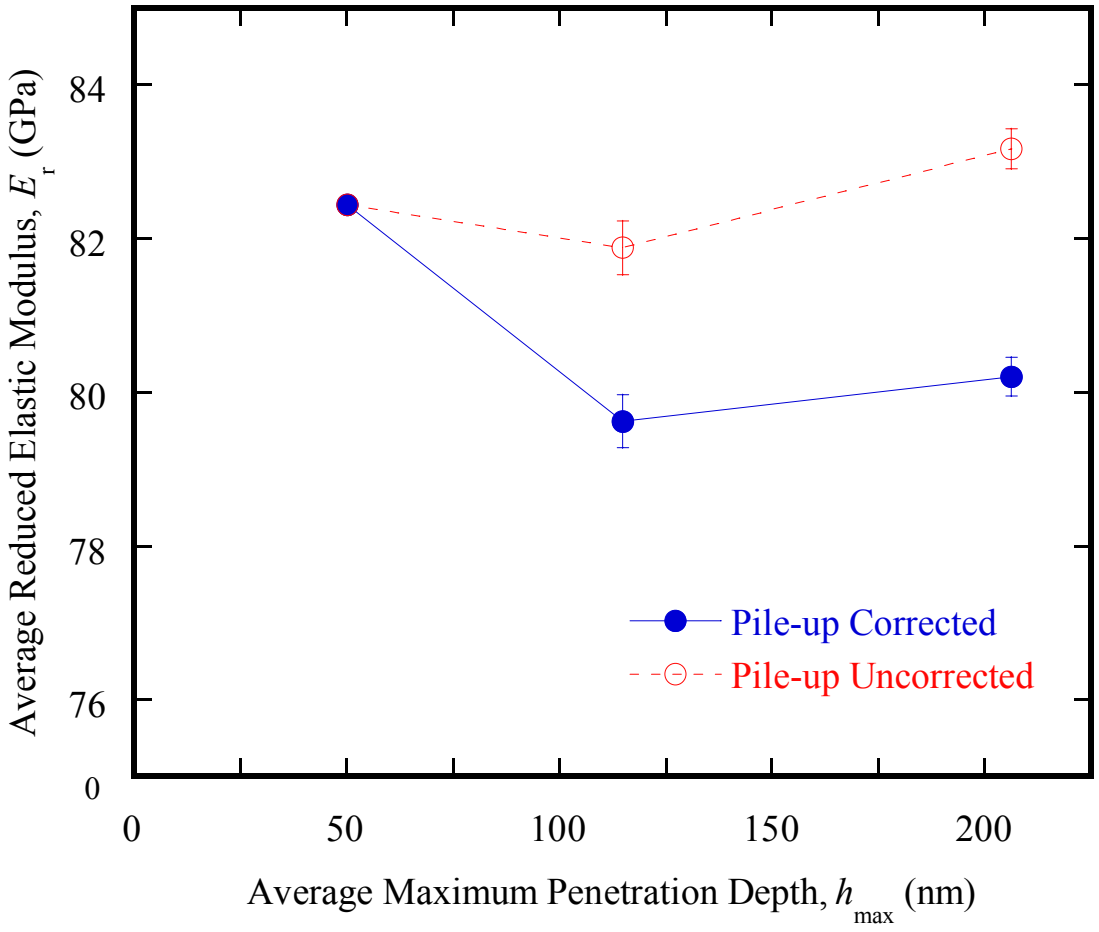

Figure **2.12**: Effect of pile-up correction on the measured reduced elastic modulus of the air side of 2 mm thick Guardian float glass whose pile-up response was depicted in Figure **2.9**. It can be observed that the reduced modulus decreased after pile-up correction.

2.3.3 Surface Roughness

Surface roughness is an important parameter that was capable of adversely affecting nanoindentation testing and data analysis. It was indicated in section **2.3.2** that

the surface roughness introduced a limitation in experimentally evaluating pile-up around an indent. Moreover, previous studies [65-67] had indicated in the past that the large surface roughness values adversely affected the final values of hardness and reduced elastic modulus measured via nanoindentation. Since the objective of the current study was to compare the reduced elastic modulus and hardness across different float glass surfaces, an effort was made to avoid the adverse effects of surface roughness on such comparisons by choosing areas of nominally similar surface roughness across different surfaces. This was achieved with the aid of in-situ AFM imaging. Prior to performing nanoindentation tests on a specimen, in-situ AFM imaging of the surfaces was carried out and a relatively smooth region was chosen to perform the indents. It was also ensured that the indented surfaces across all the regions were of nominally similar surface roughness, as will be shown in the later chapters.

2.4 Representation of Results and Error Analysis

In the ensuing chapters of this manuscript, the results of the nanoindentation testing of commercial float glass will be presented. As mentioned previously, force controlled indentation tests were performed on these samples and 10 indents from each peak force condition were analyzed for material flow behavior (pile-up), reduced elastic modulus and hardness. Therefore, the mean values of these 10 indents at each peak force condition will presented as the results. Furthermore, the objective of this study was to compare afore mentioned mechanical properties across various float glass surfaces and evaluate the presence or absence of differences between these mean values. It was

therefore necessary to evaluate mean value that could represent the mechanical properties of the entire set of indents at that condition as accurately as possible. This confidence in evaluating the mean value was incorporated into the results by displaying error bars whose length on either side of the mean that was equal to the standard error of the mean (SEM). SEM was calculated according to Equation **2-15** where x_i depicts the i^{th} value of the mechanical property whose SEM is being measured and $\bar{x}$ is the mean of that mechanical property for the *n* measurements performed at that condition [68].

$$SEM = \sqrt{\frac{\sum_{i=1}^{n}(x_i - \bar{x})^2}{n(n-1)}} \qquad \text{(Eq. 2-15)}$$

The use of standard error aided in establishing the presence or absence of difference in properties at two different conditions on the basis of their mean values.

2.5 General Methodology of Performing a Nanoindentation Test

Having looked at the various features of the nanoindentation testing and data analysis methodologies until now, this section is intended to present a summary of the final sequential procedure to perform a nanoindentation test on a specimen of choice.

1) A specimen was cut from a larger stock piece of the glass that was available.
2) A local coordinate system was marked using Knoop indents on the surface to be indented.
3) The surface was then cleaned in order to clear any debris and other organic contaminants that might be present on the surface.

4) The sample was then mounted onto a magnetic stainless steel substrate using a cyanoacrylate adhesive to help hold it in position on the nanoindenter stage.
5) Using in-situ AFM imaging, a relatively smooth region was chosen to perform the nanoindentation tests, in order to minimize the adverse influence of surface roughness on the final results. The coordinates of the area chosen to perform the indents were noted using the local coordinate system based on the Knoop indents.
6) The nanoindenter's transducer was calibrated prior to starting the indentation experiment and thermal drift was monitored and corrected for prior to each indent.
7) Initially the tip area calibration was performed once, using data from indents performed on the reference glass. Later, indents on the reference glass prior to running an experiment on the float glass samples and the resulting data was used to evaluate the machine compliance.
8) During data analysis, the machine compliance of the system was evaluated initially.
9) Pile-up around the indents was then quantified using the experimental approach based on post-indent in-situ AFM images.
10) Oliver-Pharr analysis of the nanoindentation force-displacement data was then carried out with the reduced elastic modulus and hardness evaluated being corrected for the pile-up observed around the indents.

Chapter 3

Exposure History Dependence of Float Glass Mechanical Properties

The effects of chemical differences between the two sides of the float glass on its physical properties and corrosion were presented in the introductory chapter of this thesis. In the current chapter the effects of corrosive exposure conditions on the mechanical properties of commercial float glass will be discussed on the basis of the results of our nanoindentation experiments on float glass surfaces that were subjected to controlled exposure conditions. Two kinds of exposure conditions were used in this study – *controlled surface cleaning treatments*, where the exposure time was limited to a few minutes at room temperature and *short-term* corrosive exposure conditions that involved the exposure of the float glass surfaces to corrosive environments at high temperatures for a few days. Initially the details of these exposure conditions will be presented. The reduced elastic modulus and hardness results obtained via nanoindentation are then presented followed by a discussion of their implications.

3.1 Motivation

During the initial nanoindentation testing of aged 2, 6 and 8 mm thick commercial float glass surfaces, it was realized that there existed both smooth and rough regions on the surface of any particular float glass surface. Based on line scans across pre-indent in-situ AFM images it was observed that the smooth regions had a peak-to-valley roughness

of 2 nm while the rough regions had a peak-to-valley roughness of about 6 nm as shown in Figure **3.1**.

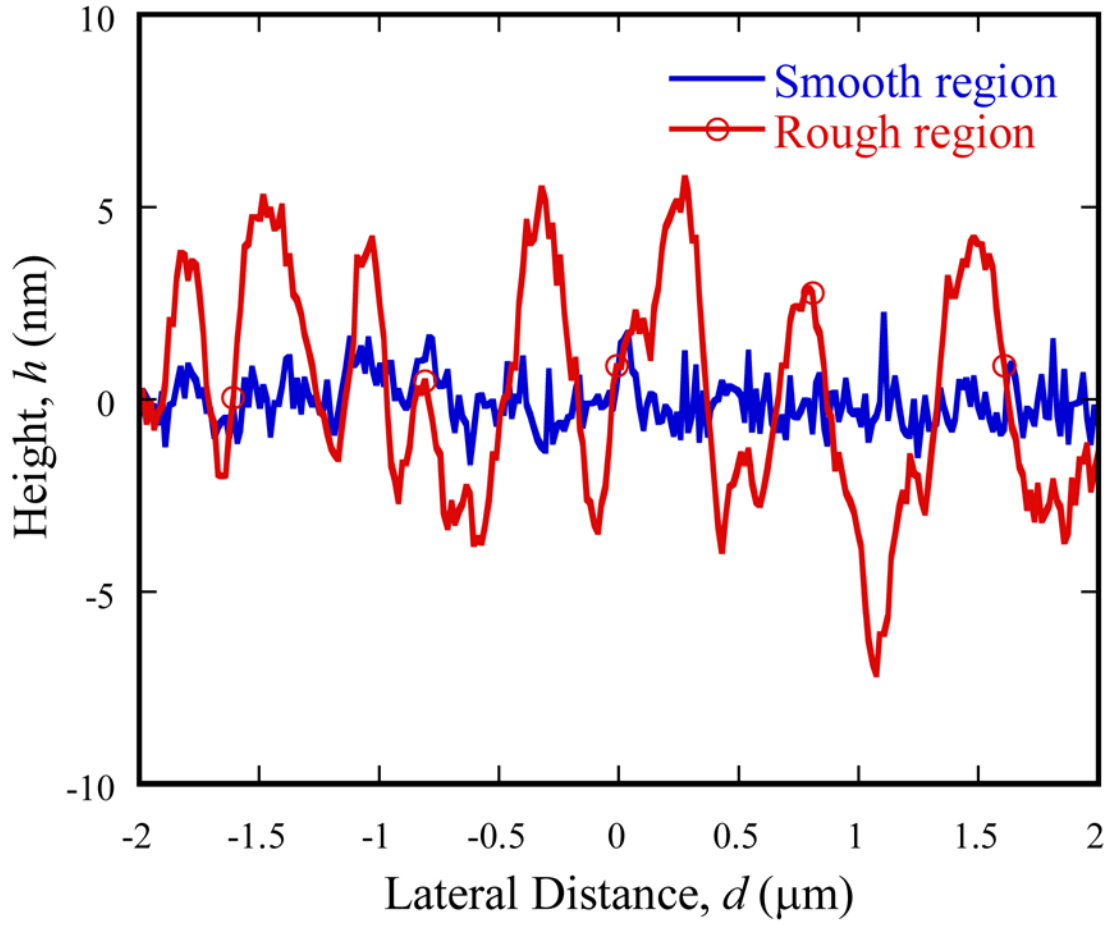

Figure **3.1**: Representative pre-indent in-situ AFM line scans from 4×4 μm^2 regions on a 6 mm thick aged float glass. Clearly, there is a variation in the surface roughness of the two regions and accordingly these regions are labeled as 'smooth' and 'rough' regions. The nominal peak-to-valley roughness for the smooth region is 2 nm while it is around 6 nm for the rough region.

Nanoindentation of smooth and rough regions of any particular float glass surface resulted in significant differences in pile-up, reduced elastic modulus and hardness of these regions. The smooth regions were observed to have ~8% greater reduced elastic modulus, ~30% greater hardness and ~50% lesser pile-up compared to the rough regions.

Figures **3.3** and **3.2** show 3-dimensional images of post-indent images for 6500 μN peak force, force controlled indents performed in the smooth and rough regions that were shown in Figure **3.1**. From these images it was observed that the pile-up in the smooth region ~25 nm while the pile-up in the rough regions was as much as 60 nm, i.e., the rough regions were softer than the smooth regions.

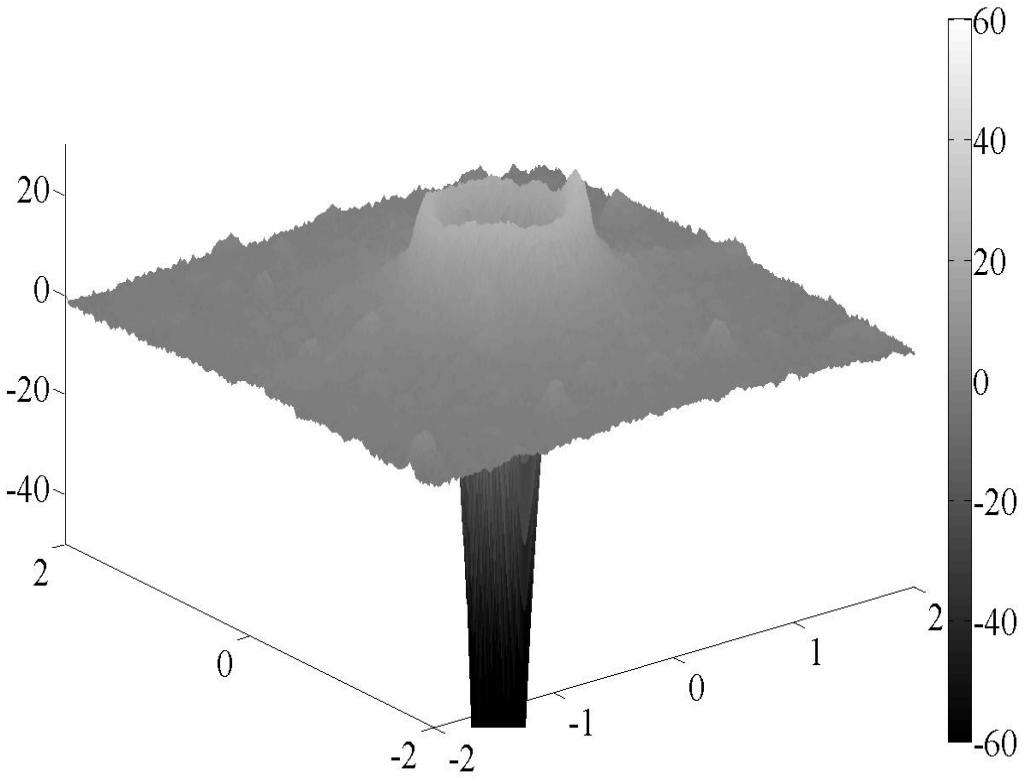

Figure **3.2**: A 3–dimensional post-indent in-situ AFM image of a force controlled indent (peak force of 6500 μN) within the smooth region of the 6 mm thick aged float glass shown in Figure **3.1**. The peak penetration depth for this indent was ~300 nm. Pile-up was observed to be ~25 nm.

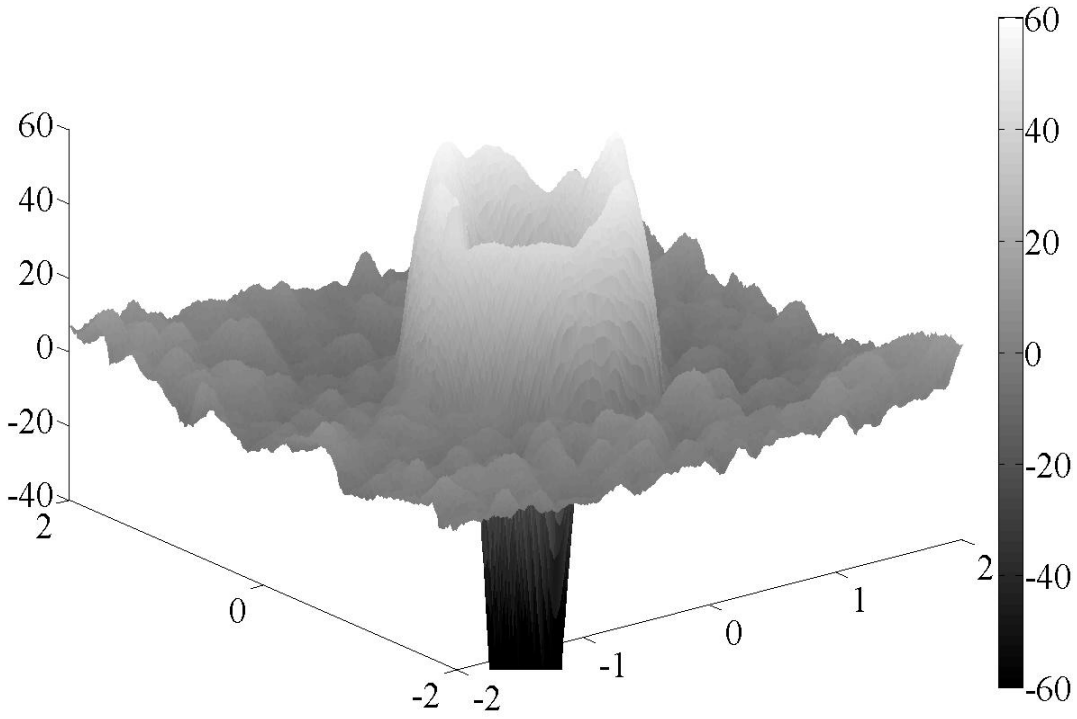

Figure **3.3**: A 3–dimensional post-indent in-situ AFM image of a force controlled indent (peak force of 6500 μN) within the rough region of the 6 mm thick aged float glass that was shown in Figure **3.1**. The peak penetration depth for this indent was ~300 nm. Pile-up was observed to be ~60 nm.

Previous studies had shown that surface roughness could adversely affect the accuracy of the mechanical properties measured via nanoindentation [65-67]. However, the maximum penetration depths for the indents shown in Figure **3.1** were about 300 nm, (i.e., at least 50 times larger than the peak to valley roughness of the rough region), and significant effects of surface roughness on nanoindentation results were not expected at such relatively large penetration depths. Hence it was unlikely that the differences in flow behavior between the soft and hard regions were solely due to surface roughness variations. It had been noted in earlier work on commercial soda-lime-silicate float glass

that corrosion increased their surface roughness [34, 37]. It was also reported that the corrosion modified silicate glass surface layers were analogous to a silica 'gel' layer [69]. Such a gel layer would be expected to be softer than the pristine surface. Since, the observations on these aged float glasses also indicated that the rough regions were softer, it was hypothesized that the intrinsic cause for the lower hardness of the rougher regions was the presence of a corrosion modified surface layer. Therefore, the focus of this study was to evaluate the role of glass corrosion in altering the reduced elastic modulus and hardness of float glass surface layers by performing nanoindentation experiments on float glasses that were subjected to controlled exposure conditions.

3.2 Controlled Exposure Conditions

As mentioned earlier, controlled surface cleaning treatments and short-term corrosive exposure conditions were used to evaluate the influence of exposure history driven surface modifications of float glasses on their mechanical behavior. Fresh float glass that was not subjected to any prior exposure conditions was required for this purpose. Fresh commercial float glass samples, 2 mm in thickness, manufactured by Guardian Industries Inc. were obtained directly off the float line but without any interleave acid coatings [37]. The stacking separation between the samples was maintained using poly (methyl methacrylate) (PMMA) spacer beads (150 mg/m^2) to replicate the storage conditions for commercial float glass. The samples were stored for one year in a vacuum desiccator until the nanoindentation experiments were performed. Samples for nanoindentation experiments were cut from a single stock glass piece 3.5 cm

wide and 8.5 cm long. Each individual specimen was about 2 cm in length and width. All the specimens were mounted on a stainless steel substrate in order to perform nanoindentation and hence only one surface (either the air or the tin side) of the float glass could be evaluated on a given sample. Separate samples cut from adjacent locations were thus used to test the air and tin sides for each particular exposure condition. Samples were cut from the stock piece by fracturing along a scribe mark that was created with a diamond scribe. All the scribe marks were initiated on the air side of the float glass. Cyanoacrylate adhesive was used to affix the samples onto stainless steel substrates. All the samples had to be cleaned prior to mounting them on stainless steel substrates to remove debris, reaction products and organic contaminants that might exist on their surfaces. As mentioned above, the effects of these surface cleaning treatments on float glass mechanical behavior constituted an important part of the current study. Therefore, the specific details of these controlled surface cleaning treatments will be presented in section **3.2.1** followed by the details of the short-term corrosive exposure conditions in section **3.2.2**.

3.2.1 Surface Cleaning Treatments

Three different surface treatments were used to evaluate the influence of very short duration surface cleaning procedures on the mechanical behavior of the air and tin sides of float glass. The three surface cleaning treatments differed from each other in the first step where the float glass surfaces were exposed to an acidic solution (pH 0.9 Hydrochloric acid solution), neutral solution (pH 7.1 reverse osmosis (RO) water) or

alkaline solution (pH 9.5 Alconox® solution) for 30 seconds. During this exposure period, the surfaces were scrubbed gently with a cotton swab to help remove loosely adhering surface contaminants. After this initial exposure, each sample was immersed in RO water and placed in an ultrasonic bath for five minutes to remove contaminants still adhering to the surface. Upon removal from the ultrasonic bath, each sample was rinsed for 10 seconds in the isopropyl alcohol to remove any organic contaminants remaining on the surface. The samples were then blown dry with pre-purified nitrogen gas and mounted on the steel substrates for nanoindentation tests. As mentioned earlier, silicate glasses are commonly used as calibration standards for nanoindentation systems and are subjected to some kind of surface cleaning treatment prior to testing. Consequently, the results of this study are important in understanding the effects of surface cleaning protocols on nanoindenter calibration and accuracy.

3.2.2 Short-term Corrosion

Evaluating the influence of the short-term corrosive exposure history of these silicate glasses on their mechanical properties is also important because short-term exposure can also lead to the presence of a modified surface layer possessing mechanical properties different from the pristine surfaces. The controlled short-term exposure conditions included float glass samples that were weathered or leached for a period of 3 – 4 days. Static weathered samples were prepared by stacking together many float glass plates separated by PMMA beads. The stacks were then placed in a programmable humidity chamber (Lunaire Environmental, Model CEO-910-W-4, Williamsport, PA) for

4 days at 85% relative humidity and 85ºC [37]. Static weathered float glass specimens for nanoindentation testing were obtained from one such 15.2 cm × 15.2 cm piece that was a part of the stack of weathered glasses. The other form of glass corrosion via exposure to a corrosive liquid (referred to as leaching) involved exposing the samples (cut out from the earlier mentioned 3.5 cm × 8.5 cm stock piece) to de-ionized (DI) water at 90ºC for 3 days. The samples (surface area of ~8 cm^2) were placed in Teflon net baskets which were immersed vertically in 250 ml of DI water maintained in Teflon containers. The containers were cleaned prior to sample preparation in accordance with the ASTM 1285–02 standard [70]. Both the static weathered samples and the liquid leached samples were subjected to the neutral cleaning treatment (described earlier) at the end of the corrosion. This additional surface cleaning treatment was performed in order to render the surfaces suitable for nanoindentation testing as discussed earlier. Therefore, in the context of understanding the effect of the weathering and leaching on the float glass mechanical properties, the samples subjected to the neutral surface cleaning treatment and no other form of exposure were used as the reference 'fresh' samples that were not corroded. All the specimens were subsequently mounted on the steel substrates to facilitate their nanoindentation testing.

3.3 Effects of Exposure Conditions on Nanoindentation Results

In this section the results of the nanoindentation studies on the float glasses subjected to controlled surface cleaning treatments and short-term exposure conditions will be presented. Furthermore the salient features of these results and their implications

will be discussed. The nanoindentation testing and data analysis methodology presented in Chapter 2 was applied uniformly for all the surfaces. In the light of the fact that the surface cleaning treatments and the short-term exposure conditions differ from each other in terms of the exposure media that were used and the parameters that were controlled, their results and implications will be discussed separately.

As discussed earlier in this chapter, surface roughness variations of these samples were known to adversely affect the accuracy of the final reduced elastic modulus and hardness results. To avoid this problem, and compare the nanoindentation results across the different surfaces, regions of nominally similar, low peak-to-valley roughness were chosen on all the surfaces with the aid of in-situ AFM imaging. Figure **3.4** displays representative line scans of the low roughness regions in the largest pre-indent in-situ AFM images of surfaces that were subjected to the three different surface cleaning treatments. Similarly Figure **3.5** depicts the representative line scans from the largest pre-indent in-situ AFM images for the surfaces that were subjected to the short-term corrosive exposure conditions. This figure also indicated that the indented regions across different samples had similar nominal peak-to-valley surface roughness, so any observed differences in the properties between these surfaces were due to the variations in exposure conditions and not due to variations in surface roughness.

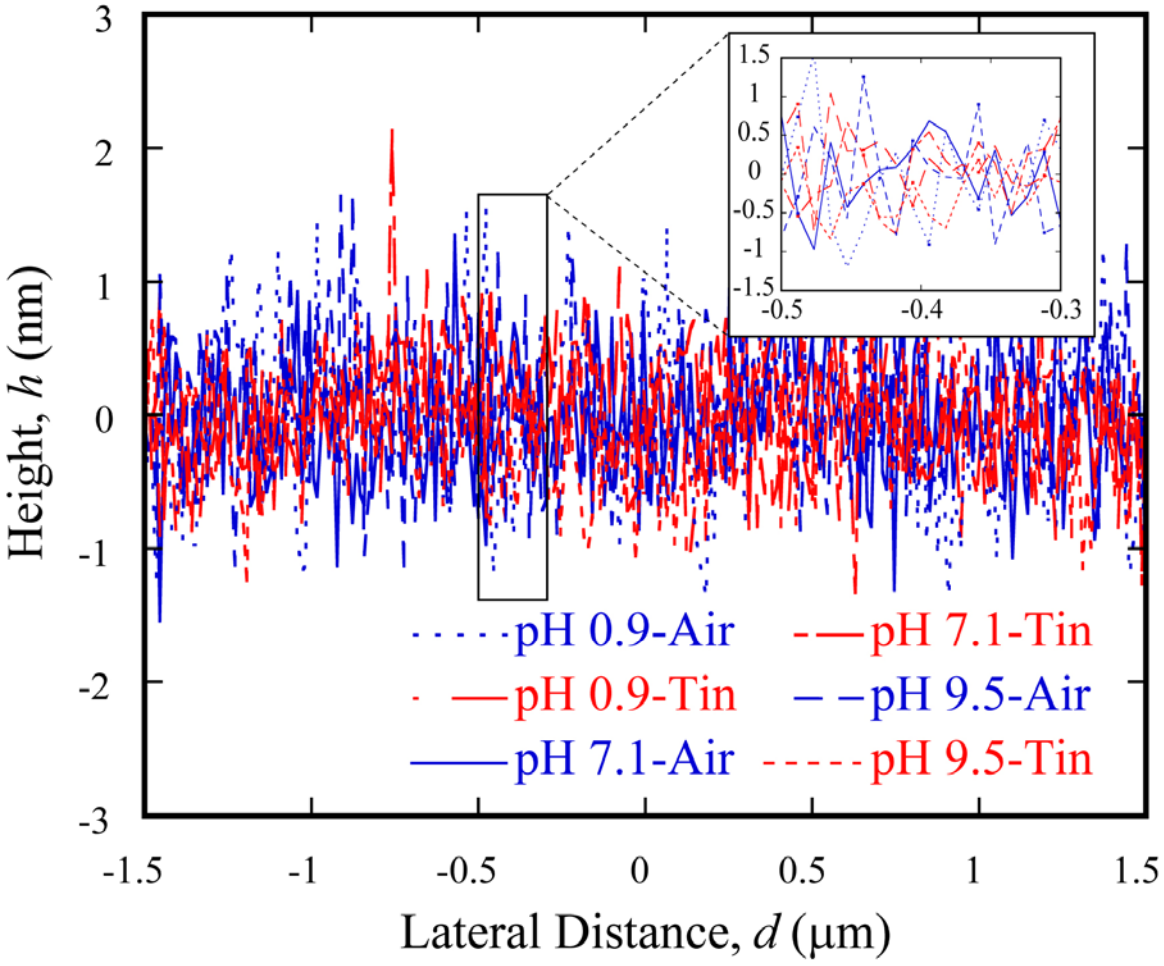

Figure **3.4**: Representative line scans obtained from pre-indent in-situ AFM images of float glass surfaces subjected to acidic (pH 0.9), neutral (pH 7.1) and alkaline (pH 9.5) surface cleaning treatments. Inset shows a magnified view from a reduced length scale. It is observed that all the surfaces have the same nominal surface roughness and therefore the observed mechanical property variations across these surfaces are due to the cleaning treatments, not variations in surface roughness.

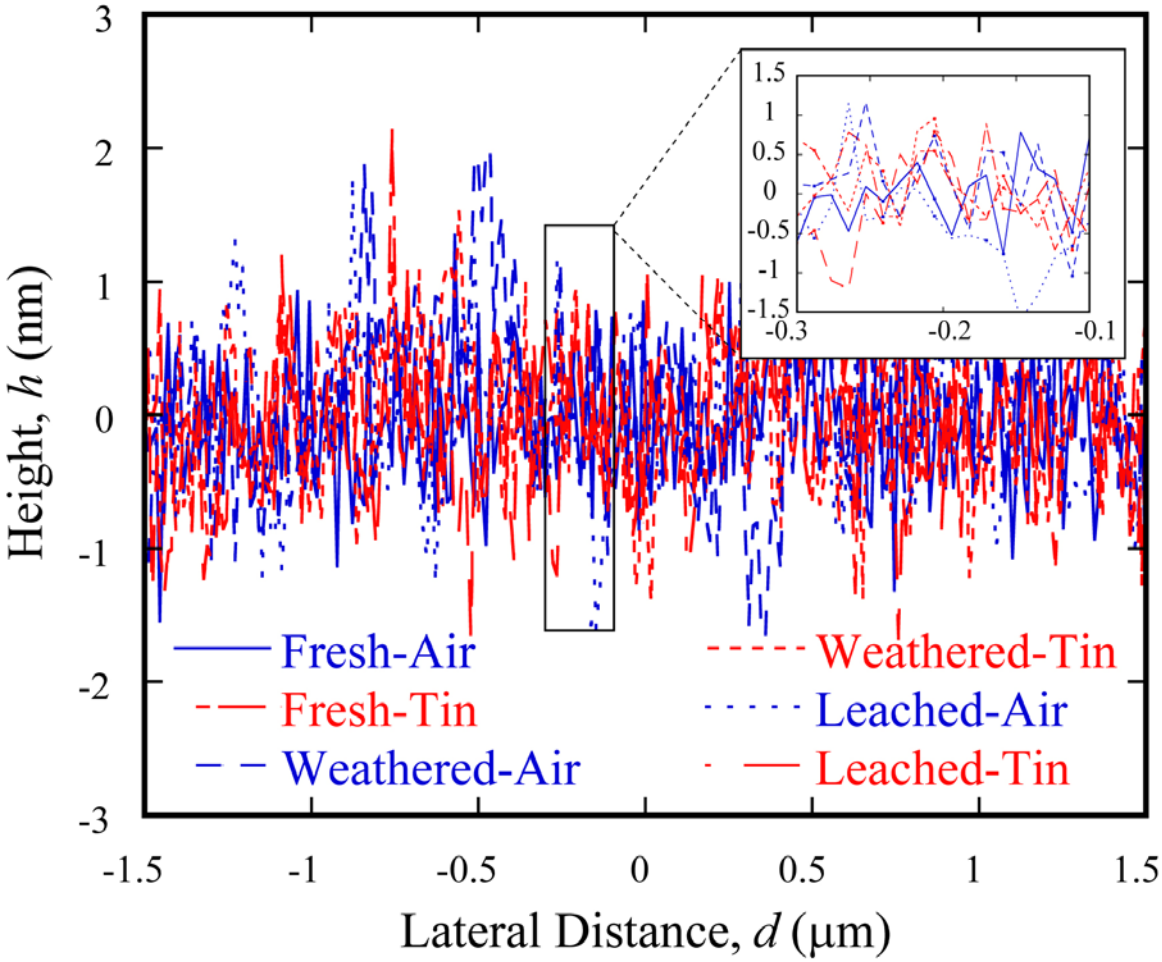

Figure **3.5**: Representative line scans obtained from pre-indent in-situ AFM images of fresh, weathered and leached float glass surfaces. Inset shows a magnified view from a reduced length scale. It is observed that all the surfaces have the same nominal surface roughness. Therefore, the observed mechanical property differences are due to the short-term corrosive exposure conditions and related structural changes, not due to surface roughness variations.

3.3.1 Influence of Surface Cleaning Treatments

Figure **3.6** displays the experimentally evaluated average pile-up for the float glass surfaces subjected to acidic (pH 0.9), neutral (pH 7.1) and alkaline (pH 9.5) cleaning treatments at the 4 peak load indentation conditions used in this study.

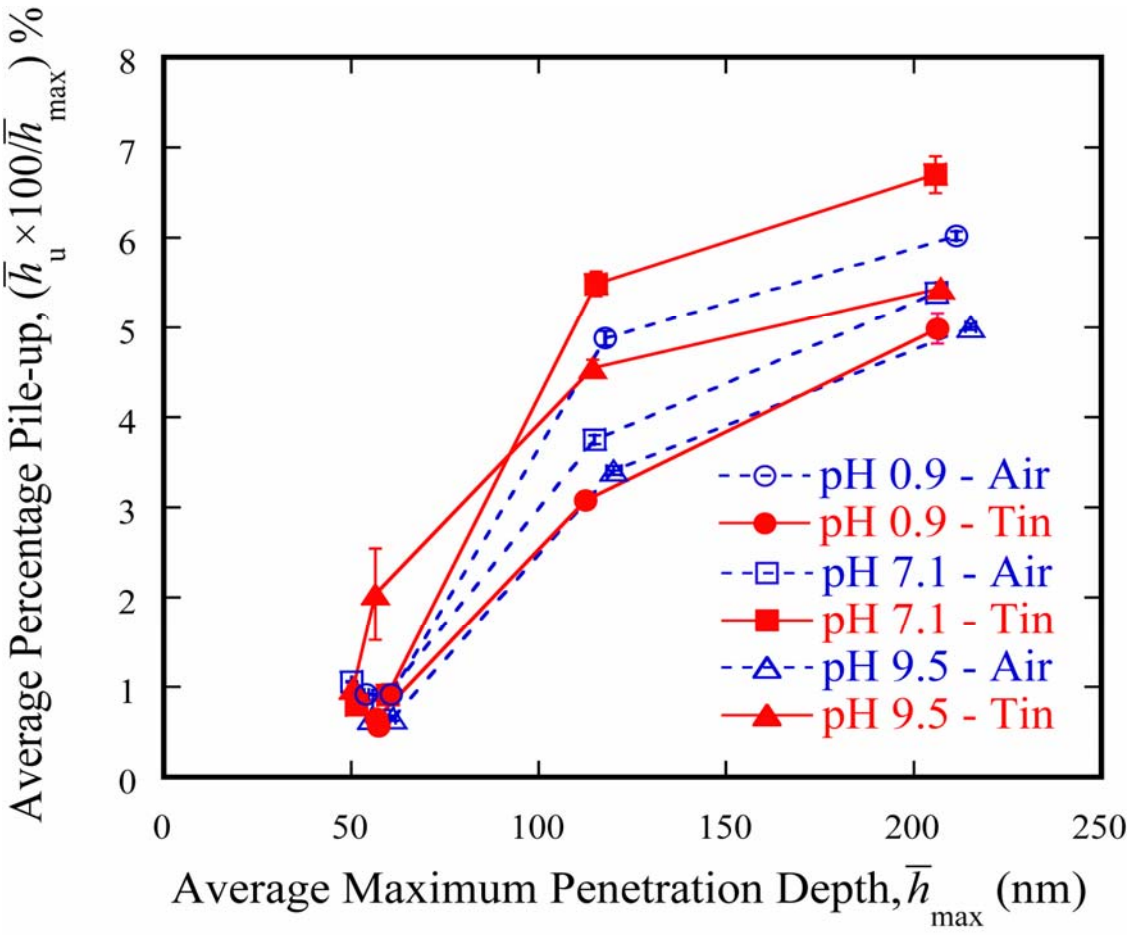

Figure **3.6**: Experimentally evaluated average percentage pile-up as a function of the average maximum penetration depth for the surfaces subjected to acidic (pH 0.9), neutral (ph 7.1) and alkaline (pH 9.5) surface cleaning treatments. Data plotted are the averages of 10 force controlled indents per condition, for four peak force conditions of 750, 900, 2000 and 4000 μN. The length of the error bars on either side of the mean values was equal to the standard error of the mean. Pile-up was observed to increase with penetration depth and it varied for the different surfaces.

Pile-up at the very shallow penetration depths (50 – 60 nm) was indistinguishable from the surface roughness on the basis of Equation **2-12**. As discussed in Chapter 2, for these indentation conditions the upper bound of pile-up was evaluated using the pre-indent images and this conservative estimate was shown in Figure **3.6**. Also the reduced elastic modulus and hardness results for these conditions were corrected for this upper bound estimate of pile-up. Pile-up results, expressed as a percentage of the corresponding maximum penetration depth, are presented as a function of the maximum penetration depth in Figure **3.6**. It was observed that pile-up increased with increasing penetration depth and all the surfaces exhibited pile-up in the range of ~0.5 – 7%.

Figures **3.7** and **3.8** depict the reduced elastic modulus (E_r) and the hardness (H) as a function of the maximum penetration depth for the surfaces that were subjected to the different surface cleaning treatments. These reduced elastic modulus and hardness results were corrected for the experimentally evaluated pile-up around the indents shown in Figure **3.6**. The plots show the average E_r and H calculated from 10 indents at each condition. The length of the error bars equals the standard error of the mean on either side of the mean values. The reduced elastic moduli of the different surfaces lay between 85 and 75 GPa. A part of this numerical range of reduced elastic modulus values are higher than the typically reported reduced elastic moduli for fresh, bulk soda-lime-silica float glasses which are about 76 – 78 GPa (assuming a constant Poisson's ratio of 0.23 and elastic modulus of 72 – 74 GPa). However, these values are within the range of the reduced elastic moduli reported from previous nanoindentation [26, 52, 71]. However, the reasons for the higher values of reduced elastic modulus evaluated via nanoindentation compared to the bulk values are not clear at this point.

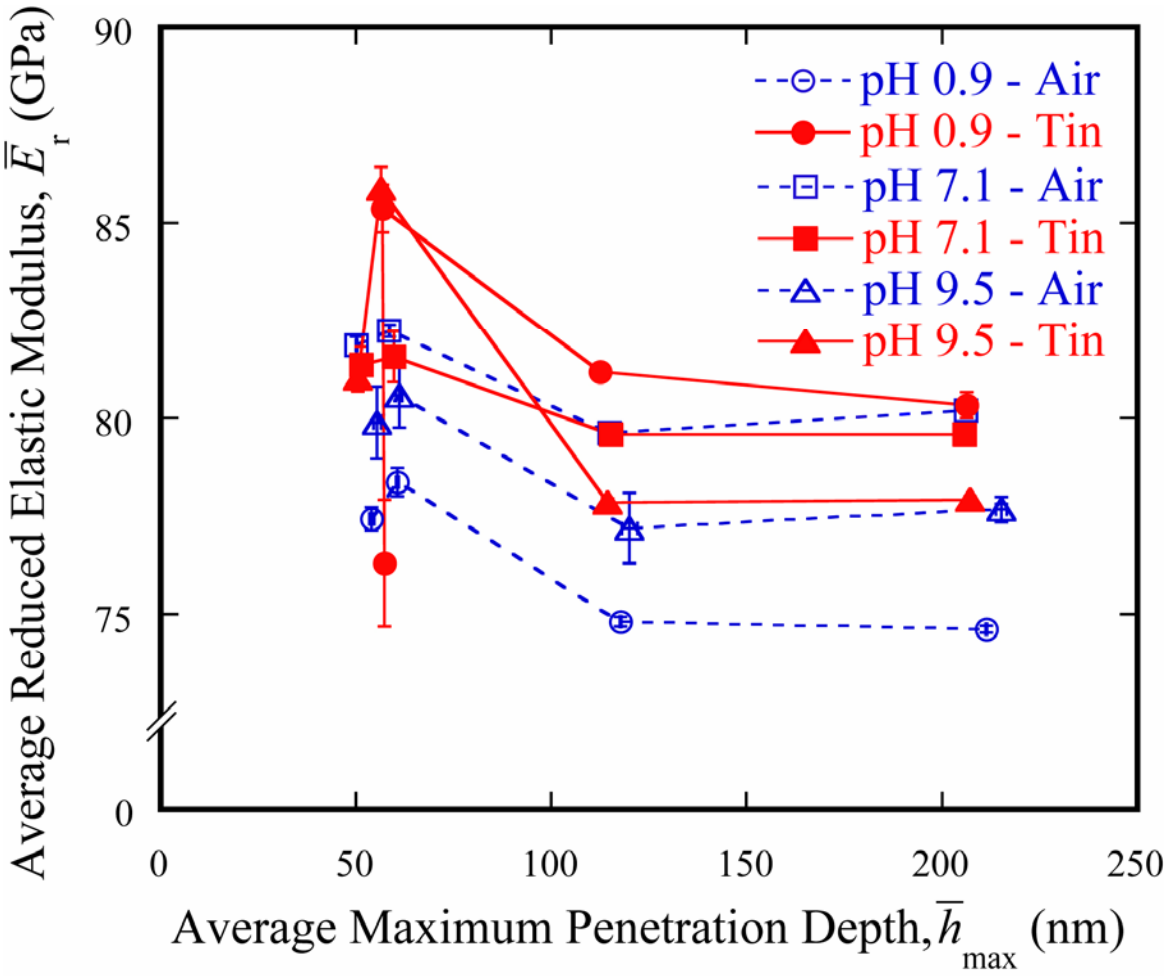

Figure **3.7**: Average reduced elastic modulus (E_r) as a function of the average maximum penetration depth for the surfaces subjected to acidic (pH 0.9), neutral (pH 7.1) and alkaline (pH 9.5) surface cleaning treatments. Data plotted represent the mean of 10 force controlled indents per condition, for four peak force conditions of 750, 900, 2000 and 4000 μN. The length of the error bars on either side of the mean values was equal to the standard error of the mean. Reduced elastic modulus was observed to decrease with penetration depth up to ~100 nm and then reach a near constant value. Also the reduced modulus was dependent on the nature of the surface cleaning treatments that the surfaces were subjected to.

For all the surfaces shown in Figure **3.7** it was observed that the reduced elastic modulus decreased by about 2 – 4 GPa with increasing penetration depths from 50 to 100 nm. Beyond 100 nm the reduced elastic modulus remained nearly constant up to ~225 nm which was the maximum penetration depth probed in this study. Hardness for the

different surfaces generally lay between 7.25 – 8.25 GPa. Hardness was found to increase by ~0.75 GPa with as the maximum penetration depth increased from 50 – 225 nm.

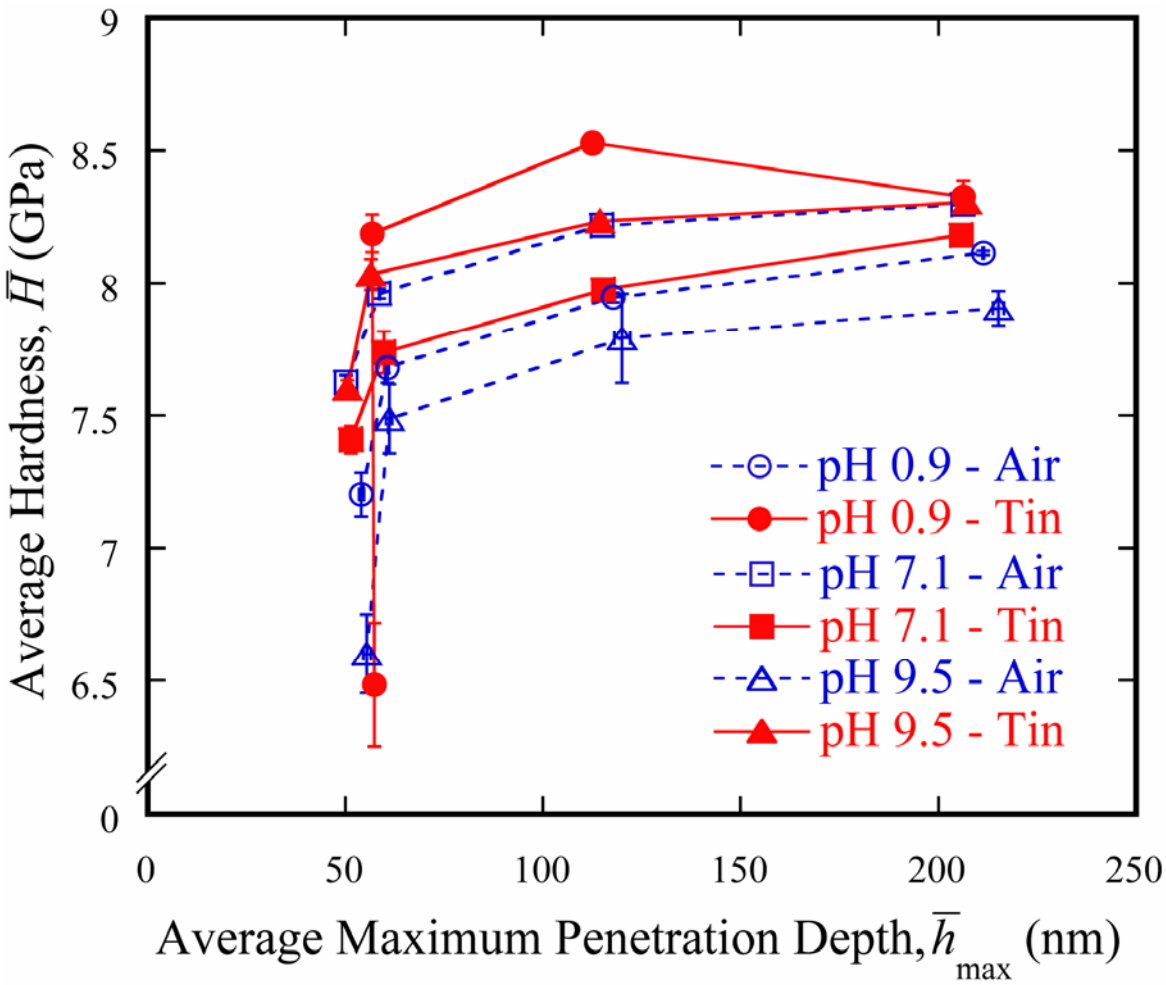

Figure **3.8**: Average hardness (*H*) as a function of the average maximum penetration depth for the surfaces subjected to acidic (pH 0.9), neutral (pH 7.1) and alkaline (pH 9.5) surface cleaning treatments. Data plotted represent the mean of 10 force controlled indents per condition, for four peak force conditions of 750, 900, 2000 and 4000 μN. The length of the error bars on either side of the mean values was equal to the standard error of the mean. Hardness was found to increase with increasing penetration depth. Acidic and alkaline cleaning treatments lead to the decrease in the hardness for the air side of the float glass while it they lead to an increase in the hardness on the tin side of the float glass.

Furthermore, comparison of the different air or tin sides subjected to the three different surface cleaning treatments indicated that these exposure conditions altered the reduced elastic modulus and hardness of the surfaces.

Upon comparing the reduced modulus of the air sides subjected to the three different surface cleaning treatments (Figure **3.7**) it was observed that the neutral cleaning treatment showed the highest reduced elastic modulus of 82 – 80 GPa, while ~3% (~2.5 GPa) lower reduced elastic modulus was exhibited by the alkaline cleaning treatment with the acidic treatment resulting in an even lower reduced elastic modulus (6 – 7.5% lower) relative to the neutral cleaning treatment. The higher reduced elastic modulus of the air side subjected to the neutral cleaning treatment compared to those subjected to acid cleaned and alkali cleaned air sides was probably due to the corrosion of the air side when subjected to acidic and alkaline cleaning treatments. It was known that corrosion mechanisms in alkali silicate glasses, such as the soda-lime-silica float glasses used in this study, were dependent on the availability of the hydronium ions (H_3O^+)/ proton (H^+) or hydroxyl ions (OH^-) as given by Equations **3-1** and **3-2** [28, 72-74]. While the mechanism in Equation **3-1** is dominant at pH < 9, the mechanism mentioned in Equation **3-2** dominates at pH > 9.

$$\equiv Si - OR + H_3O^+ / H^+ \longrightarrow \equiv Si - OH + R^+ + H_2O \qquad \text{(Eq. 3-1)}$$

$$\equiv Si - O - Si(OH)_3 + OH^- \longrightarrow \equiv Si - O^- + Si - (OH)_4 \qquad \text{(Eq. 3-2)}$$

The neutral cleaning treatment had a very low concentration of H_3O^+/H^+ or OH^- in the solution which probably rendered it the least corrosive of the three treatments. Corrosion

of alkali silicate glasses had been shown to create a modified surface layer that was hydrated and analogous to a silica gel layer [69]. Such a corrosion modified layer was thus expected to have a lower elastic modulus and hardness relative to the pristine surface. This would therefore explain the lower reduced elastic moduli and hardnesses of the air side surfaces subjected to acidic and alkaline cleaning treatments. The tin side of commercial float glass was reported to be more resistant to corrosion than the air side [30-34] and hence it was not expected to observe significant effects of the different, very short duration surface cleaning treatments on the reduced elastic modulus of this surface. However, it was evident from Figure **3.7** that the reduced modulus of the tin side was also affected by the nature of the cleaning treatment that was used. Even though there were differences in moduli between the three tin side surfaces subjected to the three cleaning treatments, at depths lower than 100 nm a clear trend in these variations was not discernible. At deeper penetration depths, however, it was observed that relative to the neutral cleaning treatment, the acidic cleaning treatment demonstrated a ~2% increase in modulus and the alkaline cleaning treatment displayed ~2% reduction in modulus. Thus there was a ~5 GPa difference between the reduced moduli of the tin sides subjected to acidic and alkaline cleaning treatments indicating that the very short duration surface cleaning treatments were also capable of altering the reduced modulus of a corrosion resistant tin side. The higher reduced elastic modulus of the tin side subjected to acidic cleaning treatment relative to the tin side subjected to neutral cleaning treatment, cannot be attributed to a corrosion modified surface gel layer as in the case of the air side, because the neutral cleaning treatment is less corrosive than the acidic cleaning treatment.

This also indicated that the two surfaces of the float glass reacted differently to a given exposure conditions.

The fact that these surface cleaning treatments altered the reduced elastic modulus of not only the air side, but also the more corrosion resistant tin side, has serious implications related to nanoindentation testing. Silicate glasses are commonly assumed to be homogenous, isotropic and exhibit time- and depth- independent elastic moduli making them a popular choice as reference materials to calibrate nanoindentation systems. Often, the effects of cleaning treatments on the reduced modulus of these glasses are not evaluated and the properties of these glasses are assumed to be the same as known reference values. However, when the moduli of the surfaces of these glasses are affected by short-term cleaning treatments, it is obvious that the fundamental basis of choosing a reference standard for nanoindentation calibration procedures will not be satisfied. On a positive note, our reduced elastic modulus results on float glass surfaces indicated that nanoindentation testing was highly sensitive and capable of discerning small variations in the reduced elastic modulus.

Hardness of the float glass surfaces was also evaluated from nanoindentation test data as described earlier in Chapter 1. It was evident from Figure **3.8** that the hardness of the float glass surfaces that were subjected to the three different surface cleaning treatments underwent changes. Hardness comparisons across the three different air sides pointed out that the air side subjected to the neutral cleaning treatment displayed the highest hardness. The alkaline cleaning treatment resulted in a hardness that was 5 – 13% (i.e., 0.5 – 1 GPa) lower than the neutral cleaning treatment depending on the penetration depth. The acid cleaned, air side had an intermediate hardness that was lower than that of

the neutral cleaned surface by 2 – 6% depending on the penetration depth. Similar to the reduced elastic modulus results, the hardness of the corrosion resistant tin side also displayed changes due to short-term exposure. The hardness of the tin sides subjected to alkaline and acidic cleaning treatments, unlike the corresponding air sides, displayed a small 2 – 5% increase relative to the tin side subjected to the neutral cleaning treatment. This indicated that the differences in chemistry and structure of the two sides of the float glass influenced its interaction with exposure environment.

3.3.2 Influence of Short-term Corrosion

The objective of the short-term controlled exposure studies was to understand the effect of float glass corrosion (weathering and leaching) and related structural modifications on the surface mechanical properties. These samples, however, underwent the neutral cleaning treatment mentioned earlier, after the initial short-tem corrosive exposure and prior to nanoindentation testing. Therefore, to understand the effects of only controlled short-term float glass exposure on its mechanical behavior, the results from the weathered and leached samples were compared to the float glass sample that had only experienced the neutral surface cleaning procedure. The samples subjected to the neutral cleaning treatment (pH 7.1) shown in Figure **3.6** – **3.8** were considered to be the initial state, 'Fresh' glass, and the reference state for establishing the effects of short-term float glass exposure on the mechanical properties of their surfaces. The static weathered glass surfaces were labeled 'Weathered' while the liquid leached glass surfaces were labeled 'Leached' (Figures **3.9** – **3.11)**. Figure **3.9** represents the percentage pile-up observed in

fresh and corroded glass specimens as a function of the maximum penetration depth. Pile-up was found to increase with increasing penetration depth, typically reaching about 5 – 6% at maximum penetration depths of ~200 nm. The air side of the weathered glass exhibited relatively higher pile-up compared to the other surfaces beyond 200 nm.

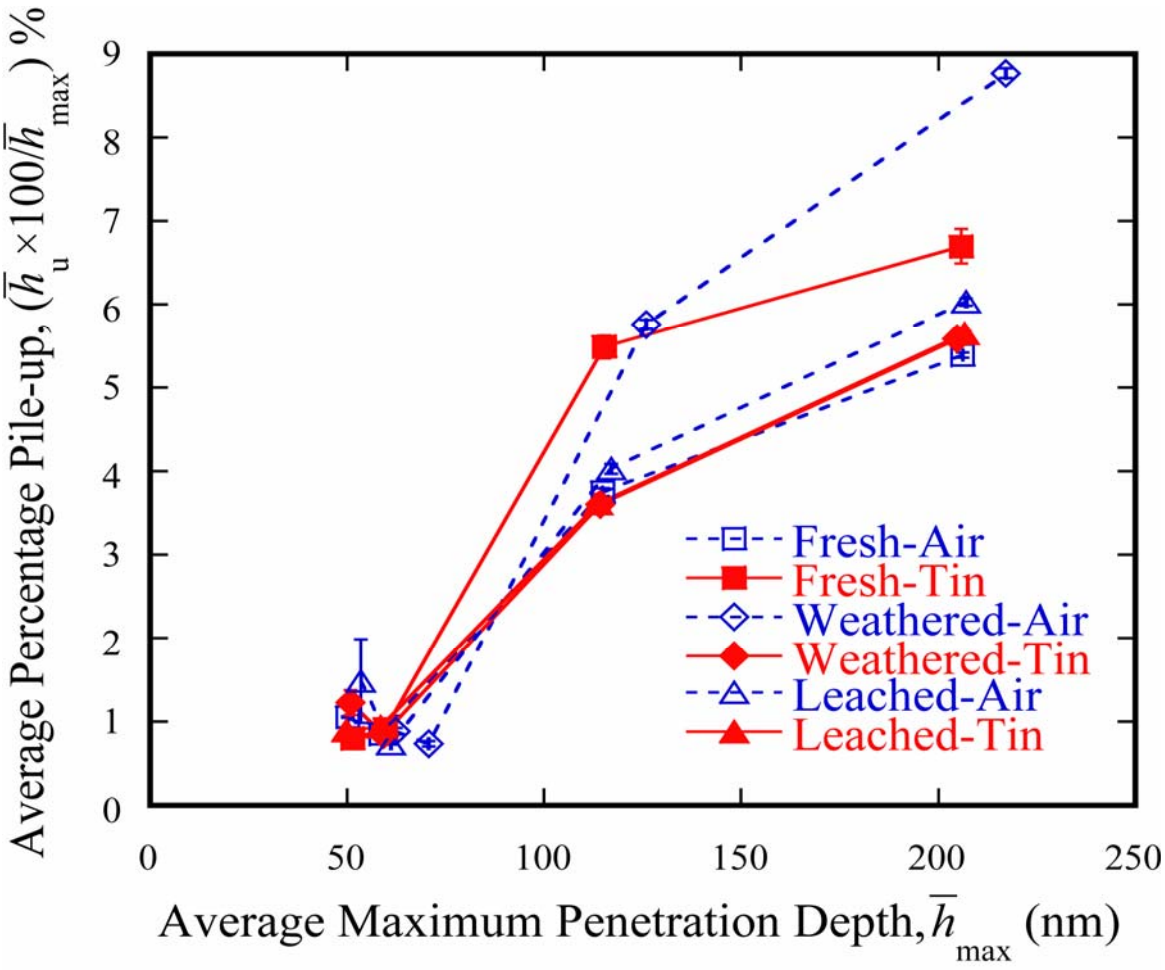

Figure **3.9**: Experimentally evaluated average percentage pile-up as a function of the average maximum penetration depth for the fresh, weathered and leached float glass surfaces. Data plotted are the averages of 10 force controlled indents per condition, for four peak force conditions of 750, 900, 2000 and 4000 μN. The length of the error bars on either side of the mean values was equal to the standard error of the mean. Pile-up was observed to increase with penetration depth and it varied for the different surfaces.

Figures **3.10** and **3.11** present reduced modulus and the hardness of these surfaces, respectively, as a function of the peak penetration depth.

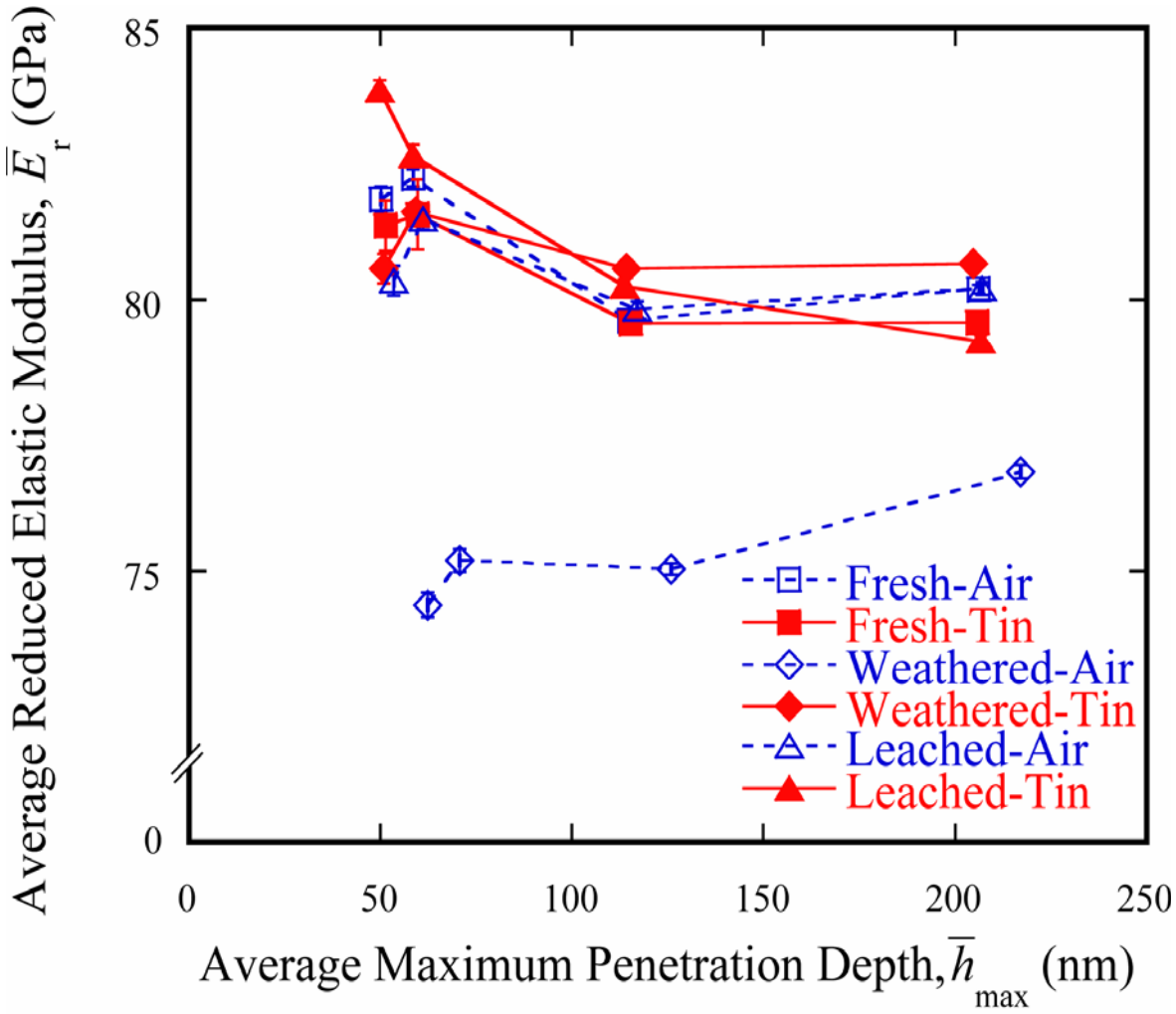

Figure **3.10**: Average reduced elastic modulus (E_r) as a function of the average maximum penetration depth for the fresh, weathered and leached float glass surfaces. Data plotted represent the mean of 10 force controlled indents per condition, for four peak force conditions of 750, 900, 2000 and 4000 μN. The length of the error bars on either side of the mean values was equal to the standard error of the mean. Reduced elastic modulus of the air side was found to vary with penetration depth and the different short-term corrosive exposure conditions.

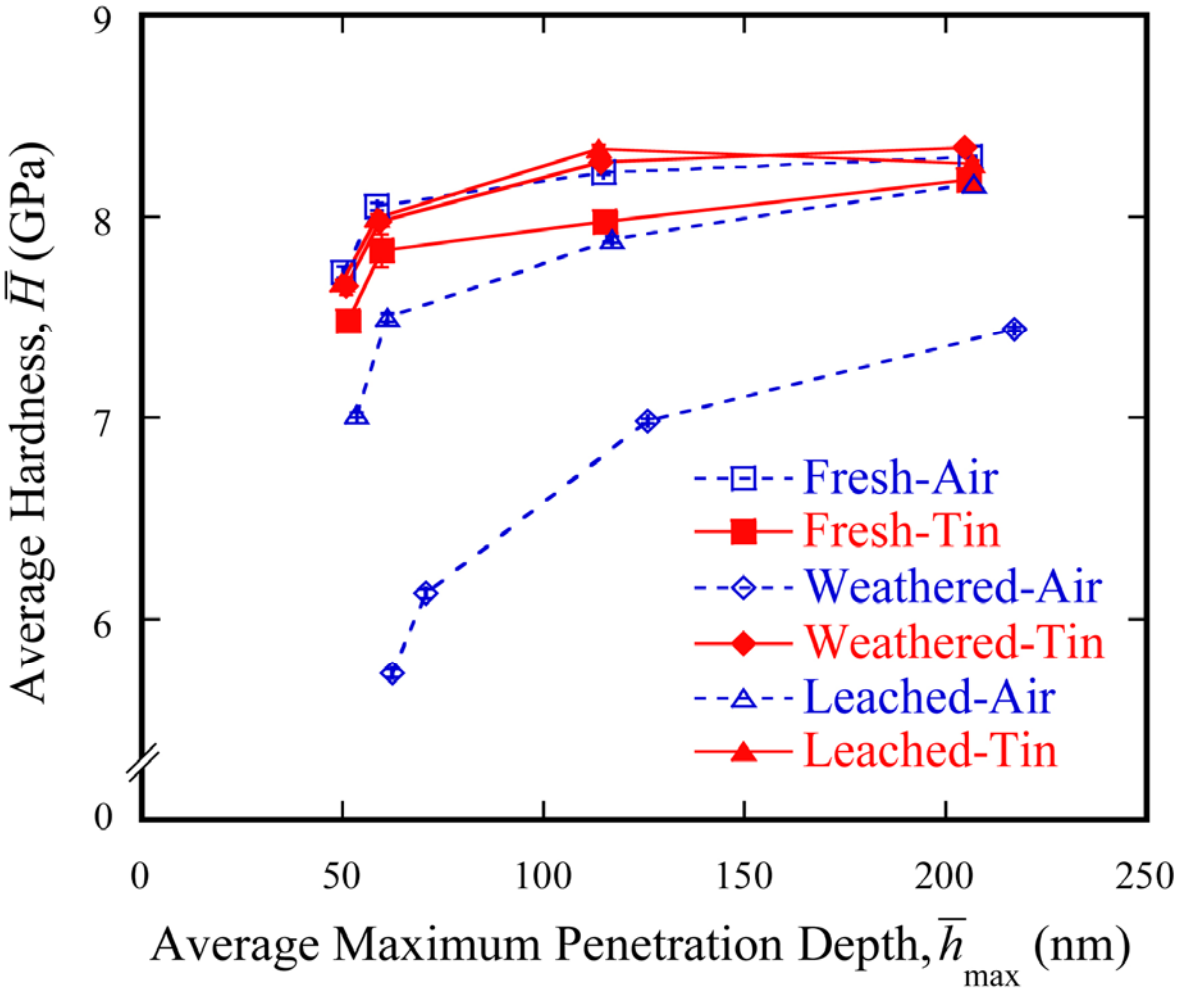

Figure **3.11**: Average hardness (H) as a function of the average maximum penetration depth for the fresh, weathered and leached float glass surfaces. Data plotted represent the mean of 10 force controlled indents per condition, for four peak force conditions of 750, 900, 2000 and 4000 μN. The length of the error bars on either side of the mean values was equal to the standard error of the mean. It is observed that the hardness is increases with increasing penetration depth. Hardness of the air side was found to decrease due to short-term corrosive exposure while there was a slight increase due to corrosion on the tin side.

Except for the air side of weathered float glass, all the other samples had reduced elastic moduli in the range of 80 – 82.5 GPa. The air side of the weathered samples had elastic moduli values between 75 and 77.5 GPa. All the surfaces except the air side of

weathered glass exhibited ~3% elevation in reduced modulus at the very shallow penetration depth. The hardness lay between 7 and 8.25 GPa with the exception of the weathered air side that had hardness in the range of 5.5 – 7.5 GPa over the range of indentation depths that were tested. Hardness, unlike reduced elastic modulus, decreased at shallow penetration depths for all the surfaces.

It was noted from Figure **3.10** that the air side of the weathered float glass demonstrated a 4 – 9% (i.e., 5 – 7.5 GPa) reduction in reduced elastic modulus over an indentation depth range of about 50 – 225 nm. The air side of the leached glass, however, did not show any significant deviation in reduced elastic modulus from that of fresh float glass. A similar comparison of the hardness for the three different air side surfaces from Figure **3.11** pointed out that at shallow penetration depths weathering led to a ~25% (~2 GPa) reduction in hardness and leaching lead to a 10% (~0.75 GPa) drop in hardness relative to the fresh glass. These observations indicated that short-term corrosion (i.e., both weathering and leaching) led to a reduction in the modulus and hardness of the air side of float glass. The differences in hardness between the corroded surfaces and the fresh glass diminished with increasing penetration depth, and at a penetration depth of about 200 nm, the reduction in hardness of the weathered glass was only 10% while the leached glass had hardness similar to that of fresh glass. The diminishing differences in reduced modulus and hardness between the corroded and fresh float glass with increasing indentation penetration depth suggested that the effects of corrosion wore out at deeper penetration depths. Apart from the fact that the weathered sample exhibited a lower modulus than the fresh and leached float glass surfaces, there was also no significant difference in hardness and reduced elastic modulus between the fresh and leached

surfaces at penetration depths of 225 nm. In contrast, the weathered air side was found to have significantly lower moduli and hardnesses at this depth. These observations suggested that the thickness of the corrosion modified surface layers on the leached glass was lower compared to that on the weathered sample. The air side of the weathered glass that was indented as a part of this study was known to have a corrosion modified surface layer at least 50 nm thick based on an earlier study [37]. This previous study had evaluated the leached layer depths on the air side of float glasses subjected to varying corrosion conditions using X-ray photoelectron spectroscopy and it established the presence of a 50 nm Na depletion layer for the air side of the very same weathered float glass whose mechanical properties are reported in the current article, relative to the very same fresh air side used as a baseline for evaluating the effect of corrosion on mechanical properties. As discussed earlier, Na depletion from the surface of the glass during corrosion led to the formation of a hydrated, silica enriched gel layer that was expected to have lower moduli and hardnesses relative to the pristine glass. The presence of this 50 nm leached layer could explain the reason for lower reduced modulus and hardness at the shallow penetrations depths of about 60 and 70 nm. However, the observed mechanical property differences between fresh and weathered air sides extended much beyond 50 nm. The reason for the differences observed even at 200 nm was most probably due to an indentation history effect where the modified 50 nm surface layers are being deformed even during a 200 nm indent and thereby contributing to the evaluated mechanical properties. This would also explain the diminishing differences in moduli and hardness at penetration depths greater than the thickness of the leached layer because the contribution from the corroded layer decreased with increasing penetration depth. In fact, an earlier

study [36] on the effect of corrosion on the mechanical properties of alkaline earth silicate glasses concluded that, at indentation depths that were an order of magnitude greater than the leached layer thickness, there was no detectable effect of corrosion.

The effects of the two short-term corrosion conditions on the mechanical behavior of the tin side of the float glass were also evaluated. Figures **3.10** and **3.11** also suggested that the moduli and hardness of the tin sides of the float glass were not significantly affected by the controlled, short-term corrosion conditions employed in this study. All the observed variations on the tin side were below 2% which was very low relative to the changes observed on the air side. The reportedly higher corrosion resistance of the tin side of float glass relative to the air side was probably the reason for the relatively insignificant changes observed in reduced modulus and hardness on the tin side.

3.4 Summary

Nanoindentation experiments were performed on a fresh commercial 2 mm thick float glass subjected to controlled surface cleaning treatments and short-term exposure conditions in a depth range that was on the order of the corrosion modified surface layer in the float glass. It was observed that the reduced elastic modulus and hardness of the float glass surfaces measured via nanoindentation were dependent on both the surface cleaning treatments and the short-term exposure conditions. It was also observed that the effect of any particular exposure condition was different on the air compared to the tin sides of the float glass. The fact that the surface cleaning treatments used in this study affected the reduced elastic modulus of the two sides of the float glass (especially the

more corrosion resistant tin side) implied that the use of silicate glasses as nanoindentation calibration standards had to be reconsidered. The exposure-dependence of the surface mechanical properties after common cleaning procedures could introduce errors into the technique at the calibration stage of testing that propagate into the final results. Further, it was observed that a given exposure condition did not affect the mechanical response of the air and tin sides of the float glasses in a similar manner. The reduced elastic modulus and hardness of the tin side displayed lesser variation as opposed to the air side.

Chapter 4

Effects of Exposure History and Tin Diffusion on the Nanomechanical Properties of Aged Commercial Float Glass

It was discussed earlier in section **1.1.2** that the two surfaces of flat glass manufactured by the float process [1] were known to be chemically and microstructurally different from each other [2]. The side that was in contact with the molten tin bath ('*tin side*') during float glass processing had diffused tin incorporated into it while the opposite side ('*air side*') experienced surface de-alkalization due to the reducing environment employed in the float chamber. Quite a few studies in the past had probed the role of the diffused tin in altering the local glass network [11, 15, 16, 20], and these studies indicated that the diffused tin increased the connectivity of the local glass network. This increase in network connectivity was expected to raise the elastic modulus and hardness of the tin side as shown with a tin doped silicate glass model system [15, 20]. However, previous work on float glass surface mechanical properties had resulted in all the three possible conclusions – the air side being harder than the tin side [22, 26], the tin side being harder than the air side [27] or the lack of difference between the two sides of float glass [25]. One of these studies [27] suggested that tin diffusion (or the lack of it) into commercial float glass surfaces and related structural differences did not solely influence their mechanical response. This study also alluded to the possibility of other more dominant mechanisms affecting the mechanical behavior of the commercial float

glass surfaces. In the previous chapter it was shown that the relative hardness of the tin side with respect to the air side was dependent on the float glass exposure history. The natural extension of this finding is that influence of exposure history might be the cause of the contradictory results reported by previous nanoindentation studies on float glass surfaces [22, 25-27]. In this chapter the focus was on the evaluation of the role of tin diffusion and long-term exposure history in controlling the mechanical properties of commercial float glasses. To achieve this objective commercial float glasses with well-characterized tin profiles and a unique long-term exposure history were chosen. Initially the sample specifications and sample preparation are presented which is then followed by the results of the nanoindentation tests performed on them. These results are discussed in the light of the previous observations from the nanoindentation testing of float glass surfaces subjected to controlled exposure conditions that were presented in the Chapter 3.

4.1 Sample Specifications

Commercial float glasses that were 2, 6 and 8 mm thick and manufactured by Societá Italiana Vetro (SIV), Italy were used to evaluate the role of tin diffusion on float glass mechanical properties. These glasses were obtained off the float line 16 years ago and their tin diffusion profiles had been characterized using secondary ion mass spectroscopy (SIMS) [3], the results of which are shown in Figure **4.1** .

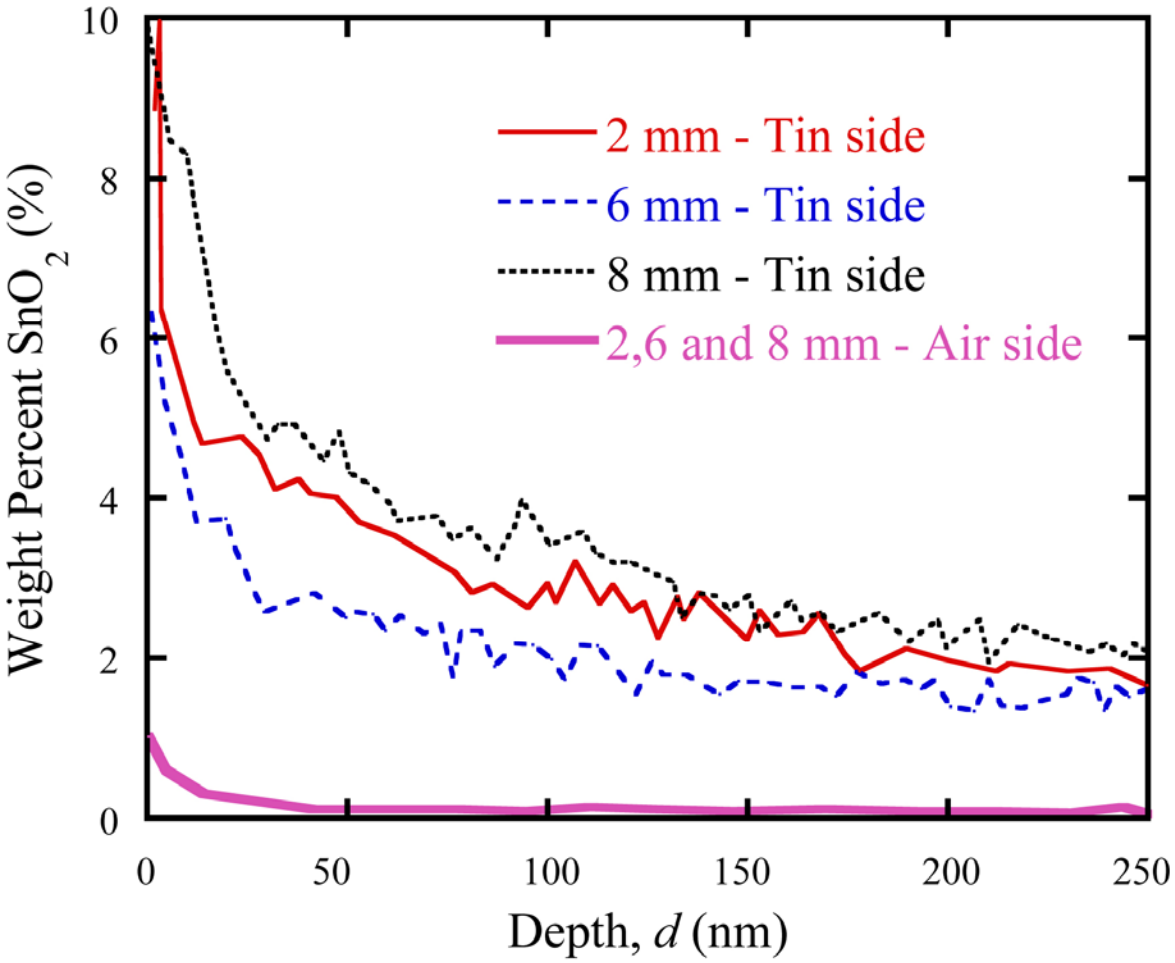

Figure **4.1**: Tin concentration depth profiles for the air and tin sides of the aged 2, 6 and 8 mm thick SIV float glasses obtained by Secondary Ion Mass Spectroscopy (SIMS) [3]. It is observed that the tin sides contain as much as 10% (weight %) SnO_2 near the surface and this concentration decays rapidly to about 2% (weight %) at a depth of ~200 nm. Very low tin concentration (< 1%) is observed even on the air side of float glass.

It was observed from Figure **4.1** that on the tin sides of the three glasses, SnO_2 concentration was the highest near the surface (~7 – 10%) and it steeply decreased with penetration depth before reaching a near constant value of ~2% at a depth of about 200 nm. Relatively insignificant concentrations of SnO_2 were observed on the air side of the three float glasses. As mentioned earlier, it was the objective of this study to evaluate the role of exposure history in conjunction with the role of tin diffusion on the surface

mechanical behavior of float glasses. The SIV float glasses used in this study also possessed a unique long-term exposure history – they had been wrapped in paper and stored in laboratory air for the past 16 years after being procured off the float line. Though these glasses were not qualitatively or quantitatively evaluated for the presence of corrosion modified surface layers, their exposure history was consistent with a natural weathering process.

Specimens used during nanoindentation testing were typically about 3 cm in length and width and required some preparation prior to testing. All the samples had to be mounted on magnetic stainless steel substrates in order to perform nanoindentation. Consequently, only one surface (either the air or the tin side) of the float glass could be evaluated on a given sample. Separate samples were therefore cut from adjacent locations on larger float glass pieces (10 × 10 cm). The 2 mm thick float glass samples were cut by initiating scribe marks with the aid of a diamond scribe along the air side and fracturing the samples along those scribe marks. The 6 and 8 mm float glasses were, however, too thick to be fractured using a scribe mark, so they were cut with a diamond blade along lines scribed on the surface. Cold water was used as the coolant for the diamond blade and the samples were exposed to this coolant for about 30 seconds during the cutting process. Once cut, all the samples were cleaned by rinsing them in a pH 4 Hydrochloric (HCl) acid solution for 2 minutes followed by a rinse in isopropanol and acetone for 3 minutes each. Surfaces were gently cleaned with a cotton swab immediately after removal from acetone and left to dry in laboratory air for 2 minutes. Samples were then mounted onto the stainless steel substrates using a cyanoacrylate adhesive.

4.2 Role of Tin Diffusion on Float Glass Surface Nanomechanical Behavior

This section will present the results of the nanoindentation testing of the air and tin sides of the three different aged float glasses. The nanoindentation testing and data analysis methodology specified in Chapter 2 was used to evaluate the pile-up, reduced elastic moduli, and hardnesses of these surfaces. Since it was noted from Figure **4.1** that the steepest gradient in surface tin concentration was between 0 and 200 nm, indentation penetration depth ranges between 50 and 225 nm were used in this study. The reduced elastic modulus and hardness results shown henceforth were corrected for the pile-up around the indents. These results were correlated with the surface tin concentration profiles shown in Figure **4.1** to evaluate the influence of tin diffusion on the mechanical response of the float glass surfaces.

Experimentally evaluated pile-up results for the 2, 6 and 8 mm thick float glasses are expressed as a percentage of the maximum penetration depth in Figure **4.2**. Depth dependency of pile-up was observed for all the surfaces. As mentioned in Chapter 2, the criterion set in Equation **2-12** to distinguish pile-up from surface roughness was not met for the two shallowest indents in each surface. Therefore the mean values of pile-up at the two shallowest indents on each surface shown in Figure **4.2** represented a conservative estimate of the upper bound of possible pile-up present around the indents, as evaluated from the pre-indent images. Mean values of pile-up were observed to increase upto 6% as the penetration depth increased from ~50 nm to ~225 nm.

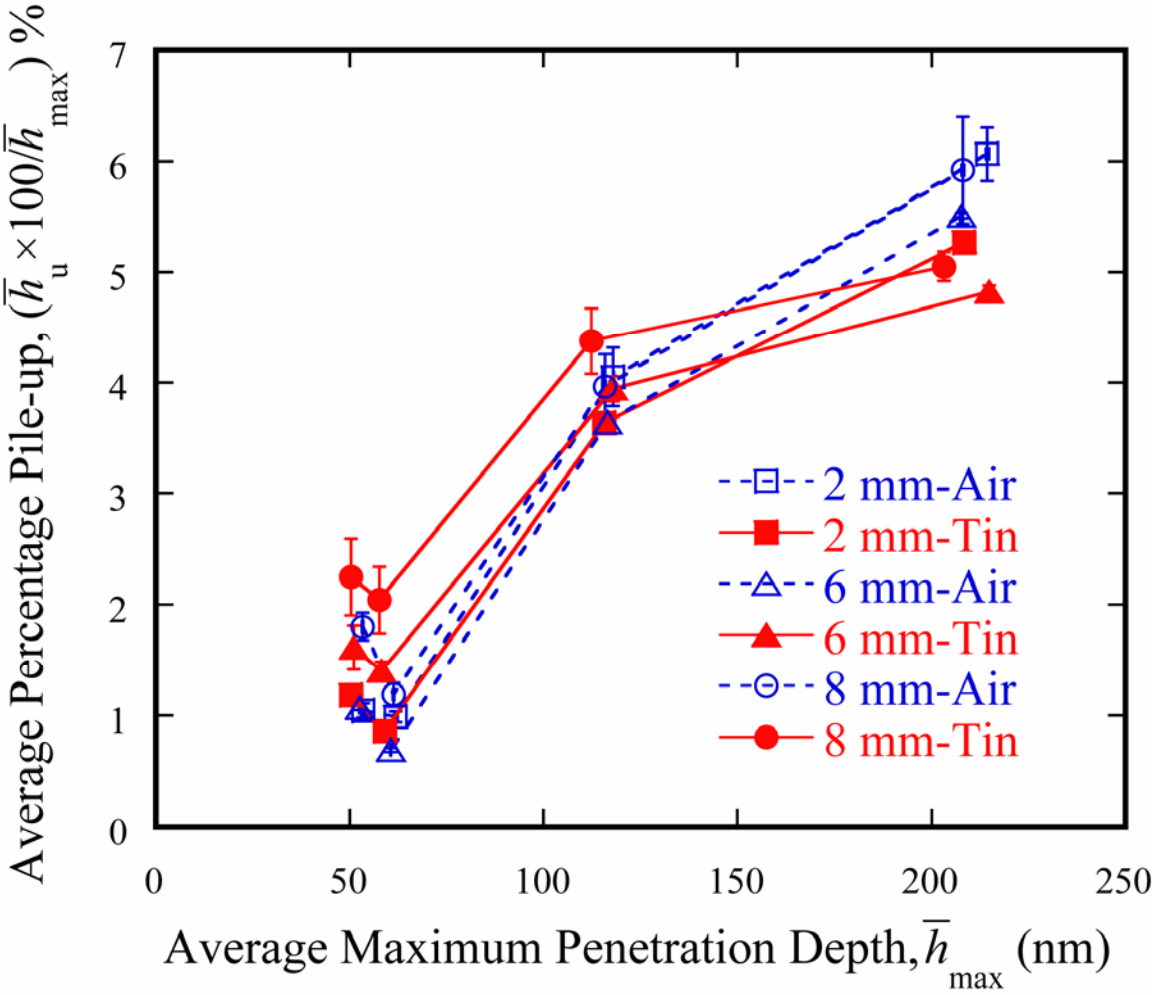

Figure **4.2**: Experimentally evaluated average percentage pile-up as a function of the average maximum penetration depth for 2, 6 and 8 mm thick aged SIV float glasses. Data plotted are the averages of 10 force controlled indents per condition, for four peak force conditions of 750, 900, 2000 and 4000 μN. The length of the error bars on either side of the mean values was equal to the standard error of the mean. Depth dependent pile-up variations are observed with the mean values of percentage pile-up lying between ~1 – 6%. At the very shallow depths pile-up was assumed to be zero since it was indistinguishable from the surface roughness of the samples. The length of the error bar on either side of a mean value is equal to the standard error of the mean.

Figures **4.3** and **4.4** present the pile-up corrected reduced elastic modulus and hardness results respectively, for all the aged float glass surfaces, as a function of the maximum penetration depth.

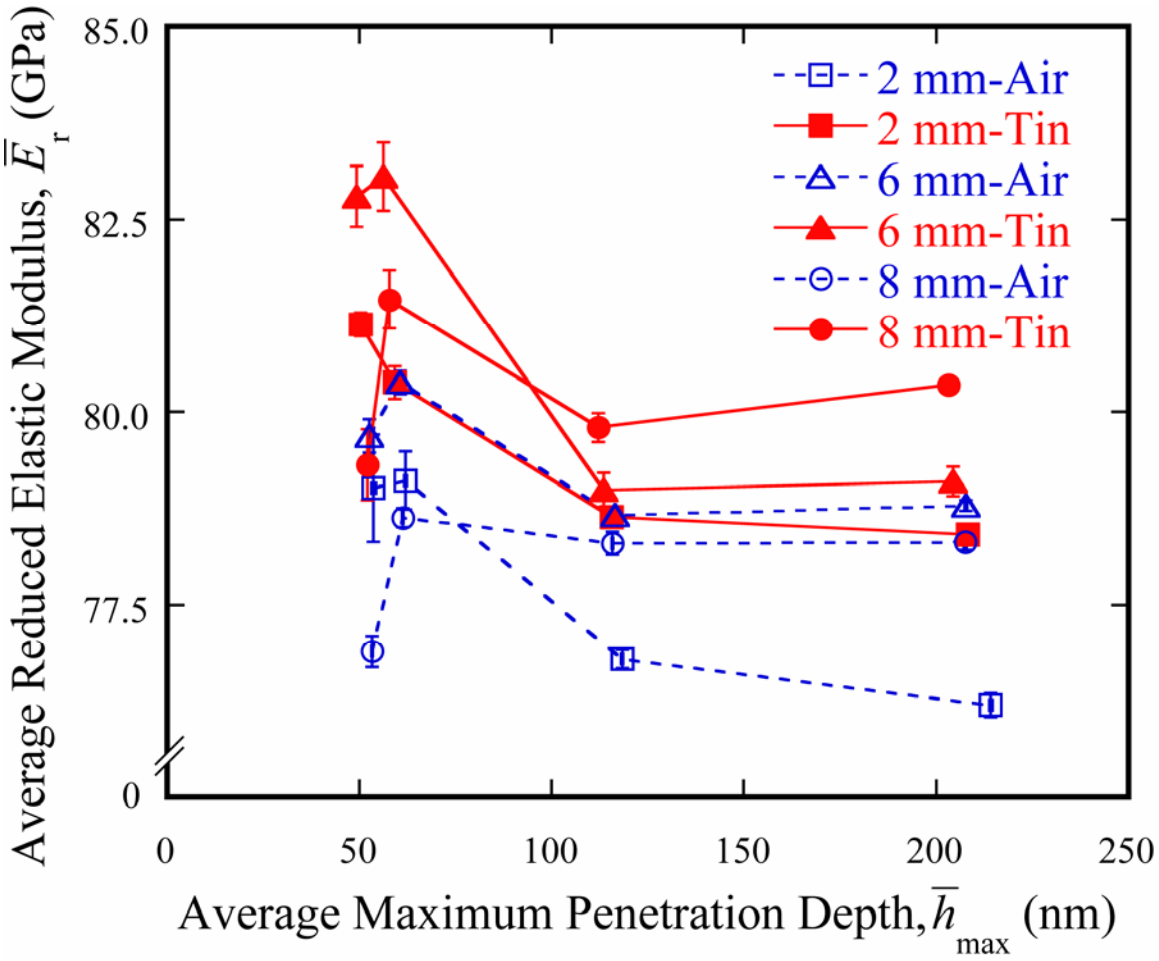

Figure **4.3**: Reduced elastic modulus (E_r) is plotted as a function of the maximum penetration depth (h_{max}) for the air and tin sides of the 2, 6 and 8 mm thick, aged float glasses. Data plotted are the averages of 10 force controlled indents per condition, for four peak force conditions of 750, 900, 2000 and 4000 μN. The length of the error bars on either side of the mean values was equal to the standard error of the mean. It was observed that the tin side of any float glass had a greater E_r compared to its air side. Beyond 100 nm E_r was observed to be independent of penetration depth.

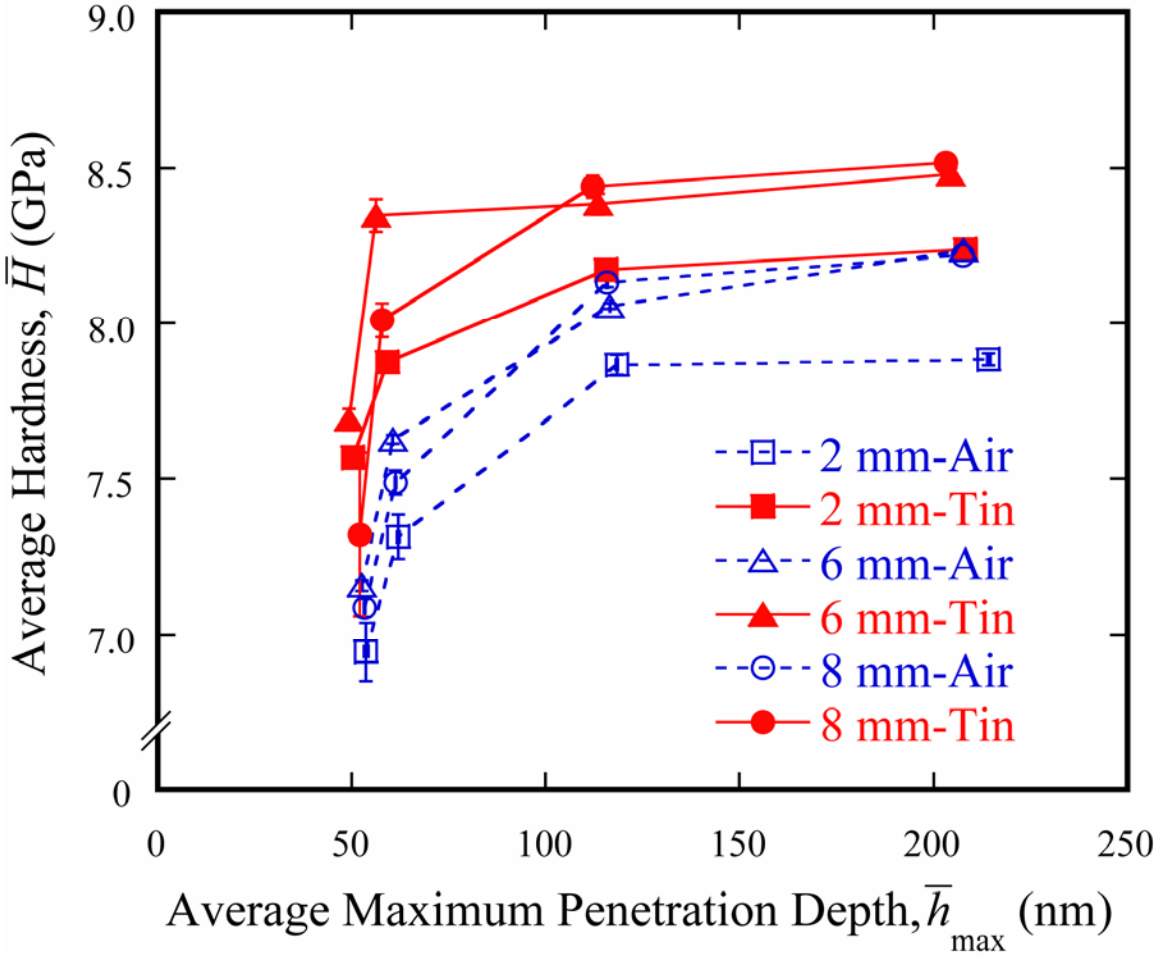

Figure **4.4**: Hardness (H) is plotted as a function of the maximum penetration depth (h_{max}) for the air and tin sides of the 2, 6 and 8 mm thick, aged float glasses. Data plotted are the averages of 10 force controlled indents per condition, for four peak force conditions of 750, 900, 2000 and 4000 μN. The length of the error bars on either side of the mean values was equal to the standard error of the mean. It was observed that the tin side of any float glass had a greater H compared to its air side.

It was observed that the reduced elastic moduli of the different surfaces lay between 75 and 85 GPa for a maximum penetration depth range of ~50 – 225 nm. Within this same penetration depth range, the hardness of these surfaces lay between, 7.0 and 8.5 GPa. Furthermore, it was observed that the hardness increased with increasing penetration depths while the reduced elastic modulus decreased with increasing

penetration depth. At depths greater than 100 nm, both hardness and reduced modulus of the surfaces were found to reach a constant value independent of the penetration depth. More importantly, it was observed that the mechanical properties of the air and tin sides of each float glass were different, with the tin side typically showing a higher reduced elastic modulus and hardness relative to the corresponding air side.

The tin concentration depth profiles for the 2, 6 and 8 mm thick aged float glasses as determined by SIMS were presented in Figure **4.1**. It was observed that the tin concentration profiles of all the three surfaces had relatively small differences between them on the tin side. These tin sides displayed a steep reduction in SnO_2 concentration from 7 – 10 weight % to ~2% within the first 200 nm from the free surface. A relatively smaller amount of tin (<1%) was detected on the air side that decayed to inexistence within the first 50 nm from the surface. For such differences in concentration of SnO_2, it was expected to observe a 2 – 4 GPa difference in reduced elastic modulus between the two sides of the float glass [20]. The reduced elastic modulus results shown in Figure **4.3** indicated that the tin sides of the 2 and 8 mm thick aged float glasses exhibited 2 – 3 GPa higher reduced elastic modulus compared to their air sides in a penetration depth range of 50 – 225 nm. These differences in reduced elastic modulus between the two sides of the 2 and 8 mm thick float glasses were close to the expected differences based on the studies on tin doped silicate glasses. However, the tin side of the 6 mm thick float glass exhibited ~3 GPa higher reduced elastic modulus compared to the air side only at penetration depths under 100 nm. Beyond 100 nm there was no significant difference between the two sides of the float 6 mm thick glass. Since the three float glasses had nominally similar differences in tin concentrations between the air and tin sides at depths beyond

100 nm, similar differences in reduced elastic modulus between the two sides of all the three float glasses were expected at these indentation depths. The fact that the 6 mm float glass did not show any difference in reduced modulus at penetration depths greater (100 nm) while the 2 and 8 mm thick glasses displayed differences as large as 2 – 3 GPa indicated that tin diffusion into the float glass surfaces was not solely responsible for the observed variations in mechanical behavior between the two surfaces of the float glass.

The hardness data shown in Figure **4.4** indicated that the tin sides of the three aged float glasses were 4 – 9% (0.5 – 0.75 GPa) harder than their corresponding air sides. However, the hardnesses of both the air and tin sides decreased at shallow indentation depths. The effect of tin diffusion and related increase in connectivity of the local glass structure on the hardness would have been to increase the hardness. Thus, if the tin-induced increase in the connectivity of the glass network was the most important factor that influenced the mechanical properties of the float glass surfaces, then the hardness of the tin side would have been higher closer to the free surface (since this was the region with the highest tin concentration). However, the hardness decreased at the shallow penetration depths, which indicated that tin diffusion was not the sole parameter that dictated the mechanical behavior of the float glass surfaces. As mentioned earlier in Chapter 3, based on the nanomechanical behavior of the fresh 2 mm thick float glass surfaces that were subjected to controlled exposure conditions, it was clear that exposure history influenced the reduced elastic modulus and hardness of the float glass measured via nanoindentation. In the next section we shall discuss the role of exposure history on the relative hardness or softness of the air side compared to the tin side in the light of

these findings. Further, the possibility of the mechanical behavior of the aged SIV float glasses being influenced by long-term exposure history will be presented.

4.3 Role of Exposure History on Float Glass Surface Nanomechanical Behavior

In this section the influence of exposure history on the relative hardness of the air and tin sides of a float glass will be discussed. Figure **3.10** revealed that there was no difference between the reduced elastic moduli of the air and tin sides of fresh float glass. This result indicated that the structural changes induced by tin diffusion (i.e., increase in connectivity of local glass network) was not the only factor that should be considered. Moreover, the observation from Figure **3.11** that the air side was slightly harder (1 – 3%) than the corresponding tin side confirmed that tin diffusion into float glass was not a dominant parameter that controlled the mechanical response of float glasses. However, Figures **3.10** and **3.11** indicated that after corrosion (weathering and leaching) the differences in mechanical properties between the air and tin sides increased. The tin side of the float glass that was subjected to controlled static weathering at 85% relative humidity and 85°C for 4 days in a humidity chamber had a 5 – 9% higher reduced elastic modulus and 12 – 35% higher hardness compared to a similarly weathered air side. Controlled leaching of these fresh float glass surfaces in de-ionized (DI) water at 90°C for 3 days also produced a tin side that had as much as 10% higher hardness compared to the corresponding air side. The reduced elastic moduli of the tin side subjected to leaching were also slightly higher than the air side at penetration depths less than 100 nm.

However, at greater penetration depths, both of the leached surfaces exhibited similar reduced moduli that were also similar to the moduli of the fresh float glass surfaces. It was thus evident from these observations that the reduced elastic modulus and the hardness of the float glass surfaces were controlled by exposure history of the float glass. Further examination of Figures **3.10** and **3.11** revealed that the mechanical properties of the air side were more susceptible to change (more specifically, a reduction in the hardness and the reduced elastic modulus) for a given exposure condition as compared to the tin side. This difference was attributed to the reportedly greater corrosion resistance of the tin side relative to the air side [30-34]. The air side corrodes more easily, leading to the formation of modified, hydrated, silica-gel type surface layer that was expected to have lower elastic modulus and hardness relative to the pristine glass surface. Thus the air side of fresh float glass might exhibit greater reduced elastic modulus and hardness relative to the tin side in the as-manufactured state while the air side was found to have a higher reduced elastic modulus and hardness after exposure to moist environments. Depending on the exposure conditions, the air side might exhibit reduced elastic moduli and hardnesses that are higher, equal to, or lower than those of the tin side. Moreover, it was observed in the previous chapter that not only the controlled short-term corrosive exposure conditions (exposure time period of a few days), but also controlled surface cleaning treatments (involving a few minutes of exposure) could influence the mechanical properties of float glass surfaces (Figure **3.7** and Figure **3.8**). These surface treatments were similar to the cleaning processes that surfaces prepared for nanoindentation testing might undergo. They varied from each other in the pH of aqueous solution to which the float glass surfaces were initially exposed for a period of 30

seconds each – pH 0.9 hydrochloric acid (acidic), pH 7.1 reverse osmosis water (neutral) and pH 9.5 Alconox® solutions (alkaline) were used. After that, all the surfaces were cleaned with pH 7.1 reverse osmosis water in an ultrasonicator for 5 minutes. Finally all the surfaces were subjected to a 10 seconds rinse in isopropyl alcohol, to eliminate any organic contaminants that might be present on the surfaces. Figure **3.7** indicated that the air and tin sides of float glasses that were subjected to the neutral cleaning procedure exhibited similar reduced elastic moduli in the penetration depth range of 50 – 225 nm. The tin side subjected to the alkaline cleaning treatment displayed a higher reduced elastic modulus compared to the air side at penetration depths below 100 nm while at deeper depths there was no difference between the modulus of the two sides. However, the tin side that underwent the acidic cleaning treatment displayed a consistent, ~8% higher reduced modulus than the corresponding air side (over the depth range of 60 – 225 nm). The hardness comparisons for these different cleaning treatments shown in Figure **3.8** indicated that while the air side subjected to neutral cleaning treatment was slightly (1 – 3%) harder than the corresponding tin side, the air sides subjected to acidic and alkaline cleaning treatments had a lower (5 – 15%) hardness compared to their corresponding tin sides. Consequently, exposure of float glasses to water-containing solutions used for cleaning their surfaces for a time period of just a few minutes influenced the mechanical response of their surfaces. These electrochemical processes are linked to the presence of tin in the glass surfaces, but the resulting mechanical properties are a byproduct of more than just the effect of tin on the deformation resistance of the glass network. It was thus clear from these above results that both controlled short-term corrosive exposure conditions and surface cleaning treatments affected the surface

mechanical response of the float glass. In the light of these conclusions from our earlier study we revisit the reduced elastic modulus and hardness results of the aged 2, 6 and 8 mm thick SIV float glasses (Figures **4.3** and **4.4** respectively) that had a long-term exposure history of about 16 years.

It was concluded in the earlier discussion (section **4.2**) of the mechanical properties of these aged float glasses that tin diffusion into these glasses was not the sole controlling factor of their mechanical properties. The results of the controlled exposure studies on the fresh float glass that were presented in the previous chapter also indicated that the tin sides of these glasses exhibited higher average reduced elastic moduli and hardnesses than the corresponding air sides after exposure to corrosive conditions. Based on these observations, the higher hardness and reduced elastic moduli of the tin sides of the 2, 6 and 8 mm thick aged float glasses compared to their air sides were also, in all likelihood, a consequence of the long-term exposure history of these glasses. Since these aged glasses had been exposed to laboratory storage conditions for 16 years, the air sides of these float glasses probably weathered to a greater extent than the more corrosion-resistant tin sides. Consequently, the air sides of the aged float glass had lower reduced moduli and hardnesses than the corresponding tin sides. Admittedly, the lack of mechanical property data from the original, unexposed, as-received 2, 6 and 8 mm thick aged float glasses impairs our ability to definitively establish the influence of exposure history on their mechanical behavior. However, when the reduced elastic modulus and hardness data of the 2 mm thick fresh (Guardian) and aged (SIV) float glasses were compared, it was observed that the numerical range of mechanical properties of the aged float glass matched with those of fresh float glass that underwent controlled corrosion.

This observation suggests that exposure history might indeed be the dominant effect influencing the surface mechanical properties of the aged float glasses. The reduced elastic moduli of the air side of the 2 mm thick aged float glass (Figure **4.3**) and the corroded 2 mm thick fresh float glasses (i.e., pH 0.9, pH 9.5, weathered and leached conditions shown in Figures **3.7** and **3.10**) were in the range of 75 – 80 GPa. The air side of the 'fresh' 2 mm thick Guardian float glass shown in Figure **3.10** had reduced moduli between 80 and 82.5 GPa. The hardnesses of these corroded Guardian float glass surfaces (Figures **3.8** and **3.1**) lay between 7 and 8 GPa, while that of the 'fresh' Guardian float glass surface were between 7.7 and 8.5 GPa. The tin sides of all the Guardian float glasses surfaces had reduced elastic moduli in the range of 82 – 78 GPa and hardnesses in the range of 7.5 – 8.25 GPa, indicating that the tin sides were nearly unaffected due to exposure. Based on these similarities in the reduced elastic moduli and hardnesses of the fresh 2 mm thick soda-lime-silica float glass that was subjected to controlled exposure conditions and the aged float glasses that were subjected to long-term exposure, it appears that the variations in mechanical properties of the SIV glasses were dominated by exposure history.

4.4 Summary

Surface mechanical properties of aged commercial float glasses of 2, 6 and 8 mm with well-characterized tin profiles were evaluated using nanoindentation to identify the role of tin diffusion in float glasses. The resulting reduced elastic modulus and hardness results, upon correlation with the corresponding tin concentration profiles of these

glasses, indicated that tin diffusion into float glass was not the dominant parameter influencing the surface mechanical properties. The reduced elastic moduli and hardnesses obtained via nanoindentation studies of 2 mm thick Guardian float glasses that were subjected to controlled short-term corrosive exposure conditions and surface cleaning treatments that were presented in the previous chapter established that the exposure history of these surfaces controlled the mechanical response of float glass. Depending on the specific exposure condition, the tin side exhibited reduced elastic moduli and hardnesses that were higher, lower, or equal to the moduli and hardnesses of the corresponding air sides. Further, comparisons between the reduced elastic modulus and hardness results from the 2 mm thick aged float glass and the 2 mm thick fresh float glass that was subjected to controlled exposure conditions, indicated that the observed variations between the air and tin sides of the aged float glasses surfaces were probably controlled by the long-term exposure history driven surface structural modifications. In general, the exposure history dominates the surface mechanical response of the float glasses. Tin diffusion into the tin side of float glass increased the corrosion resistance of this surface relative to the tin deficient air side, due to which the tin side of exposed float glass had higher reduced elastic modulus and hardness compared to the tin side after exposure to corrosive environments. These observations also indicated that the contradictory results in previously published literature [22, 25-27], regarding the hardness of the tin side relative to the air side of float glass previous published literature were probably a result of the effects of not understanding the role of the exposure history on the mechanical response of the float glasses.

Chapter 5

Conclusions and Future Work

In the current chapter the salient outcomes of this study will be presented. This will be followed with suggestions for related studies in the future that would complement the current work.

5.1 Conclusions

This project evaluated the role exposure history and tin diffusion on the surface mechanical properties of commercial float glasses using nanoindentation. Nanoindentation testing and data analysis methodologies were developed so as to reduce the errors associated with the technique of nanoindentation. MATLAB® based algorithms were developed to evaluate the machine compliance, reduced elastic modulus and hardness of the surfaces tested using a modified Oliver-Pharr analysis approach. An experimental approach based on in-situ AFM imaging was developed to estimate and correct for pile-up around the indents. Both the indenter tip area calibration data and the test data were corrected for pile-up around the indents.

The 2 mm thick fresh commercial float glass was used to evaluate the influence of three different surface cleaning treatments and short-term corrosive exposure conditions on the mechanical properties of its surfaces. Three surface cleaning treatment conditions of varying pH's – an acidic hydrochloric acid solution (pH 0.9), nearly neutral reverse osmosis water (pH 7.1), and an alkaline Alconox® solution – were used. Each of

these treatments was followed by a 5 minute exposure to the pH 7.1 reverse osmosis water in an ultrasonic bath and a 10 second rinse in isopropyl alcohol. Controlled short-term corrosive exposure conditions included weathering of the float glass surfaces at 85% relative humidity and 85°C for 4 days while leaching involved the exposure of the float glass surfaces to de-ionized water at 90°C for 3 days. The following list summarizes the conclusions from the work.

1. The neutral cleaning procedure (also referred to as fresh surfaces that did not undergo weathering or leaching) resulted in an average reduced modulus of 80 – 82 GPa. The air side that was subjected to the neutral cleaning treatment displayed the highest average reduced moduli and average hardnesses while the acidic surface cleaning exposure lowered the average reduced elastic moduli of the air side by ~6% (~5.0 GPa). Similarly, the alkaline treatment caused a decrease of ~3% in the average reduced elastic moduli. On the tin side, a difference of ~5 GPa was observed between the surfaces subjected to acidic and alkaline cleaning treatments. The tin side exposed to the acidic cleaning treatment displayed the highest average reduced elastic modulus while the tin side exposed to the alkaline cleaning treatment exhibited the least average modulus. While the air and tin sides of short-term leached glass did not exhibit a large deviation from the fresh glass behavior, the air side of the that underwent short-term weathering displayed 4 – 9% (3 – 6 GPa) reduction in the average reduced modulus relative to the air side of the fresh glass. Similarly, the tin side of the weathered glass exhibited reduced elastic moduli that were nearly equivalent to the corresponding fresh float glass surface. It was apparent that the mean reduced modulus of the air

side of float glass was more susceptible to exposure condition-induced changes. In general, alkali silicate glasses were susceptible even to very short duration, surface cleaning treatments and their use as nanoindentation calibration materials should be carefully considered.

2. The average hardnesses of the surfaces were also observed to be affected by the surface cleaning treatments and the short-term exposure conditions. The average hardnesses of the float glass surfaces subjected to the neutral treatment were between 7.5 – 8.25 GPa. On the air side, the alkaline cleaning treatment resulted the least average hardnesses (5 – 13%, or 0.5 – 1 GPa, lower) relative to the neutral cleaning treatment (~7.75 – 8.25 GPa). The acid cleaning treatment also resulted in the reduction of the average hardness, but to a lesser extent (~3 – 6%). The air side of the weathered glass exhibited the maximum decrease in the average hardness (25% lower than the mean hardness of fresh glass) while leaching of the air side caused up to 10% decrease in the mean hardness at penetration depths less than 100 nm. The average hardness of the tin side was found to be nearly constant for all the exposure conditions (i.e., variations less than 2%). These results indicated that the air side of float glass was more susceptible to variations in average hardness as compared to the tin side of the float glass.
3. The surface cleaning treatments and the short-term corrosive exposure history of the float glass surfaces affected their average reduced elastic moduli and average hardnesses that were measured using nanoindentation. The mechanical properties

of the two sides of float glasses were affected to different extents due to the differences in chemistry between the two sides.

4. The 2, 6 and 8 mm thick aged float glasses that had undergone long-term exposure (over a period 16 years) to laboratory air were evaluated using nanoindentation at depths ranging from 50 – 225 nm to identify the role of tin diffusion on modifying the surface mechanical response of float glasses. Attempts to correlate the tin profiles with the trends in the average reduced elastic moduli and average hardnesses indicated that tin diffusion into these glasses was not the sole parameter affecting the mechanical properties of these surfaces.
5. The average reduced elastic moduli and average hardness results from nanoindentation studies of 2 mm thick fresh float glasses subjected to controlled surface cleaning treatments and short-term corrosive exposure conditions showed that the tin side could have average reduced elastic modulus and hardness that were either higher, lower or equal to the modulus and hardness of the corresponding air sides depending on the nature of the exposure history.
6. Further, comparisons between the mean values of the reduced elastic modulus and hardness from the 2 mm thick aged float glass and the 2 mm thick fresh float glasses that subjected to controlled exposure conditions indicated that the variations in the aged float glass surfaces, which possessed a very long exposure history, were probably controlled by exposure history driven surface structural modifications. Tin diffusion into the tin side of float glass increased the corrosion resistance of the surface relative to the air side, thereby elevating the mean values of reduced elastic moduli and hardnesses of the surfaces. The contradictory

results in previously published literature are probably a byproduct of the effects of exposure history on the mechanical response of float glass.

5.2 Recommended Future Work

This study has shown that the nanomechanical properties of the surfaces of float glasses are dependent on their exposure history. As mentioned in the previous section, the fact that surface cleaning treatments could lead to changes in the reduced elastic moduli and hardnesses. Since similar effects are expected in reference glasses for nanoindentation testing, calibration standard silicate glasses such as fused silica should be evaluated for the exposure history dependence of their properties. It was also observed in the current study that the air side of fresh float displayed greater average hardness relative to the corresponding tin side. This is probably due to the surface de-alkalization occurring on this surface due to exposure to the reducing environment within the float chamber. It thus appears that the alkali and alkaline earth constituents of the glass have a significant impact on its surface mechanical properties. Therefore, testing binary silicate glasses with varying compositions of the alkali or alkaline earth constituents would provide an insight into the effect of these constituents on the surface mechanical behavior of silicate glasses.

Bibliography

1. Pilkington, L.A.B., *Review Lecture. The Float Glass Process*. 1969, The Royal Society. p. 1-25.
2. Sieger, J.S., *Chemical characteristics of float glass surfaces.* Journal of Non-Crystalline Solids, 1975. **19**: p. 213-220.
3. Verita, M., et al., *EPMA, RBS and SIMS analyses of tin profiles in commercial float glasses*, in *International Congress on Glass*, A. Duran and J.M.F. Navarro, Editors. 1992, S. E. de Ceramica y Vidrio Madrid p. 415-420.
4. Franz, H., *Surface chemistry of commercial glasses.* Ceramic Engineering and Science Proceedings, 1995. **16**(2): p. 221-227.
5. Williams, K.F.E., et al., *Tin oxidation state, depth profiles of Sn2+ and Sn4+ and oxygen diffusivity in float glass by Mossbauer spectroscopy.* Journal of Non-Crystalline Solids, 1997. **211**(1-2): p. 164-172.
6. Williams, K.K.F.E., et al., *Characterization of tin at the surface of float glass.* Journal of non-crystalline solids, 1998. **242**(2-3): p. 183-188.
7. Townsend, P.P.D., et al., *Comparisons of tin depth profile analyses in float glass.* Journal of non-crystalline solids, 1998. **223**(1-2): p. 73-85.
8. Frischat, G.H., C. Müller-Fildebrandt, and H.D.M. G, *On the origin of the tin hump in several float glasses.* Journal of Non-Crystalline Solids, 2001. **283**(1-3): p. 246-249.
9. Hayashi, Y., K. Matsumoto, and M. Kudo, *The diffusion mechanism of tin into glass governed by redox reactions during the float process.* Journal of Non-Crystalline Solids, 2001. **282**(2-3): p. 188-196.
10. Ishikawa, T. and S. Akagi, *The structures of glasses in the system SnO-SiO_2.* Physics and Chemistry of Glasses, 1978. **19**(5): p. 108-114.
11. Karim, M.M. and D. Holland, *Physical properties of glasses in the system SnO-SiO_2.* Physics and Chemistry of Glasses, 1995. **36**(5): p. 206.
12. Williams, K.F.E., et al., *Mossbauer spectra of tin in binary Si-Sn oxide glasses.* Journal of Physics: Condensed Matter, 1995. **7**(49): p. 9485-97.
13. Bent, J.F., et al., *The structure of tin silicate glasses.* Journal of Non-Crystalline Solids, 1998. **232-234**: p. 300-308.
14. Holland, D., et al., *Site symmetry in binary and ternary tin silicate glasses - 29Si and 119Sn nuclear magnetic resonance.* Journal of Physics Condensed Matter, 2003. **15**(31): p. 2457-2472.
15. LeBourhis, E. *Tin influence on physical properties of silico-soda-lime glass*. in *XVIII International Congress on Glass*. 1998. San Francisco, California, USA: American Ceramic Society, Westervillle, Ohio.
16. Sears, A., D. Holland, and M.G. Dowsett, *Physical properties of stannosilicate glasses.* Physics and Chemistry of Glasses, 2000. **41**(1): p. 42-8.

17. Johnson, J.A., et al., *Ternary alkali stannosilicate glasses: a Mossbauer and neutron diffraction study.* Journal of Physics: Condensed Matter, 2000. **12**(3): p. 213-30.
18. Benne, D., et al., *Square-wave voltammetry and Mössbauer spectroscopy in tin-doped soda-silicate and soda-lime-silicate glasses.* Journal of Non-Crystalline Solids, 2003. **318**(1-2): p. 202-212.
19. Holland, D., *Combined techniques for the study of glass structure*, in *Advances in the Characterization of Ceramics*. 1996, Institute of Materials: University of Manchester, England.
20. Krohn, M.H., et al., *Effect of tin-oxide on the physical properties of soda-lime-silica glass.* Journal of Non-Crystalline Solids, 2005. **351**(6-7): p. 455-465.
21. Tummala, R.R. and B.J. Foster, *Strength and dynamic fatigue of float glass surfaces.* Journal of the American Ceramic Society, 1975. **58**(3-4): p. 156-7.
22. Gulati, S.T., R. Akcakaya, and J.R. Varner, , *Fracture behavior of tin vs. air side of float glass.* Ceramic Transactions, 2001. **122**: p. 317-325.
23. Krohn, M.H., et al., *Biaxial flexure strength and dynamic fatigue of soda-lime-silica float glass.* Journal of the American Ceramic Society, 2002. **85**(7): p. 1777-1782.
24. R. Akcakaya, S.T. Gulati, and J.R. Varner, *Fatigue behaviour of surface flaws on air vs. tin sides of soda-lime-silica float glass*, in *Challenges and Break-Through Technologies*. 2000: Amsterdam.
25. Ramsey, P.M. and A.J. Whitehead, *Nanohardness measurements of float glass surfaces*, in *International Congress on Glass*. 1992: Madrid, Spain.
26. Goodman, O. and B. Derby. *Combined nanoindentation and acoustic determination of the elastic properties of float glass surface*. 2004. Nashville, TN., United States: American Ceramic Society.
27. Howell, J.A., J.R. Hellmann, and C.L. Muhlstein, *Nanomechanical properties of commercial float glass.* Journal of Non-Crystalline Solids, 2008. **354**(17): p. 1891-1899.
28. Clark, D.E., C.G. Pantano Jr., and L.L. Hench, *Corrosion of Glass*. 1979: Books for Industry.
29. Bunker, B.C., *Molecular mechanisms for corrosion of silica and silicate glasses.* Journal of Non-Crystalline Solids, 1994. **179**: p. 300-308.
30. Shelby, J.E. and J. Vitko, Jr., *Surface characterization of weathered low-iron float glass.* Journal of Non-Crystalline Solids, 1980. **38 & 39**(Pt 2): p. 631-636.
31. Pantano, C.G., *Chemical Properties of Real and Ideal Glass Surfaces*, in *Materials Characterization for Systems Performance and Reliability*, McCauley and Volker, Editors. 1986, Plenum: New York. p. pp. 127-148.
32. Mingqin, G., et al., *A study on resistivity against water of tin-doped glasses.* Journal of Non-Crystalline Solids, 1986. **80**(1-3): p. 319-323.
33. Feldmann, M. and R. Weissmann, *Initial stages of float glass corrosion.* Journal of Non-Crystalline Solids, 1997. **218**: p. 205-209.
34. Bange, K., et al., *Multi-method characterization of soda-lime glass corrosion. Part 2. Corrosion in humidity.* Glass Science and Technology: Glastechnische Berichte, 2002. **75**(1): p. 20-33.

35. Bange, K., et al., *Multi-method characterization of soda-lime glass corrosion Part 1. Analysis techniques and corrosion in liquid water.* Glass Science and Technology: Glastechnische Berichte, 2001. **74**(5): p. 127-141.
36. Koenderink, G.H., R.H. Brzesowsky, and A.R. Balkenende, *Effect of the initial stages of leaching on the surface of alkaline earth sodium silicate glasses.* Journal of Non-Crystalline Solids, 2000. **262**(1): p. 80-98.
37. Smith, N.J. and C.G. Pantano, *Leached layer formation on float glass surfaces in the presence of acid interleave coatings.* Journal of the American Ceramic Society, 2008. **91**(3): p. 736-744.
38. Lombardo, T., et al., *Weathering of float glass exposed outdoors in an urban area.* Glass Technology, 2005. **46**(3): p. 271-276.
39. Hayashi, Y., Y. Fukuda, and M. Kudo, *Investigation on changes in surface composition of float glass - Mechanisms and effects on the mechanical properties.* Surface Science, 2002. **507-510**: p. 872-876.
40. Oliver, W.C. and G.M. Pharr, *Improved technique for determining hardness and elastic modulus using load and displacement sensing indentation experiments.* Journal of Materials Research, 1992. **7**(6): p. 1564-1580.
41. Hainsworth, S.V., H.W. Chandler, and T.F. Page, *Analysis of nanoindentation load-displacement loading curves.* Journal of Materials Research, 1996. **11**(8): p. 1987-1995.
42. Den Toonder, J., J. Malzbender, and G. De With, *The P-h2 relationship in indentation.* Journal of Materials Research, 2000. **15**(5): p. 1209-1212.
43. Troyon, M. and M. Martin, *A critical examination of the P-h2 relationship in nanoindentation.* Applied Physics Letters, 2003. **83**(5): p. 863-865.
44. Cheng, Y.-T.s.C.-M., *Analysis of indentation loading curves obtained using conical indenters.* Philosophical Magazine Letters, 1998. **77**(1): p. 39-47.
45. Doerner, M.F. and W.D. Nix, *A method for interpreting the data from depth-sensing indentation instruments.* Journal of Materials Research, 1986. **1**(4): p. 601-9.
46. Sneddon, I.N., *Relation between load and penetration in axisymmetric Boussinesq problem for punch of arbitrary profile.* International Journal of Engineering Science, 1965. **3**: p. 47-57.
47. Pharr, G.M., W.C. Oliver, and F.R. Brotzen, *On the generality of the relationship among contact stiffness, contact area, and elastic modulus during indentation.* Journal of Materials Research, 1992. **7**(3): p. 613-617.
48. King, R.B., *Elastic analysis of some punch problems for a layered medium.* International Journal of Solids and Structures, 1987. **23**(12): p. 1657-1664.
49. Field, J.E., *The Properties of Natural and Synthetic Diamond*. 1992, London: Academic Press.
50. Mencik, J. and M.V. Swain, *Errors associated with depth-sensing microindentation tests.* Journal of Materials Research, 1995. **10**(6): p. 1491-1501.
51. Fischer-Cripps, A.C., *Nanoindentation*. 2nd ed. Mechanical engineering series. 2004, New York: Springer.

52. Howell, J.A., *Surface properties of glass evaluated using nanoindentation*, in *Materials Science and Engineering*. 2005, The Pennsylvania State University: University Park.
53. Bridgman, P.W. and I. Simon, *Effect of very high pressures on glass.* Journal of Applied Physics, 1953. **24**: p. 405-413.
54. Cohen, H.M. and R. Roy, *Effects of ultrahigh pressures on glass.* Journal of the American Ceramic Society, 1962. **44**: p. 523-524.
55. Cohen, H.M. and R. Roy, *Densification of glass at very high pressure.* Physics and Chemistry of Glasses, 1965. **6**: p. 149-161.
56. Lambropoulos, J.C., S. Xu, and T. Fang, *Constitutive law for the densification of fused silica, with applications in polishing and microgrinding.* Journal of the American Ceramic Society, 1996. **79**(6): p. 1441-1452.
57. Xin, K. and J.C. Lambropoulos. *Densification of fused silica: Effects on nanoindentation*. 2000. San Diego, CA, USA: Society of Photo-Optical Instrumentation Engineers, Bellingham, WA, USA.
58. Uhlmann, D.R., *Densification of alkali silicate glasses at high pressure.* Journal of Non-Crystalline Solids, 1973. **13**(1): p. 89-99.
59. Malin, M. and K. Vedam, *Ellipsometric studies of environment-sensitive polish layers of glass.* Journal of Applied Physics, 1977. **48**(3): p. 1155-1157.
60. *Corning 1737 AMLCD Glass Substrates: Material Information.* 2004 Corning.
61. Kirkpatrick, R., *Durability of octadecyltrichlorosilane coated borosilicate glasses*, in *Materials Science and Engineering*. 2005, The Pennsylvania State University.
62. Hay, J.L. and G.M. Pharr, *Instrumented Indentation Testing*, in *ASM Handbook Volume 8: Mechanical Testing and Evaluation*, H. Kuhn and D. Medlin, Editors. 2000, ASM International, Materials Park, OH. p. 232-243.
63. Oliver, W.W.C. and G.G.M. Pharr, *Measurement of hardness and elastic modulus by instrumented indentation: Advances in understanding and refinements to methodology.* Journal of materials research, 2004. **19**(1): p. 3-20.
64. Bolshakov, A. and G.M. Pharr, *Influences of pileup on the measurement of mechanical properties by load and depth sensing indentation techniques.* Journal of Materials Research, 1998. **13**(4): p. 1049-1058.
65. Bobji, M.S., S.K. Biswas, and J.B. Pethica, *Effect of roughness on the measurement of nanohardness - a computer simulation study.* Applied Physics Letters, 1997. **71**(8): p. 1059.
66. Bobji, M.S., et al., *Influence of surface roughness on the scatter in hardness measurements - a numerical study.* International Journal of Rock Mechanics and Mining Sciences, 1999. **36**(3): p. 399-404.
67. Nagy, P., et al. *The combined application of nanoindentation and scanning probe microscopy to materials sciences*. 2003. Balatonfured, Hungary: Trans Tech Publications Ltd.
68. Rabinovich, S.G., *Measurement errors and uncertainties : theory and practice*. 3rd ed. 2005, New York: AIP Press.

69. Michalske, T.A., B.C. Bunker, and K.D. Keefer, *Mechanical properties and adhesion of hydrated glass surface layers.* Journal of Non-Crystalline Solids, 1990. **120**(1-3): p. 126-137.
70. *ASTM Standard C 1285-02, Standard Test Methods for Determining Chemical Durability of Nuclear, Hazardous, and Mixed Waste Glasses and Multiphase Glass Ceramics: The Product Consistency Test (PCT).* 2002.
71. Krohn, M.H., *Effect of tin on the relationship between composition, structure, and properties of soda-lime-silicate glasses*, in *Materials Science and Engineering*. 2004, The Pennsylvania State University: University Park.
72. Doremus, R.H., *Glass Science*. 2nd ed. 1994: John Wiley & Sons Inc.
73. Douglas, R.W. and T.M.M. El-Shamy, *Reactions of Glasses with Aqueous Solutions*. 1967. p. 1-8.
74. El-Shamy, T.M., J. Lewins, and R.W. Douglas, *Dependence on the pH of the decomposition of glasses by aqueous solutions.* Glass Technology, 1972. **13**(3): p. 81-87.